Interactions of high energy mesons with complex nuclei

Margaret G. E. Welton

INTERACTIONS OF HIGH ENERGY MESONS

WITH COMPLEX NUCLEI.

Thesis submitted for the degree of

Doctor of Philosophy

in the University of Durham.

by

Margaret G.E. Welton.

January 1967.

"Interactions of High Energy Mesons with Complec Nuclei".

M.G.E. Welton

Abstract

In order to study further the reaction of 300 MeV π^- mesons with carbon nuclei, it was necessary to acquire with good statistics the energy of the secondaries at different angular intervals. Apparatus was designed and built to support nuclear emulsion plates in a vertical plane around a central target. The apparatus was inserted between the poles of a magnet in a field of 25.5 kilogauss during the exposure. The plates were then area scanned for suitable tracks. A method of analysis was developed especially to cope with the problem of a finite target.

$p\beta$ measurements were also made on secondaries from interactions in a carbon target. The actual incident beam energy was determined and was 285 MeV in both cases. The two sets of results agreed well over the angular interval where comparison could be made. The results

were also compatible with previous experimental results at 300 MeV.

Comparison was also made with the results predicted by a Monte Carlo nuclear cascade calculation (Bertini), but although the energy-angular distributions were almost identical, the momentum distributions at any one specific emission angle did not give good agreement. The observed angular distribution can be explained if the pion is subject to a potential on entering the nucleus, and if the nucleons have a momentum distribution extending up to at least 275 MeV/c. The nuclear well depth is estimated to be on average 53 MeV. An exclusion principle operates preventing pion-nucleon interaction if the nucleon is not thereby raised to the top of the nuclear well.

CONTENTS.

—

Preface

The aim of the experiments described in this thesis
was to find a method of detecting the secondaries from a
π-nucleus interaction, and of accurately and rapidly
measuring the secondary pion energy so that good statistics
could be achieved. A framework to hold and accurately
locate emulsion plates was designed and calibrated by
Dr. A.J. Apostalakis and the author, and made in the
Physics Department workshop. The matrix method of
analysis was worked out by Dr. J.V. Major. The computer
programs were written and run by the author. The
scanning of the spectrographic plates was done by
Mrs. E. Errington and the author. pβ measurements were
made by Drs. J.V. Major, A.J. Apostalakis, N.A. Kahn,
G.A. Briggs and C. Kitchen. The π beam was located and
aligned from the data supplied by the CERN Laboratory,
and the exposure made by Drs. J.V. Major, A.J. Apostalakis,
P.J. Finney and the author.

LIST OF FIGURES.

LIST OF TABLES.

1.   PION INTERACTIONS WITH COMPLEX NUCLEI.

Since the smallest atomic nucleus, that of hydrogen, has approximately nine times the mass of a pi meson, a target pion of sufficiently low energy may see a nucleus as a collection of separate nucleons.   Examination of emulsion stacks exposed to meson beams have shown that in the region of 300 MeV pi-nucleus interactions give rise to at the most only one emerging nucleon of high energy, and several protons of low energy.   The cross-section for pi-nucleon interaction predicts only one collision between the meson and a nucleon within the nucleus (Finney et al. 1962; Yuan, 1956).   This struck nucleon will emerge with a higher energy than the nucleons emitted by the unstable residual nucleus, and hence all the evidence indicates pi-nucleon rather than pi-nucleus interactions as predominating.

In the following report therefore, pi-nucleon interactions will be considered first, followed by an attempt to determine the effect of the nuclear structure on the interaction.

1.1. Summary of Pion-Nucleon Interactions.

The observed interactions of pi-mesons with nucleons at energies below 1 GeV are as follows:-

elastic scattering $\pi^- + p \rightarrow \pi^- + p$)   1.1.1.

$\pi^- + n \rightarrow \pi^- + n$)   1.1.2.

charge exchange $\pi^- + p \rightarrow \pi^0 + n$ 1.1.3.

radiative capture $\pi^- + p \rightarrow \gamma + n$ 1.1.4.

The cross-section for radiative absorption is negligible compared with the first three.   It is expected from charge symmetry that $\sigma(\pi^+ n) = \sigma(\pi^- p)$ and $\sigma(\pi^- n) = \sigma(\pi^+ p)$. At 190 MeV, the cross-sections $\sigma(\pi^+ p)$ and $\sigma(\pi^- p)$ show a definite maximum, the $\frac{3}{2} - \frac{3}{2}$ resonance.   At 300 MeV the values of these cross-sections are (75 ± 5) mb and (32 ± 2) mb respectively.   The latter cross-section including about 22 mb for elastic scattering and 11 mb for exchange scattering (Yuan, 1956).

1.2. Interactions with Complex Nuclei.

Even when a pion interacts only with a single

nucleon within a nucleus through processes 1.1.1 to 1.1.4, the transfer of energy by the meson to the struck nucleon upsets the nuclear equilibrium, and the interaction leaves the nucleus in an excited state.

The impulse approximation assumes that no transfer of energy to the residual nucleus takes place during the time of the collision, and is valid in interactions where the projectile particle on average makes only one collision in the nucleus. If the struck nucleon escapes from the nucleus without making any further collisions, it must have received enough energy to lift it out of the nuclear potential well. The residual nucleus recoils in order that momentum may be conserved, and attains equilibrium by the ejection of particles or photons. When a large momentum transfer to the nucleus occurs, then equilibrium is attained by the ejection of several low energy nucleons, known as 'evaporation particles'. Inelastic interactions with two or more nucleons are possible, especially if the cluster models of the nucleus apply at the interaction energy. An example is the absorption of pi-mesons in the nucleus by the following processes:-

$$\pi^- + p + n \rightarrow n + n$$

and
$$\pi^+ + p + n \rightarrow p + p$$

These processes can occur particularly at zero and low kinetic energies.

A meson incident on a nucleus may thus be scattered elastically by the whole nucleus, or react inelastically, being scattered by one or more nucleons, undergoing charge exchange, or being absorbed. A process cannot be completely identified unless all the secondaries can be observed. There is however, no means of directly observing the neutral particles.

As an association of elementary particles the nucleus itself presents many problems, and not least among these is the distribution within the nucleus of these particles, the energy states which they occupy, and the appearance which this entity presents to an incident particle. Probe particles used to examine the nucleus, which appear to interact only with one nucleon, indicate that the nucleons are distributed in momenta. Various models have been proposed to explain the distribution of nucleonic momenta and energies.

a) <u>The Fermi Model.</u>   One of the first hypotheses concerning the structure of the nucleus was that the nucleus was a gas of protons and neutrons confined to the nuclear volume.   To each nucleon is assigned an energy state and as they are Fermions, no two nucleons can occupy identical states.   Furthermore it is assumed that there are no collisions between nucleons.   Except at high excitation energies, the gas would be completely degenerate (zero temperature, T=0) and the momentum distribution would be:-

$$N(p)dp = \frac{3p^2 . dp.}{P_{max}} \qquad 1.2.1$$

where P_{max} is the Fermi momentum corresponding to the Fermi energy, E_F, and is the maximum possible momentum, determined by the nuclear volume.   The Fermi energy is about 25 MeV, ($P_{max} \sim 220$ MeV/c).   The total depth of the potential well for protons is about 30 MeV.

b) <u>The Shell Model.</u>   This model describes the nucleus by a system of nucleon orbits similar to the electron orbits of the atom.   As the nucleons are Fermions the same exclusion rules apply.   These nucleonic

energy states or levels may have a specified spatial density, but no momentum density is ascribed to them. However, for an unexcited nucleus the lowest states will be filled, and the Pauli exclusion principle will prohibit interactions involving the transfer of nucleons to already occupied states.

The orbital angular momentum of an energy state is denoted by $\ell = 0$, 1, 2, 3, etc, or the orbital letters s, p, d, f, g..... An orbit or shell is referred to as 1s, 4s, 2p, etc, where the number before the letter is the radial number. Allowing for spin-orbit coupling (Mayer, 1949 and Haxel et al. 1949) the energies of the particles in the shells are split into subshells characterised by $j (= \bar{\ell} + \bar{s})$. For example, in carbon the six protons (or the six neutrons) are distributed as follows, two protons in the $1s_{1/2}$ energy states, and the remaining four in the $1p_{3/2}$ energy states; i.e. $1s^2_{1/2} \ 1p^4_{3/2}$. The four $p_{3/2}$ protons are differentiated by their relative orientation of the j vector.

c) <u>Cluster Models</u>. These models describe the nucleus as configurations of stable units such as alpha

particles or deuterons. The nucleons are thus bound to smaller units within the nucleus, and are more localised than in the Fermi model. This localisation of the target nucleon within the nucleus during impact will give rise to apparent higher momentum components through the operation of the Uncertainty Principle. The cluster models have only limited success in explaining nuclear phenomena, especially in nuclei where all the nucleons cannot be incorporated into alpha or deutron units.

d) The Optical Model. Although the following model does not yield information on the momentum distribution within the nucleus, it provides an invaluable overall description of nuclear interactions. A particle incident on a nucleus can be compared with a light wave incident on a finite medium which both diffracts and refracts the light with absorption of the refracted beam. The nucleus is thus a region of complex refractive index, or complex potential. This model tends to disregard the structure of the nucleus, and hence the density fluctuations across the nuclear volume. It has no means of describing changes which take place in the nucleus due to an interaction, but does give an expression for

the scattered particle in elastic scattering. All other processes are classed as absorption. It also yields only the average values for the cross-section, and ignores any structural effects such as resonances.

The complex potential was first introduced to describe the scattering of nucleons by nuclei, (Fernbach et al. (1949); Feshbach et al. (1954)), and later extended to cover the scattering of alpha particles and mesons. If the nucleus is considered as having a complex potential, then the real part $V'(r)$ introduces a phase difference between that part of the wave traversing the nucleus and the rest of the wave. Interference between these two wave fronts produces diffraction, and absorption of the wave in the nucleus due to $W(r)$ can enhance the diffraction effect. If the complex potential is V, then

$$V = V'(r) + iW(r).$$

The Schroedinger equation and its complex conjugate for an incident particle are:-

$$\nabla^2 \psi + 2M/\hbar^2 (E - V' - iW) \psi = 0$$

$$\nabla^2 \psi^* + 2M/\hbar^2 (E - V' + iW) \psi^* = 0$$

multiplying by ψ^* and ψ, and subtracting gives –

$$\psi^* \nabla^2 \psi - \psi \nabla^2 \psi^* = 4M/\hbar^2 . iW \cdot \psi \psi^*$$

i.e. $$\hbar/2iM . \nabla . (\psi^* \nabla^2 \psi - \psi \nabla^2 \psi^*) = 2W \psi^* \psi /\hbar$$

The left-hand side is the divergence of the probability current, and equals the increase of particle density per unit volume. For absorption this must be negative. On the right-hand side therefore W<0, and the absorption is proportional to the imaginary part of the potential and the particle density.

Nuclear forces are short range, and therefore, as the nucleus is stable, the resultant force at the centre is zero and hence the potential is constant, while at the surface a strongly attractive force operates. The real part of the potential is thus similar to the nuclear density, and an equation of the following form has been widely used

$$V'(r) = -V_o/(1 + e^{(r-c)/a})$$

where c and a are closely related to the corresponding
quantities for the nuclear radius.

W(r) is much more difficult to derive.   Because of
the short range of nuclear forces, it should, like V'(r),
be constant in the central nuclear region, and it seems
reasonable that absorption by the nucleus should be
proportional to the nuclear density.   Hence one can use

$$W(r) = -W_o/(1 + e^{(r-c)/a})$$

where c and a are not necessarily the same as before.

There is however an alternative view which considers
the operation of the exclusion principle within the
nucleus.   As the nucleus is a highly degenerate Fermi-
Dirac system, the principle prevents the transfer of
momentum and energy between particles, which would
normally occur due to the strong forces present.   In this
case the mean-free-path of a particle in the system may
be much longer than it would be if the exclusion principle
did not operate.   However in the surface region this
exclusion effect is much reduced, and hence the
absorption rate may be higher despite the reduction in
nucleonic density.   An alternative equation is thus

$$W(r) = -W_o \cdot e^{(r-c)^2/b^2}$$

Again, neither W_o nor c are necessarily the same as in the previous equations. In the absence of experimental determination the former equation is more commonly used to define $W(r)$.

The effect of the potentials is seen when considering the incidence of a beam of particles of momentum p on a nucleus. The beam can be represented as a wave of wave number k (where $k = p/\hbar$), and wavelength λ (where $\lambda = \hbar/p$). As this beam enters the nucleus the wave number changes by k_1, and in the non-relativistic case with a constant nuclear potential then

$$k_1 = k \cdot ((1 + V/E)^{\frac{1}{2}} - 1) \quad \text{(Fernbach et al. 1949)}.$$

In the relativistic case

$$k - k_1 = k(1 + 2 \cdot V'/p\beta c + (V'/pc)^2)^{\frac{1}{2}}$$

The effect of the imaginary potential can be represented by the absorption coefficient K ($\propto W$), or the mean-free path for interaction in nuclear matter λ_N (where $\lambda_N = 1/K$).

The absorption coefficient for scattering by a nucleus, where scattering takes place on single nucleons of scattering cross-section σ is

$$K = 3A\sigma/4\pi R^3.$$

where R is the nuclear radius.
Therefore for an incident pion

$$K = \frac{3A}{4\pi R^3} \left(\sigma_{\pi-p}Z + \sigma_{\pi-n}(A - Z) \right) \qquad 1.2.2$$

or if capture by nucleon pairs predominates

$$K = \frac{3A\sigma_D}{4\pi R^3} \qquad 1.2.3$$

Experiments on pion-nucleus scattering revealed that the cross-section was not geometric. Two reasons for this have been suggested. One is that the cross-section could be increased by the coulomb effect, the negative mesons being attracted towards the positive nucleus resulting in a cross-section $\sigma_A{}'$.

$$\sigma_A = \pi R^2(1 - [1 - (1 + 2KR)\exp(-2KR)] / 2K^2R^2)$$

(Fernbach et al. 1949)

$$\sigma_A' = \sigma_A(1 \pm \frac{2Ze^2E}{R(pc)^2})$$

where E and p are the pion energy and momentum respectively. Alternatively Feshbach and Weisskopf (1949) suggested that the meson had a characteristic "size" equal to the reduced de Broglie wavelength λ yielding the new cross-section σ_A''.

$$\sigma_A'' = (\sigma_A^{\frac{1}{2}} + \pi^{\frac{1}{2}}\lambda)^2$$

At low energies where λ is large, the correction will be important and the nucleus will lose all its transparency as the size of the pion will be comparable with σ_A. Having measured the cross-section, and obtained K from equations 1.2.2 or 1.2.3, then the imaginary potential W can be calculated

$$W = \tfrac{1}{2}.hcK\beta$$

The change in wave number k_1 on entering the nucleus can be determined from the angular distribution of the scattered particles, and hence V' and W can be calculated.

1.3. Experimental Results.

a) <u>Nuclear Momentum Distributions</u>.   Some of the
earliest work which indicated a momentum distribution of
the nucleons, was work on the formation of deuterons,
where a nucleon from the nucleus unites with the incident
nucleon.   From observations of the emission angle and
energy of the deuteron, the momentum distribution of the
target nucleons can be obtained.   The fermi distribution
(eq: 1.2.1) for nucleon momenta with E_F = 25 MeV did not
produce the observed deuteron distribution, and from data
where the target nucleus was C^{12}, the following
distribution was derived, where $N(p)$ is the number of
nucleons with momentum p.

$$N(p) = \frac{8\pi \alpha}{(a^2+p^2)^{\frac{1}{2}}}$$

1.3.1

(Chew and Goldberger,1950)

with α^2 = 18 MeV.

A distribution was needed which would provide a
high momentum component, which the Fermi distribution does
not possess, and such a distribution had already been

derived from proton-nucleon scattering, where it had been assumed that the high momenta were contributed by the strong interactions between a pair of nucleons.

$$N(p) = \frac{e^{-p^2/\alpha^2}}{\alpha^2 \pi^{3/2}}$$

1.3.2

(Henley, 1952)

with $\alpha^2/2M \sim 14$.

The above equation (1.3.2) fitted the experimental results for deuteron pick-up satisfactorily.

Simultaneously the results of many nucleon-nucleon scattering experiments were being explained by the hypothesis of a distribution of nucleon momenta in the nucleus.

In one such experiment 314 MeV protons were incident on C^{12}, and the scattering and proton-nucleon cross-sections for scattering were determined. Attempts were made to fit the data using a Chew - Goldberger distribution (eq: 1.3.1), and an equation of the form

$$N(p) = C_A ((\alpha^2 + p^2)^2 \ (\beta^2 + p^2)^2)$$

1.3.3

where $\beta = 2.5 \ \alpha$, and C_A is a normalisation factor.

The above momentum distribution gave an average kinetic energy of 48.1 MeV for the nucleons, whereas a Fermi distribution with a P_{max} of 200 MeV/c would have an average kinetic energy of 12.8 MeV, which was not compatible with the experimental results.   However, the best fit was acquired with a gaussian distribution (eq: 1.3.2), which gives an average kinetic energy of 19.3, but any exclusion effect was ignored since it was expected to be observable only in the beam direction (Henley, 1952).

In later work (Winsberg and Clements, 1960) examining the theory of nucleon-nucleon scattering, it was assumed that the nuclear particles had the same nucleon-nucleon cross-sections as they would have had in the unbound state.   The only alteration being due to the Pauli exclusion principle.   Isotopic elastic scattering in the region 10 MeV - 6 GeV was investigated. Consideration of a Fermi gas of nucleons with E_F of 18.8 - 33.4 MeV, led to the conclusion that the data required an E_F of 48.1 MeV which implies a P_{max} of 303 MeV/c for the nucleons, which is far above the accepted range of values.

Extensive investigations of the nucleonic momentum distribution have been made using quasi-elastic scattering. This is scattering of an incident particle by a bound nucleon, which at the moment of impact is considered to act as a free particle with its nuclear momentum.

Before 1958 quasi-elastic p-p scattering was already being considered as a means of obtaining information about the nuclear structure (Maris et al. 1958). The nucleons were considered to make only one collision within the nucleus, and thus needed a high energy and small de Broglie wavelength. It was decided to use closed shell nuclei with assumed j-j coupling in the shells. If the last shell is not filled, the collision can leave the residual nucleus in one of many states so that the energy balance is not unique. The exclusion principle would not have an observable effect for incident nucleons of above 400 MeV. The results obtained in a quasi-elastic experiment were expected to be similar to those from deuteron pick-up except that the latter probably favoured surface nucleons and hence higher momentum components, whereas quasi-elastic

scattering would sample throughout the nucleus. The method involved the simultaneous detection of two secondaries of equal energies and emission angles ($\sim 45°$ to beam direction) when a proton beam was incident on light nuclei. A series of such experiments were carried out in different laboratories.

At 185 MeV the binding energies for the s and p shells of light nuclei were measured (Tyren et al. 1958). These are compared in Table I with values obtained by other workers performing similar experiments and within the estimated errors the results agree. A table of the experimentally determined values of the binding energies of light nuclei has been drawn up by Ajzenberg-Selove et al. (1959), which includes the Tyren et al. results.

Among attempts to fit momentum distributions for the nucleons in these experiments were the following. For 660 MeV protons on beryllium and C^{12}, the Fermi distribution was rejected outright because of the lack of high momentum components, and three other distributions were tried (Azhgirey et al. 1959).

Projectile energy	Target	Binding energy p shell. MeV.	Binding energy s shell. MeV.	Reference
155 MeV	Li^6	4.5 ± 1.5	20.3 ± 1.5	a
155 MeV	Li^7	10.2 ± 1.6	23 ± 1.5	a
185 MeV		10 ± 1.5	24 ± 1.5	b
185 MeV	Be^9	18 ± 1.5	25 ± 1.5	b
155 MeV	B^{10}	7 ± 1.1	31.5 ± 1.5	a
		13 ± 1.2		
155 MeV	B^{11}	10.4 ± 1.6	34 ± 3	a
		15.2 ± 1.7		
		14 ± 1.5	37 ± 5	b
155 MeV	C^{12}	15.8 ± 1.2	34.5 ± 1.5	a
158 MeV		17		d
185 MeV		16		e
		17 ± 1.5	35 ± 1.5	b
185 MeV	N^{14}	8 ± 1.5		b
		16 ± 1.5		
185 MeV	O^{16}	12 ± 1.5		b
		19 ± 1.5		

Results of proton quasi-elastic scattering.

a) Garron et al. (1962)
b) Tyren et al. (1958)
d) Gottschalk and Strauch (1960)
e) Gooding et al. (1960)

TABLE I

1) a gaussian. $N(p) \propto e^{-p^2/\alpha^2}$ 1.3.4

    with $\alpha^2/2M$ = 16, 18, 20 and 22 MeV.

2) a Selove distribution. $N(p) \propto e^{-p^2/a_1^2} \pm 0.15e^{-p^2/a_2^2}$

    with $a_1^2/2M$ = 7 MeV, a_2^2 = 50 MeV.   1.3.5

3) sum of two gaussians. $N(p) \propto e^{-p^2/a_1^2} + e^{-p^2/a_2^2}$ 1.3.6

The best fit was in fact obtained using 1.3.6 with $a_1^2/2M$ = 16 MeV, $a_2^2/2M$ = 50 MeV and β = 0.09. For copper and uranium targets multiple collisions prevented detection of the nucleon energy.

     For light elements with 155 MeV incident protons the following two distributions were tried as a result of a preliminary Born approximation calculation.

    for the s shell. $N(p) \propto e^{-p^2/a^2}$ 1.3.7

    for the p shell. $N(p) \propto (p/a)^2 \cdot e^{-p^2/a^2}$ 1.3.8

By adjusting a a satisfactory fit was obtained for the energy distribution of the secondaries, the final values of a are shown in Table II.

α in MeV	Li^6	Li^7	B^{10}	B^{11}	B^{12}
s shell	110	115	120	120	160
p shell	110	70	80	90	95
Garron et al. (1962)					
p shell					74
Gottschalk & Strauch (1960)					

Experimental determinations of α for nucleon momenta distributions

$$N(p) \alpha \quad e^{-p^2/d^2}$$

TABLE II

1.3.6 was used successfully to explain the quasi-elastic interactions of 660 MeV protons on C^{12} (Zhadonov and Fedotov, 1961).

The quasi-elastic scattering interaction

$$p + C^{12} \rightarrow Be^8 + p + \alpha$$

has been studied at 150 MeV. Rejecting free helium collisions the momentum distribution of the emitted α was studied for a fixed momentum transfer, $q = 2.0$ fm^{-1} and $E_\alpha = 22.5$ MeV. It was concluded that the ground state of C^{12} probably could be described completely in terms of a cluster model, but the experiment was not accurate enough to derive an expression for the α momenta, (James and Pugh, 1962).

Further in the reaction

$$p + C^{12} \rightarrow p + n + C^{11}$$
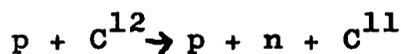
the recoil momentum will be equal in magnitude and opposite in direction to the target nucleon momentum before the collision. For incident proton beams of 0.25 to 6.2 GeV the recoil momentum was independent of

the incident energy and corresponds to an average kinetic energy of 19 MeV, which agrees with the deuteron pick-up results, (Sarjant Singh and Alexander, 1962).

Deuteron sub-units in the nucleus have been studied using the reaction

$$\delta + N \rightarrow N' + p + n$$

where the momenta of the out-going particles can provide information about the quasi-deuteron momenta. Further, the reaction

$$\gamma + N \rightarrow N'' + p$$

yields information about the binding energy of the protons. To form deuteron sub-units the nucleons should be within a radius $\hbar/\mu c$ (μ is the pion rest mass), and this is more probable for nucleons belonging to the same shell than for those from different shells. Kim (1963) examined the experimental results existing for C^{12}, assuming that the pairing for 1s nucleons was stronger than for the 1p ones. He obtained the following distributions and binding energies

1s nucleons E_B = 20 MeV

$$N(p) = (3\pi M)^{-3/2} \exp(-p^2/3M) \qquad\qquad 1.3.9$$

1p nucleons E_B = 5 MeV

$$N(p) = (2\pi^{-\frac{1}{2}}/3)(10M)^{-5/2} \exp(-p^2/10M) \qquad\qquad 1.3.10$$

deutrons $N(p_D) = (0.37 \exp(-p_D^2/4ME_1)/(4\pi ME_1)^{\frac{1}{2}}$

$$+ 0.82 \exp(-p_D^2/4ME_2)/1.5 (4ME_2)^{2.5} \qquad\qquad 1.3.11$$

where E_1 = 1.5 MeV E_2 = 5 MeV

The different quasi-elastic proton-proton experiments
give compatible results for the binding energies of the
nucleons in the s and p shells of the light nuclei.
These binding energies of 10 - 30 MeV are not completely
contradicted even when deuteron subunits only are
considered as in Kim's work. Both the deuteron pick-up
experiments and the incident proton work at 0.25 to
6.2 GeV suggest an average nucleonic kinetic energy of
19 MeV which is inconsistent with the Fermi distribution.

Finally the distribution of nucleon momenta indicated by
both deuteron pick-up and quasi-elastic scattering from
100 - 660 MeV is of a gaussian form with α always in the
region of 100 MeV.

 b) <u>Nuclear Potentials</u>. In the quasi-elastic
scattering experiments, no accurate determination of the
potential has been made. Table III shows the only
measured values.

 It has been pointed out by Strnad (1962) that
although distributions of the form shown in 1.3.7 and
1.3.8 can, with a suitable choice of α , be fitted to the
cross-section curves, estimates of the binding energy
based on these distributions differ greatly from the
measured values. Using the observed binding energies and
potential well form factors, curves were fitted to the
results of Garron <u>et al</u>. for Li^7 and C^{12} with the radius
of the potential well, r, as the variable parameter. The
nuclear potential can then be estimated from the equation,
and in fact the potential radii which gave the best fit
almost coincide with radii found by high energy electron
scattering (see Table IV).

Projectile	Energy	Target	Potential in MeV.	
p	660 MeV	Be	30	Azhgirey et al.1959.
		C^{12}	30	
p	0.25 - 6.2 GeV	C^{12}	37 - 45	Sarjant Singh and Alexander, 1962.

Estimations of the Nuclear Potential from Experimental Results.

TABLE III

	By experiment		From equation		Variable parameter	
	B_s MeV	B_p MeV	V_s MeV	V_p MeV	r_s fm	r_p fm
Li^7	23.5	10	43	25	2.5	4.5
C^{12}	36	16	79	40	1.6	3.4

B - binding energy

V - potential well depth

	re_{ff}(fm)	r_{equ}(fm)
Li^7	3.5	3.5
C^{12}	2.94	3.0

re_{ff} - effective potential radius

r_{equ} - equivalent radius from electron scattering

(Hofstadter, 1956)

TABLE IV.

1.4.   Pauli Exclusion Principle Effects.

a) <u>General Outline</u>.   The Pauli exclusion principle
forbids any two Fermions to occupy identical energy
states.

The effect of the exclusion principle on the
refractive index of nuclei at high energies was examined
by Glauber (1956).   Glauber stated that to find the
effective scattering properties of nucleons in nuclei, it
is better to use the position correlations of the
particles in the Fermi gas than their momentum distribution.
Correlation which keeps similar particles apart, leads to
destructive interference effects, and at low energies the
nucleon-nucleon cross-sections in the opacity expression
are smaller than the free particle cross-sections.   At
high energies ($\lambda <$ nucleon-nucleon range) shadowing and
multiple scattering effects also become important.   In
this case the tendency of nucleons to stay apart increases
their effectiveness as collision targets.   Therefore
the nucleon-nucleon cross-sections for nuclear opacity
are greater than the free nucleon-nucleon cross-sections
by a term proportional to

$$\frac{i.f^2(0).\ p^2_{max}}{p^2}$$

where p is the initial momentum.

This term changes sign when

$$Im|f(0)|^2 = Re|f(0)|^2$$

The effect of nucleon separation is exactly the inverse to that which causes non-additivity of cross-sections, as for example in deuterium, where the nucleons are drawn together.

Examining proton collisions with a 30 MeV proton beam, Elton and Gomes (1957) concluded that the exclusion principle does not operate in the diffuse rim of the nucleus where the nucleons are almost free, and their momentum can be represented by a gaussian function (e.g. 1.3.2).

The exclusion principle tends to freeze particle motion and to minimise the effects of the excitation of small clusters (Bruecker, 1958). If however, all the lowest energy levels are not filled, small momentum transfers can take place, moving nucleons into unoccupied

positions. Alternatively the nucleus can be considered
as a Thomas-Fermi gas, where the density is given by

$$\rho(r) = 2/\hbar^3 . \, 4\pi/3 \, . \, p_F^3(r) \qquad\qquad 1.4.1$$

where $p_F(r)$ is the maximum momentum at radius r.
If $N > Z$, then the neutron density has a larger radius than
the proton density (Oda and Harada, 1958).
Electron scattering data indicate that

$$\rho(r) = a(\exp((r-c)/b) + 1)^{-1} \qquad\qquad 1.4.2$$

where a is a normalisation factor, c is the half-way
radius, and b is a diffuseness parameter with b = 0.57
f and c = $1.1 \text{x} A^{1/3}$f. $p_F(r)$ can be obtained from 1.4.2
and 1.4.1. Estimating the potential for an incident
proton, the differential cross-section for scattering can
then be calculated. In the nuclear region chosen, the
exclusion principle was found to make no difference to
proton-nucleon scattering at 31 MeV, and fairly satisfactory
agreement was obtained with the experimental points.

In estimating the effect of the exclusion principle
at high energies Karplus and Yamaguchi (1961) used a

gaussian momentum distribution for uncorrelated nucleons
(incident energies 300 MeV). Their value of α was
168 MeV/c (see 1.3) for incident nucleon energies between
15 and 26 GeV. They neglected the effect of nuclear
binding on cross-section except to the extent which the
Pauli exlcusion principle and coherent effects, reduce
the quasi-elastic scattering at very small angles. They
obtained a distribution width

$$\frac{p.\Theta.p_{max}}{M}$$

for the secondary nucleons at angle Θ due to the Fermi
motion of the nucleons, and then considered a degenerate
Fermi distribution making a gaussian approximation to the
average fraction, f, of states not available to a nucleon
when it receives an impulse $p\Theta$.

f is given by

$$f = \left(1 - \frac{p\Theta}{2p_{max}}\right)^2 \cdot \left(1 + 1/4 \cdot \frac{p\Theta}{p_{max}}\right)$$

$$\sim \exp\left(-1.25 \cdot \frac{p^2\Theta^2}{p^2_{max}}\right)$$

$$= \left(-\frac{5}{2} \cdot \alpha \cdot p^2\Theta^2\right)$$

Scattering at angles such that $p\theta \gtrsim 2p_{max}$ is only slightly reduced, but the amplitude of the momentum spectrum is reduced by a factor $(1 - \exp(-5p^2\alpha\theta^2/2))$. This gives the same effect as if the struck nucleons were smaller scatterers than free nucleons.

Watson and Zemach (1958) performed a Monte Carlo calculation for pions incident on a nucleus. They found an effective mass for the pion, as the dispersive nature of the medium alters the magnitude of the pion flux and the density of the states. However, their calculations did not agree with experimental results.

Further calculations have been carried out for π-nucleon scattering, above 600 MeV, which disagree with Watson and Zemach's results. The calculations indicate an increase in cross-section due to the exclusion principle, and in the limit agree with Glauber's earlier calculations. They also give good agreement with the experimental results in this region (Baqui Bég, 1960).

b) <u>300 MeV Meson Interactions with Complex Nuclei</u>. Continuing observations on the interactions of π^- mesons in complex nuclei, this laboratory analysed the scattering

of a 300 MeV π^- beam incident on a G5 emulsion stack.
Previously at 750 MeV and 4.2 GeV the optical model of
the nucleus was used to explain the results and
satisfactory agreement was obtained using a reduced meson
size (Allen et al. 1961; Clarke and Major, 1957).   At
300 MeV (Finney et al. 1962) and 88 MeV (Allen et al. 1959)
however, the value of K, the absorption coefficient,
obtained differed greatly from the theoretical value.

For 300 MeV the observed value of K was 3 to 4 times
smaller than the expected value.   140 metres of track
were scanned, and 255 elastic events including 42
disappearances were found.   Thus the mean-free-path for
elastic scattering ($\geqslant 5°$) was (77 $\pm$ 5.8) cm.   The
forward-backward ratio, F/B, is the ratio of the number of
mesons emitted in the forward direction, that of the
incident beam, to the number emitted in the backward
direction.   The value obtained experimentally was
F/B = 0.74 $\pm$ 0.17 for stars with secondary mesons.
Misclassification would increase the elastic mean-free-
path by a maximum of 12% and decrease the inelastic
mean-free-path by 5%.

The mean interaction cross-section in emulsion is

$$\bar{\sigma} = \sum (N_i \sigma_i)/\sum N_i \qquad\qquad 1.4.3$$

where there are N_i nuclei/cm of the ith element whose interaction cross-section is σ_i.

Using the observed inelastic mean-free-path, 1.4.3 and 1.2.3, a value for K was obtained

$$K = (1.5 \pm 0.15).10^{12} cm^{-1}.$$

which gives $\lambda_N = 6.7 \pm 0.7. 10^{-13}$ cm, and an opacity of 66%. Thus the mean-free-path in nuclear matter is calculated to be (1.5 x nuclear radius).

Calculations performed with the individual free nucleon cross-sections (75 $\pm$ 5.6 and 32 $\pm$ 2 see earlier) give $K = (5.2 \pm 0.3).10^{12} cm^{-1}$.

Because of the long mean-free-path in nuclear matter only one scattering of the projectile is expected to occur, and therefore the relative probabilities of scattering and absorption are 30% and 70% respectively. Adding the expected values of K (scattering) and K (absorption) in these proportions leads to an expected

value which agrees with the observed value.

$$K = K_{scatt} + K_{abs} = (1.9 \pm 0.2). \; 10^{12} cm^{-1}$$

The average kinetic energy of the secondary mesons was 107 MeV (corresponding to E = 250 MeV and p = 205 MeV/c). For secondary pion energies greater than 85 MeV, then the average kinetic energy was (164 ± 26) MeV, and the F/B ratio was (1.1 ± 0.35), which corresponds to the following nuclear potential components:-

$$V'(r) = (25 \pm 1) \; MeV$$

$$W_o(r) = -(14 \pm 1) \; MeV$$

The observed and calculated K values could be brought into agreement only if r was reduced to $1.12.10^{-13} cm$, when the values were both $9.3 \; 10^{12} cm^{-1}$. However this value of K would imply that the meson makes on average about five collisions in the nucleus. Also this high value for K predicts an average energy for the secondary mesons of about 70 MeV, not the observed 107 MeV, and the value for r_o is outside the accepted

range.   The results are consistent therefore with a
single collision within the nucleus, with absorption not
scattering as the predominant feature.   The cross-section
for interaction of a meson with a single nucleon is
however smaller by a factor of 3.

If the mean energy of the scattered π^- mesons is
plotted against the laboratory angle of scattering, then
in the forward direction the energy is found to be much
lower than would be observed if the struck nucleons were
stationary.   This suggests that small momentum transfers
are forbidden, and that the exclusion principle is
operating within the nucleus.   Describing the nucleon
states within the nucleus using a Fermi momentum
distribution, it proved impossible either to account for
the reduction in cross-section of about 3, or for the F/B
ratio of about unity (Finney et al. 1962;   P.G.J.T.
Parkhouse, M.Sc. Thesis, Durham University).

1.5.   Monte Carlo Calculations.

Metropolis (1958) performed nuclear cascade
calculations for heavy nuclei, Al, Bi, U, etc.   The

earlier calculations were made for incident protons and neutrons of 82 to 365 MeV, and were general Monte-Carlo calculations picking a point of entry to the nucleus, and then following the particle until absorption occurred or it escaped. The Fermi model of a degenerate gas was used to describe the nucleus, comprising a nuclear volume whose radius was $R = rA^{1/3}$. The degree of forbiddenness of a collision depended on whether or not the resulting energy of the nucleon was less than E_F. Overall good agreement was obtained both quantitatively and qualitatively with the experimental results.

The calculations were then extended for incident energies of up to 1.8 BeV and incident pions, pion production, scattering and absorption were included. The calculated emission angle spectra of protons agreed well with the experimental results except at angles $< 10°$. However, for pions the emission spectra did not agree. At smaller angles of emission the calculations gave far too many high energy pions, which had the effect of raising the average kinetic energy. In fact, the experiments indicated that small energy transfers were

being prohibited thus reducing the forward scattering.
For example, for 500 MeV π^- incident on heavy emulsion
nuclei the calculated average kinetic energy was 174 MeV,
but the observed average was 110 MeV.   For 162 MeV π^-
a similar discrepancy was observed, but it was not as
great.

An attempt was made to follow a suggestion of
Nikol'skii's (1957) and to introduce a pion-nucleon
potential.   With an attractive potential of 18 MeV the
agreement was better for the energy spectrum of the
secondaries.   Any secondaries with negative kinetic
energy were assumed to be absorbed.   However, the angular
distributions still did not agree, and the calculated
distribution was not isotropic enough.   It was thought
that the introduction of a diffuse nuclear boundary, also
suggested by Nikol'skii, might remedy this.

Bertini (1963) followed up this work by introducing
such a nuclear boundary effect into the calculations.
The diffuse nuclear boundary was approximated to, by
dividing the nucleus into three concentric spheres of
decreasing density as the radius increased.   In each
region the nucleus was assumed to be behaving as a

degenerate Fermi gas, but the overall effect approximated
to a gaussian distribution with a kT of 15 MeV. This
agreed well with experimental results (see 1.3), and it
appears that the detected distributions are partly the
effect of varying nuclear density.

Here, the pion potential was assumed to equal the
potential of the struck nucleon, and again collisions were
forbidden, if a nucleon energy occurred below E_F. The
results agreed well with experimental data for incident
nucleons as long as $A \leqslant 12$, except that again more small
momentum transfers were expected than observed. The
pion data however, showed large discrepancies, the most
extreme being for charge exchange. It was postulated
that the discrepancy might be due to the incoherence
indicated by the resonance in the pion-nucleon cross-
section.

1.6. Pion Potentials

In 1958 Watson and Zemach performed a series of
calculations, which gave the momentum of the pion within
the nucleus. This momentum had two components, and from

this it was possible to calculate the pion potential corresponding to a particular pion kinetic energy. Their calculations were for the 10 to 400 MeV region. Their results however, only gave qualitative agreement with experimental data.

Nikol'skii (1957) estimates the pion potential for a kinetic energy of 160 MeV as $V = -(24 \pm 6)$ MeV. The minus sign indicating that the potential is attractive. It was also found that a change in V of 30 MeV led to a change in kinetic energy of 7 MeV for backward scattered pions. In Table V a list of experimentally determined pion potentials are shown. Within experimental error the values are consistent, but the accuracy is not high.

1.7. Reasons for this Experiment.

It is obvious that theory and experiment do not agree on the results of pion interactions with complex nuclei. Previous work at 300 MeV (see 1.4) had shown that the optical model was not applicable, and no explanation of the results other than that a Pauli effect might be responsible for the discrepancy, could be found.

Experimentally Determined Pion Potentials

Energy	Particle	Target	V	V_i
48	$\pi^{\pm}$	C	$-(15 \pm 15)$	
62	π^-	G5	$-$	~ -19
80	π^+	G5	$-$	~ -24
120	$\pi^{\pm}$	G5	$-$	~ -24
70	$\pi^{\pm}$	C	~ -18	~ -9
78	$\pi^{\pm}$	Cu	$\sim -(35 - 40)$	~ -20
80	π^+	Al	~ -20	$\sim -(10 - 25)$
80	π^-	Al	$\sim -(30 - 40)$	$-$
88	π^-	G5	$-(28 \pm 3)$	$-(32 - {}^{+20}_{-6})$
300	π^-	G5	(25 ± 1)	$-(14.1 \pm 1.4)$
60	$\pi^{\pm}$	He	$-(20 \pm 10)$	$-$
62	$\pi^{\pm}$	C	-18	$-$
105	$\pi^{\pm}$	He	$-(18 \pm 14)$	$-$
125	π^-	C	-30	$-$

All values in MeV.

Values taken from tables in

Nikol'skii et al. (1957)

Allen et al. (1959)

Finney et al. (1962)

TABLE V

However, in order to be able to construct a model for the struck nucleons it is necessary to have more accurate data on the emitted pions. This means measuring large numbers of inelastic scatters quickly and accurately.

Making normal $p\beta$ measurements on secondary tracks from interactions is a slow process, as each track has to be aligned along the traverse of the stage. Scattering measurements and grain counts have then to be made on the track in order to identify it, and if the tracks are steep, passing rapidly into another plate, measurements are impossible. Often the track cannot be resolved as definitely belonging to a pion, but could be that of a charged particle of higher mass. Also in cases of charge exchange, positive and negative pions cannot be distinguished.

The spectrograph, described in chapter 2, uses a magnetic field to sort the charged particles. Thus using an incident pion beam, only a negligible number of the secondaries which have negative curvature will not be pions. Also using this method, of the order of 100 tracks per scanner per day, can be measured.

The experiment was thus planned in the hopes of

obtaining energy and angular distributions with good
statistics. From these distributions, the discrepancies
between the experimental results and the prediction of
a particular model, could be accurately determined, and
the model altered or rejected accordingly.

1.8. Basic Calculations made for the Present Experiment.

These calculations were based originally on a
classical model of the nucleus as an association of
isotropically moving nucleons. A pion of momentum π_1,
and energy W, is incident on this nucleus, and collides
with a nucleon, moving with momentum P and energy Wp, at
an angle α to the direction of motion of the pion. The
resultant momenta and angles of emission can then be
calculated.

The centre of mass of the two particles is found,
and the cross-section corresponding to the centre of mass
momentum of the pion is calculated, using the differential
cross-section $(d\sigma/d\Omega)$ of 1.9, and the equation

$$d\sigma^{\pm} = 2.\ \sin\alpha.d.\alpha.\sin\theta.\frac{d\sigma}{d\Omega}.\pi./(\text{number of angular}$$

$$\text{intervals)} \quad 1.8.1$$

where θ is the angle of emission.

A table is then drawn up showing the cross-section for scattering into a certain angular interval with a given momentum for that value of P. Each table contained the total cross-section for 18 values of α from $0 - 180°$. The calculations were then repeated using a different P. P ranged from $25 \rightarrow 475$ MeV/c in 50 MeV/c intervals and α in $10°$ intervals from $5°$ upwards.

Three nucleon momentum distributions were assumed, giving the fraction F with momentum P.

a) the Fermi with $F = 3.P^2.dP/P^2_{max}$

with $P_{max} = 240$ MeV/c.

b) the gaussian with $F = 2.e^{-P^2/\alpha^2}.dP/\pi^{\frac{1}{2}}.\alpha.$

with $\alpha = 191$ MeV/c.

c) a composite with $F = 4.P^2.e^{-P^2/\alpha^2}.dP/\pi^{\frac{1}{2}}.\alpha^3.$

with $\alpha = 191$ MeV/c.

Sets of cross-section tables were then produced for each distribution. Summing over all tables for a distribution gave the total cross-section.

Cut-offs could then be applied by forbidding collisions in which the secondary momentum or energy of the struck nucleon failed to satisfy some chosen condition.

The calculations were carried out originally on the Ferranti Pegasus computer at the University of Newcastle-on-Tyne. Subsequent adaption of the cross-sectional tables was done on the Elliott 803 computer of Durham University.

1.9. Pion Interaction Cross-Sections.

In order to calculate the effect of the Pauli exclusion principle in π-nucleon collisions, detailed information on the π-nucleon cross-section is required.

For a pion incident on a free nucleon, the differential cross-section in the centre of momentum at an angle Θ, can be represented by the following series

$$\frac{d\sigma}{d\Omega} = A + B.\cos\Theta + C.\cos^2\Theta + D.\cos^3\Theta + \dots \quad 1.9.1$$

where A, B, C, etc. are functions of the phase shifts at the energy under consideration. It is possible to obtain expressions of the form

$$A = a + bq + cq^2. \qquad\qquad 1.9.2$$

for each of these functions, where a, b and c are numerical constants, and q is the momentum of the pion. The terms of 1.9.1 are of decreasing importance, and only the first three or four need be considered.

In order to obtain the constants a, b and c, and thus be able to calculate the differential cross-section, experimental values for A, B, C and D were plotted for various values of q. These experimental values were obtained from the following papers:- Deahl et al. (1960, 1961), Kellman et al. (1963), Zinov and Korenchenko (1959), Ashkin et al. (1956, 1957), Helland et al. (1962) and Yuan (1956). The curves were plotted for both π^--P collisions (Fig. 1a) and π^+-P collisions (Fig. 1b). Assuming charge independence the π^+-P curves also apply to π^--N collisions. The constants were found for equation 1.9.2 by curve fitting to the experimental
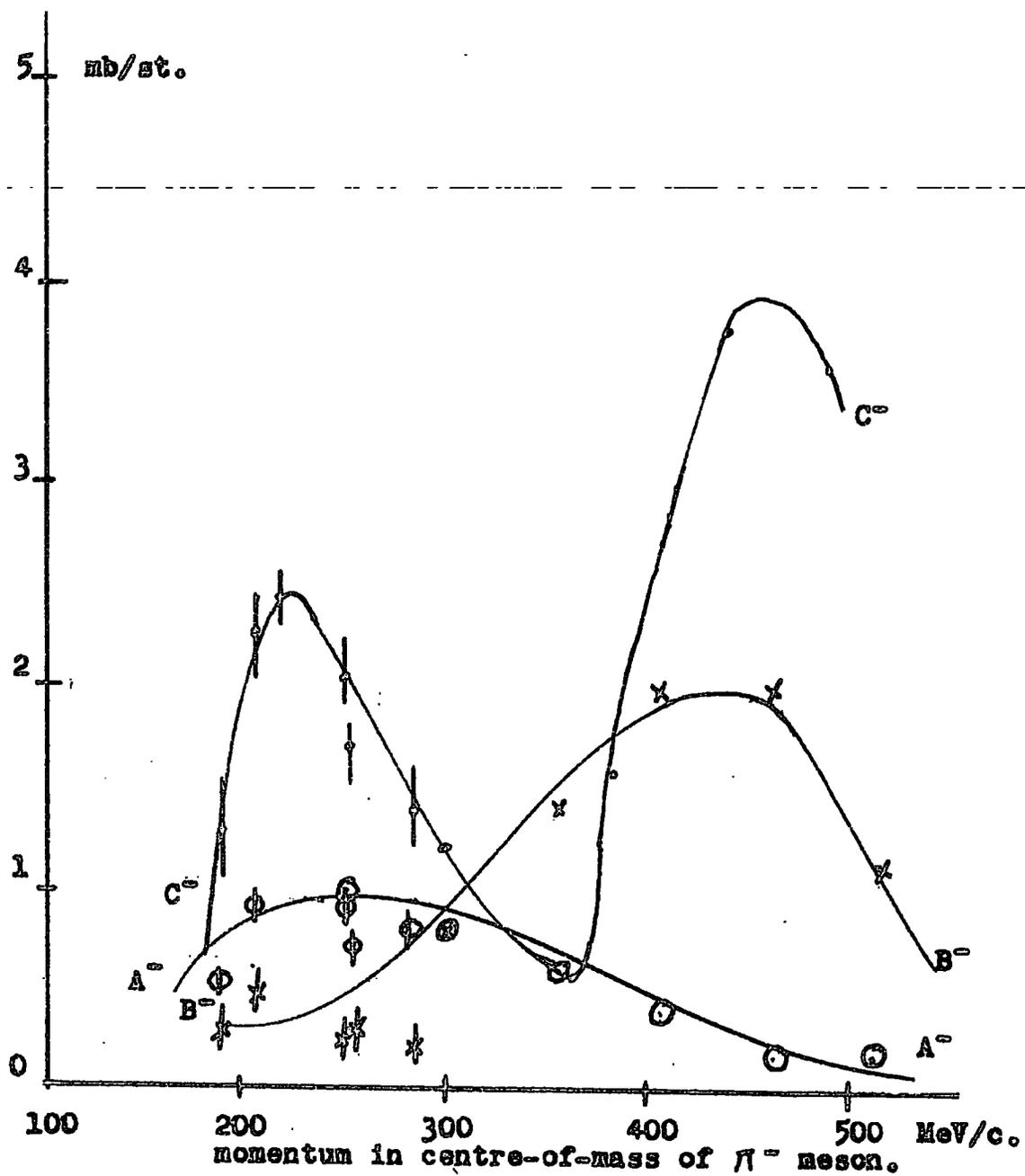
Cross-section 𝛑⁻-P scattering.

Figure 1a

Cross-section π^+-P scattering.

momentum in centre-of-mass of π^+ meson.
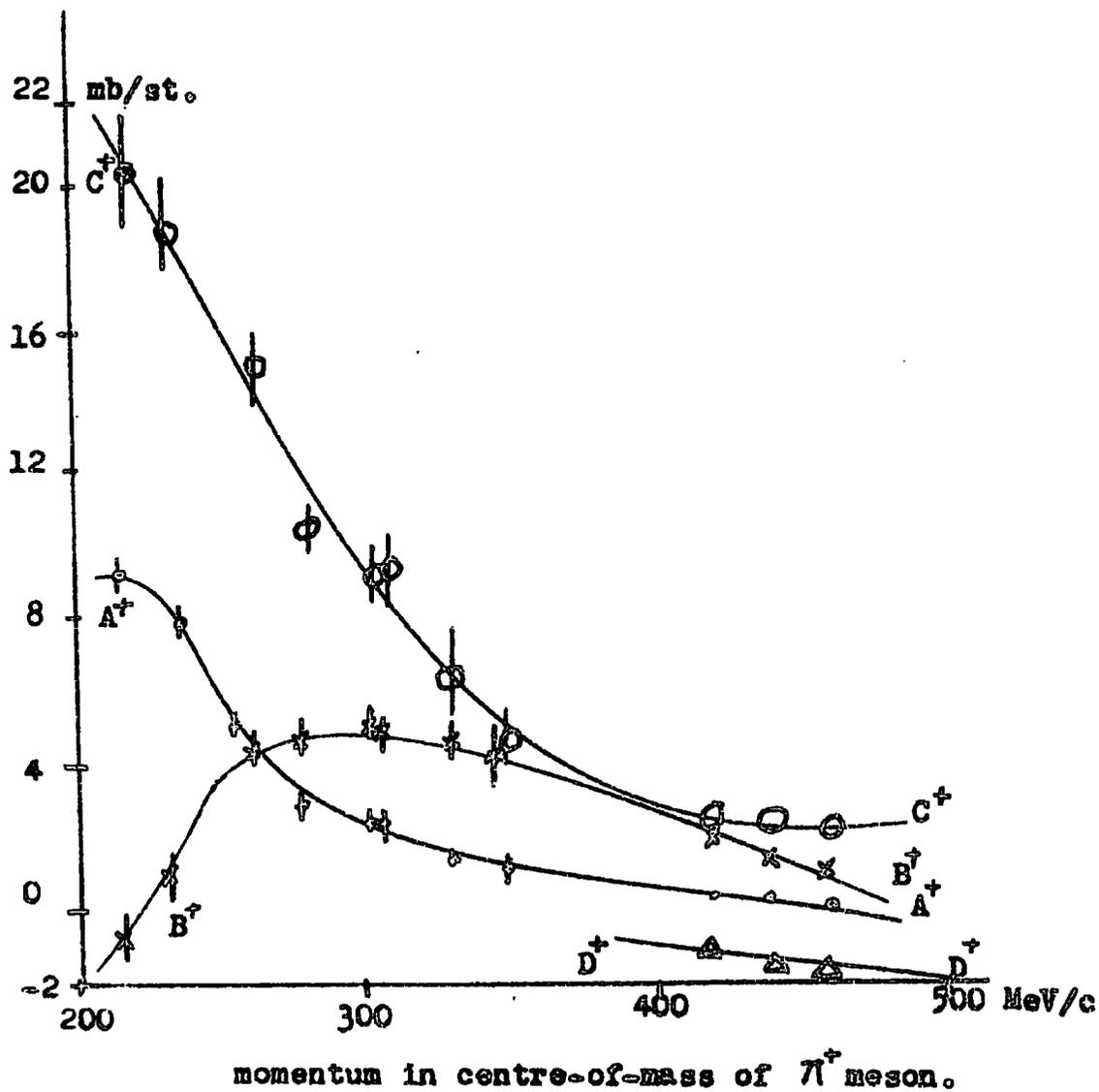
Figure 1b.

q range in MeV/c	f_i	a	b	c
q < 270	A	-15.997	+0.29850	-0.00082
	B	-30.203	+0.13453	0
	C	-0.368	+0.32098	-0.000986
q < 250	D	0	0	0
250 < q < 355	D	-1.724	+0.029	-0.000088
270 < q < 460	A	+29.565	-0.13209	+0.000150
270 < q < 355	B	-22.128	+0.17528	-0.0002735
	C	+76.36	-0.3235	+0.000349
355 < q < 460	B	+12.30	-0.01481	-0.0000114
	C	+61.27	-0.2810	+0.000349
	D	+41.096	-0.2218	+0.00028

where $f_i = a + bq + cq^2$.

and the f_i are the phase shift functions in the equation

for the differential cross-section.

TABLE VI

points.   The expression for pi-nucleons cross-section is
the sum of $\pi^- P$ and $\pi^- N$ cross-sections.   The constants
for A, B, C and D are shown in Table VI for the various
ranges of q.

1.10.   Some Results of the Calculations.

a) Effect of nucleonic momentum distributions on
the scattering of pions.   In figure 2a, is shown the
energy of the pion as a function of scattering angle
resulting from a pion collision with a stationary nucleon,
at a pion energy of 300 MeV.   Compared with it are the
mean energies of pions for scattering angles determined
from the calculations outlined above.   In the
calculations the collisions are with moving target
nucleons.   It is found that for the Fermi and the
composite Gaussian distributions, the mean energies are
almost exactly equal to each other, and very close to
that of a pion scattered from a stationary target.

The differential cross-section for scattering on a
stationary nucleon becomes modified as seen in figure 2b,

where the nucleon is allowed to move according to the Fermi and composite Gaussian distributions.

b) <u>The effect of the nuclear potential</u>. The nuclear potential experienced by pions has been described in table V (section 1.6) and is shown in figure 2c. In the same figure, the relation between kinetic energy within and without the nucleus is shown. The potentials were determined experimentally for several nuclei, and it is assumed that they are constant throughout the periodic table. Since the potential varies with energy, it introduces a considerable modulation on the mean energy of the scattered pions.

A primary pion of 285 MeV is reduced to 260 MeV inside the nucleus. Therefore the scattering of a 260 MeV pion is the reaction being investigated. Using the Oxford Kinetic Tables, the energy of the secondary pion within the nucleus can be found after the collision with a stationary nucleon. As this pion leaves the nucleus there is a further potential effect which can be estimated using figure 2c. The expected modulation for a pion-stationary nucleon collision is shown in figure 2a,

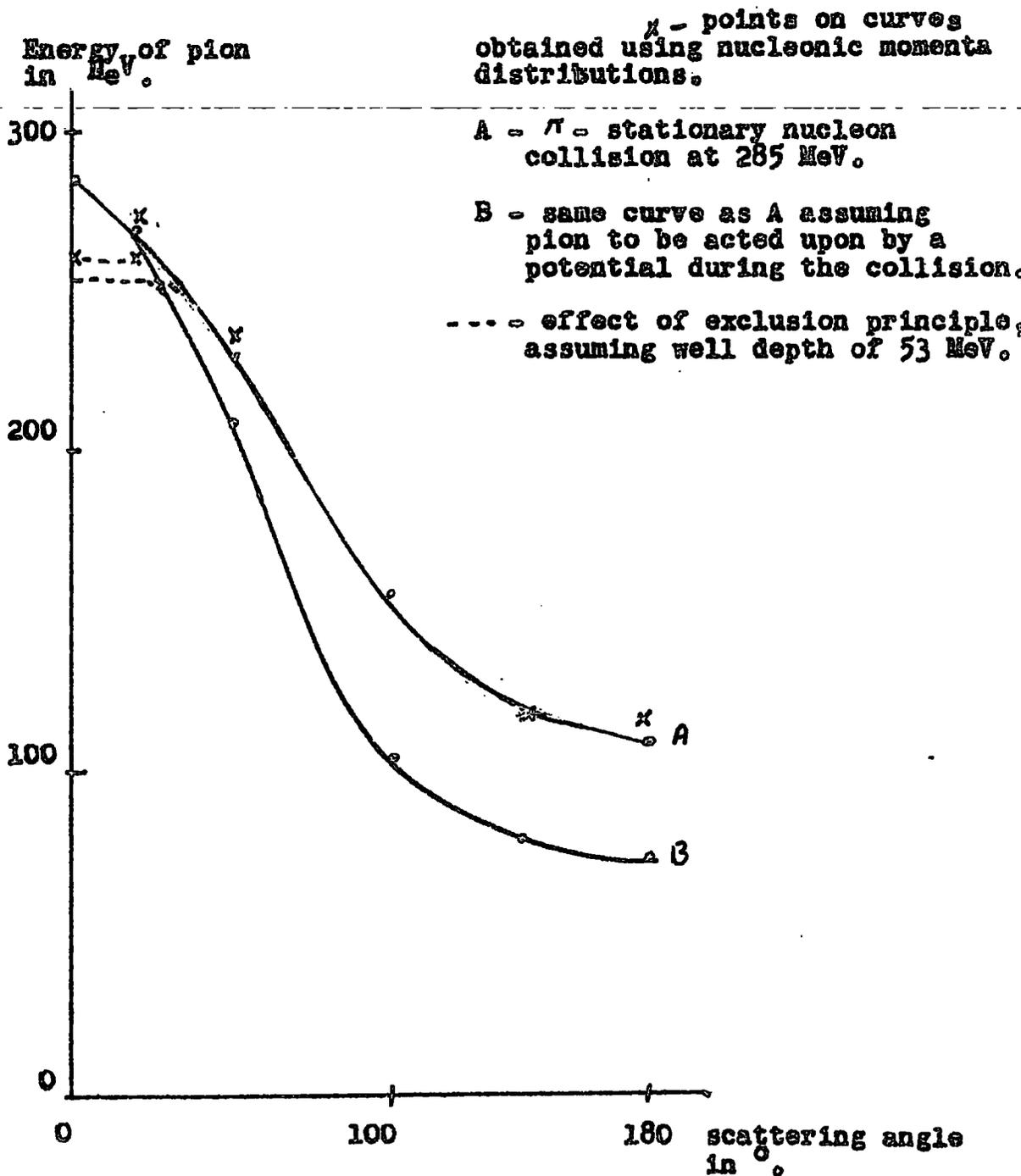Variation of Mean Energy with Scattering Angle.

Figure 2a.

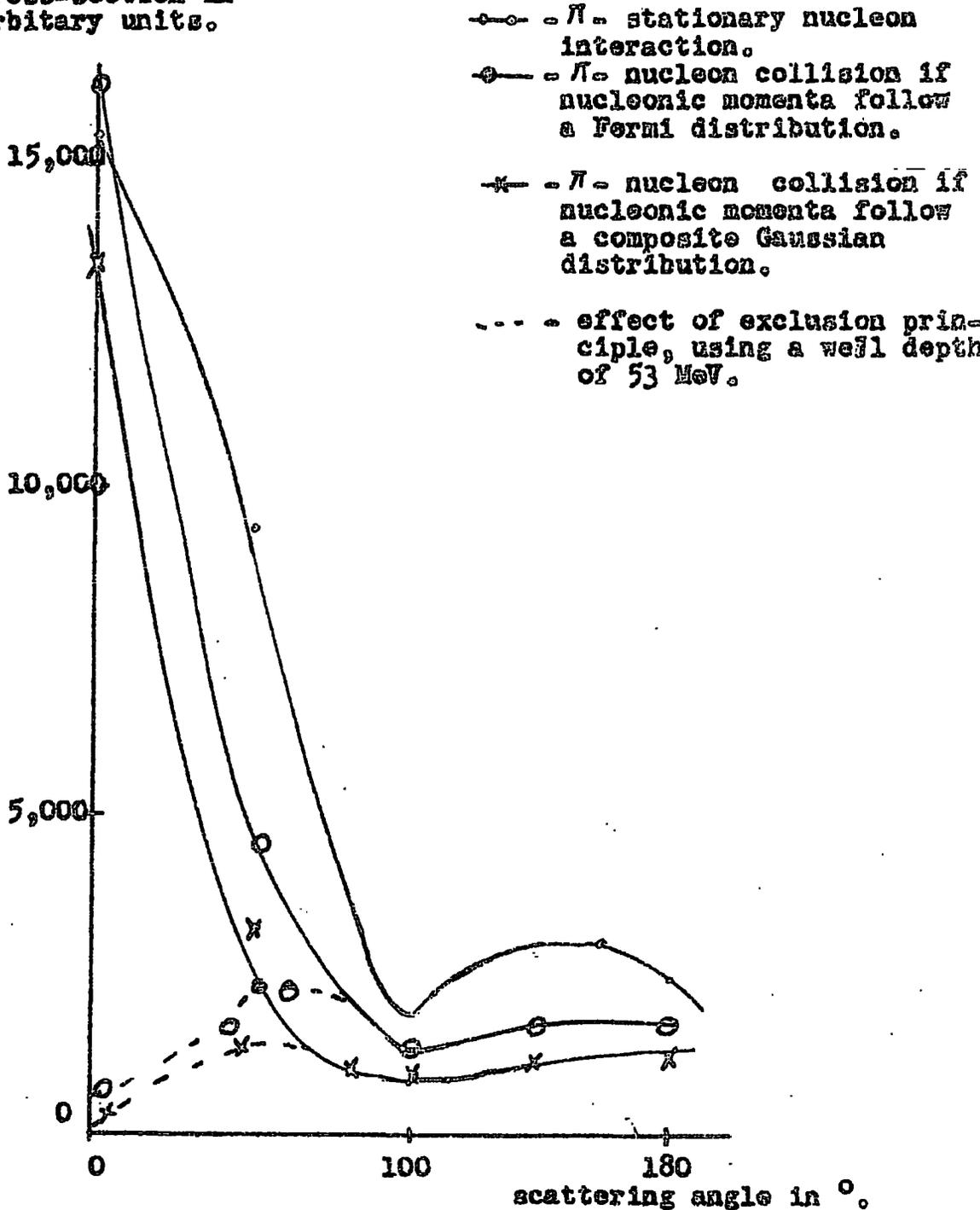Variation of Cross-section with Scattering Angle.
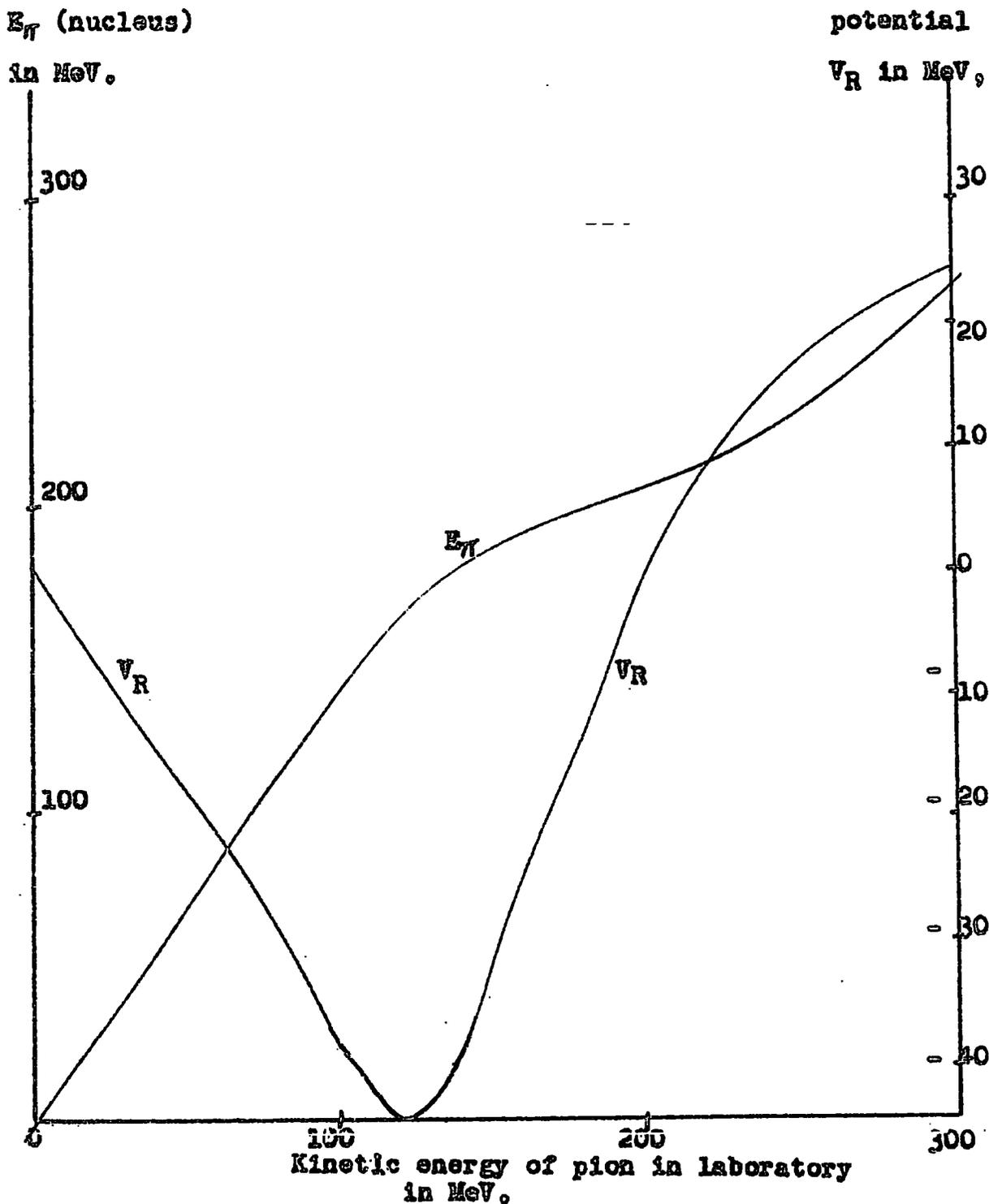

Figure 2b.

Figure 2c.

where it is seen to be most pronounced at larger angles
of scattering.   In a similar manner using the assumed
momentum distributions, the potential effect can be
determined, and the modulation of the mean energy curve
is in fact the same whether the nucleons are considered
to be stationary or distributed over a momentum range.
The modulation depends on the shape of the potential
curve in figure 2c.

c) <u>Exclusion effects</u>.   The exclusion principle
inhibits small momentum transfers of momentum, so that
it depresses the scattering through small angles.   For
the Fermi and composite Gaussian ($p^2 e^{-p^2/\alpha^2}$) distributions
the effect is shown in figure 2b, where the reduction of
forward scattering is plainly seen.   Using the Fermi
model, the reaction was assumed forbidden under different
conditions.   If a momentum restriction was assumed, such
that the nucleon must be raised to 240 MeV/c if the
reaction was allowed, a decrease of the forward cross-
section was obtained, but not of the mean energy.   The
other two momentum distributions tried gave the same
result.

If a nucleonic potential well is assumed of depth V, then the energy required by the nucleon to escape is (V- K.E.), where K.E. is the kinetic energy of the nucleon in the nucleus. Using the exclusion principle, a collision will be forbidden if the energy transferred to the nucleon is not enough to allow it to escape. An example of such an energy limitation is shown in figure 2b, where it can be seen that the effect becomes negligible at around 70°. In figure 2a, the effect on the mean energy of the scattered pions is shown.

d) <u>Distribution of momenta at a fixed angle of scattering</u>. The effects of momenta distributions of the struck nucleons is seen to be negligible if average effects are considered. For example, the mean energy and mean cross-section of the scattered pion are virtually unchanged. However, the differential cross-section is smeared out. So are the individual momenta of the secondary pions as is shown in figure 2d. Here as an example, the scattering of 290 MeV pions through 90° is shown. The effect of the momentum distribution is to broaden the line spectrum by about $\pm$ 150 MeV/c.

Momentum Spectrum at a Given Scattering Angle.

Expected spectrum at 90° of secondary pions, if the
nucleons have a composite Gaussian distribution of
momenta with a maximum p around 275 MeV/c. No
corrections have been made for potential or exclusion
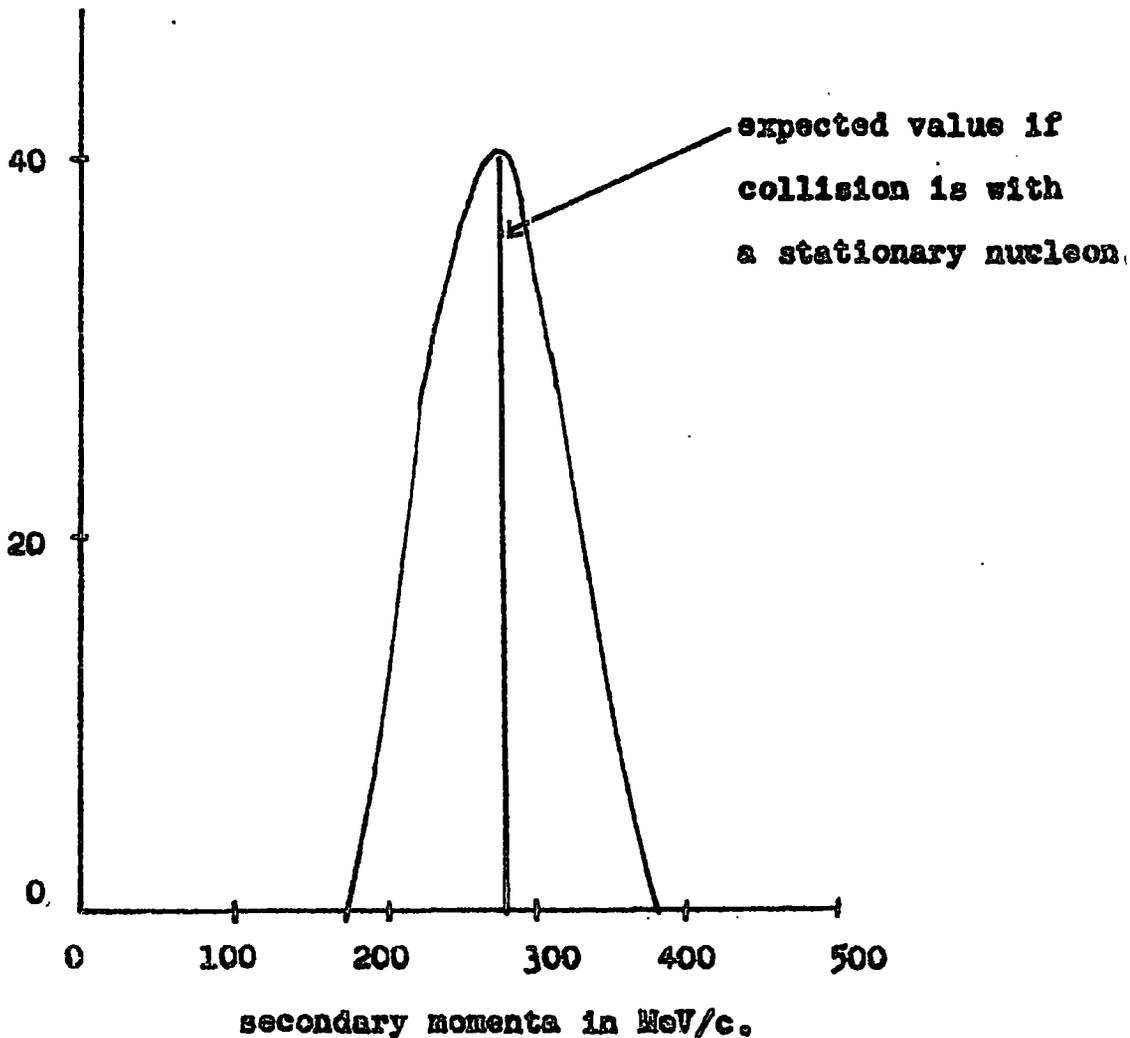effects. Incident pion momentum is 290 MeV.

Number of tracks.

Figure 2d.

Exclusion effects which are small at 90° have been
excluded.

2.   THE SPECTROGRAPH.

2.1.   The Principle of the Spectrograph.

As was stated in the first chapter, section 1.7, the emission angles and momenta of the secondaries from a pi-nucleus interaction are required with good statistics.   The ideal system would have cylindrical symmetry and would consist of a point target set in a magnetic field and surrounded by a circular detecting device.   The detecting device in this case being flat sheets of nuclear emulsion in the plane of the magnetic field.

The beam enters the system and strikes the target. The secondaries then strike the emulsion at an angle to the perpendicular to the surface, and pass through, out of the spectrograph.   Knowing the central target point and the angle of the track in the emulsion, it is possible to determine $\mathcal{E}$ the angle of emission.   If ε is the horizontal, and ε' the vertical component of the angle of emission, then:-

$$\cos \mathcal{E} = \cos \varepsilon . \cos \varepsilon'. \qquad 2.1.1.$$

By placing the spectrograph in a magnetic field an estimate of the particle momentum p, can be made. A singly charged particle in a magnetic field of strength H, will describe a circular trajectory with radius of curvature R, perpendicular to the field direction, where:-

$$p = 300.H.R. \quad eV/c \qquad\qquad 2.1.2$$

If ρ is the chord of this circle from the target, O, to the point of contact with the emulsion, Z, (see Fig. 3b) then:-

$$\sin \phi = \rho/2R. \qquad\qquad 2.1.3$$

and from 2.1.2 and 2.1.3 -

$$p = \frac{300.H\rho.}{2.\sin \phi}$$

With a known magnetic field, H, p can be calculated if ρ and ϕ are determined by measurement.

The presence of the magnetic field will give antitropic curvature to the tracks of oppositely charged particles. Thus from the angle in the emulsion it will
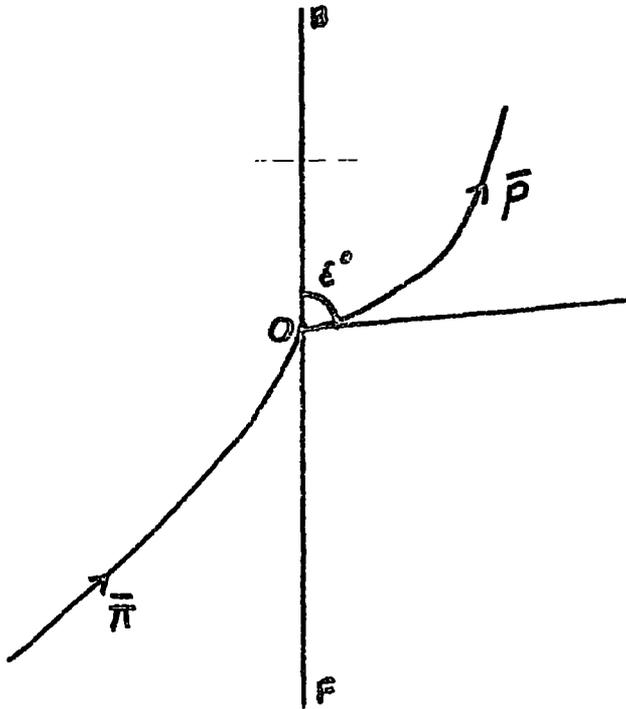
BF - the perpendicular to
      the target face.

O - the point of scattering
      in the target.

FIG: 3a. Horizontal Plane of Interaction.

O ～ point on the target,

Z ～ point on the plate.

FIG: 3b. Trajectory of a Particle in a Magnetic Field.

be possible to distinguish the tracks of negatively charged particles and to make measurements only on these tracks. Therefore pions which undergo charge exchange are automatically excluded.

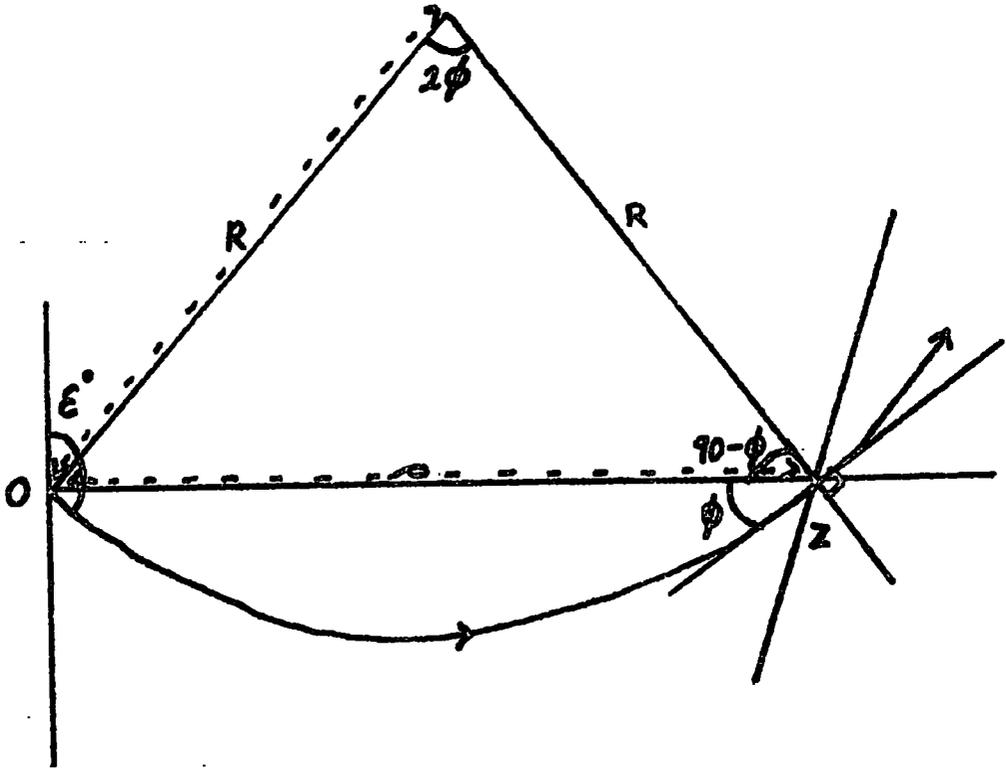With regard to the magnetic field, there were two requirements, a steady constant value over the area of the spectrograph and a value high enough to render the curvature of the tracks easy to detect and measure. It was obvious that the smaller the radius of the spectrograph the easier it was to have a constant value for the field strength over the experimental area, but the deflection of the particle would be very small and the curvature of the track hard to detect. Also the finite size of the target necessitated having a large radius (see below). The value of the field required was of the order of 10 kilogauss.

Particle Flux. One of the most important factors affecting the choice of the radius of detection, is the flux per unit area of detector. If the incident pion flux on a target of thickness t, is F, then the total path length is Ft. Therefore the number of inelastic events giving rise to secondaries is:-

$$\frac{Ft}{\lambda}$$

where λ is the interaction path length. If d is the radius of the circle on which the detectors are set, the flux per unit area per pulse is -

$$\frac{Ft}{\lambda \, 4 \, \pi \, d^2}$$

The maximum tolerable flux is about 2.10^3 particles per cm. The time to obtain this is then -

$$\frac{\lambda \, 4 \, \pi \, d^2 \, . \, 2.10^3}{Ft}$$

This time should be as short as possible in order to keep the background low, and so that the experiment is feasible with regard to the use of a beam from a high energy accelerator for this exposure. Obviously once F is the maximum possible, the time depends on the ratio between d and t. This ratio is very important because on it depends also the size of the error in the determination of p (see later). If t is large compared with d then the errors on both p and E increase.

The highest flux of 300 MeV negative pi-mesons was obtainable from the C.E.R.N. synchrocyclotron, where a beam of the order MeV had already been built. The flux was quoted at about 4.10^4 π^- per second over an area of 6 x 8 cm^2. On a target of 2 x 2 cm^2, this is 4.10^3 π^- per second. λ for inelastic scattering is 3 x 38 cm (for scattering with an emergent pion), and taking d as 5 cm and t as 1 cm, this requires an exposure time of 6 hours; whereas for the same t but with d increased to 10 cm, the exposure time is 22 hours. Hence in adjusting d and t to the practical optimum some sacrifice in accuracy was necessary in order to achieve better statistics and vice versa.

2.2. The Actual Spectrograph.

In practice the ideal system of a central point target surrounded by a circular detector can only be approximated to. The aim is to set a finite target in the centre of a circle of frames, which support flat nuclear photographic emulsion in a vertical plane (see Fig. 4). Each frame supports a glass coated on both
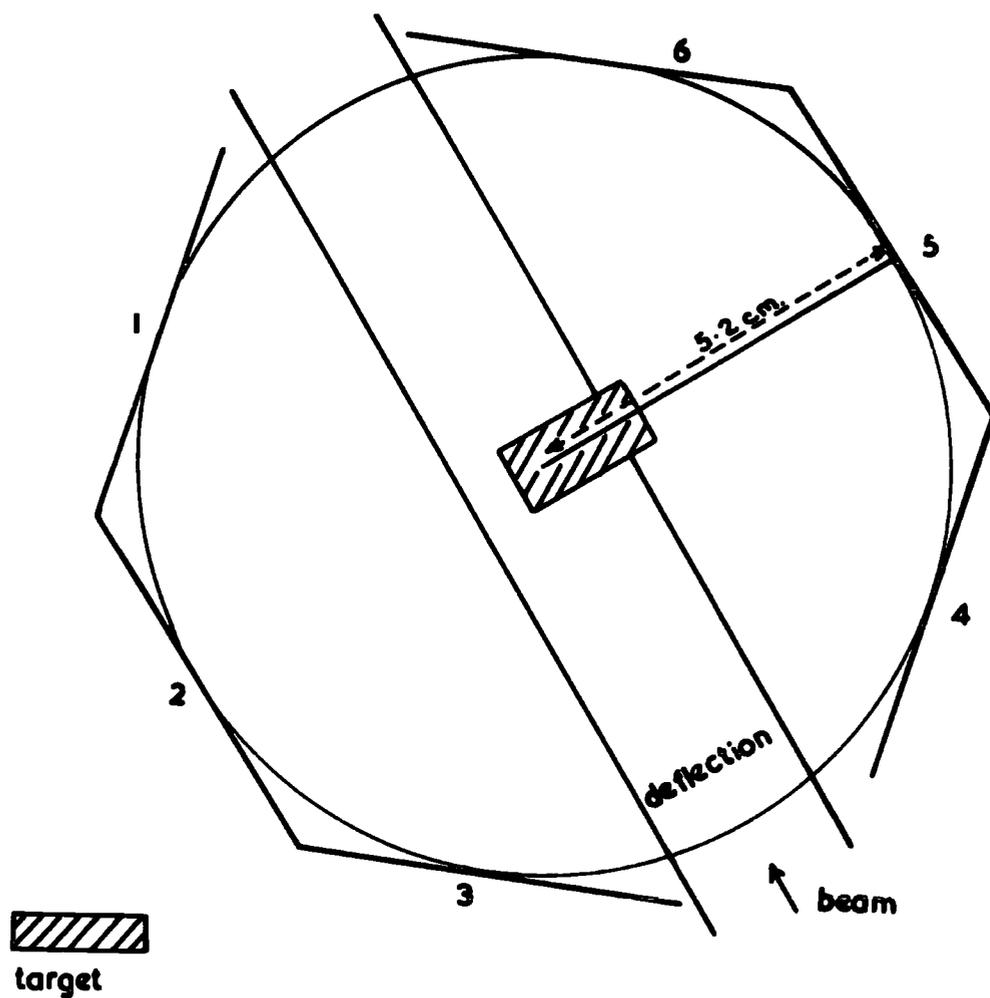
target

Diagram showing layout of

six plates and target

Target dimensions are 2cm x 1cm x 5cm.

Figure 4

sides with nuclear emulsion. The position of each frame

must be located accurately, so that a frame can be

removed, and replaced in exactly the same position. To

achieve this accuracy a three point locating system was

used.

Each frame is set along a tangent of the detection

circle, radius d. The equations in section 2.1. have to

be modified, since they assumed cylindrical symmetry.

Let Θ now be the angle in the horizontal plane which the

track makes with the perpendicular to the plate at the

point of entry, Z, (see Fig. 5a). It is necessary to

determine for each plate both d, the length of the

perpendicular from the target to the plate, and the

position D, where this perpendicular reaches the plate.

For each track then, Θ, and x the horizontal co-ordinate

of the track relative to D, can be measured. Thus -

$$\tan(\Theta - \phi) = x/d. \qquad 2.2.1.$$

and ϕ is the only unknown in the equation. Also

$$\rho = (x^2 + d^2)^{\frac{1}{2}} \qquad 2.2.2.$$

and by substituting for ρ and ϕ in 2.1.4 p can be found
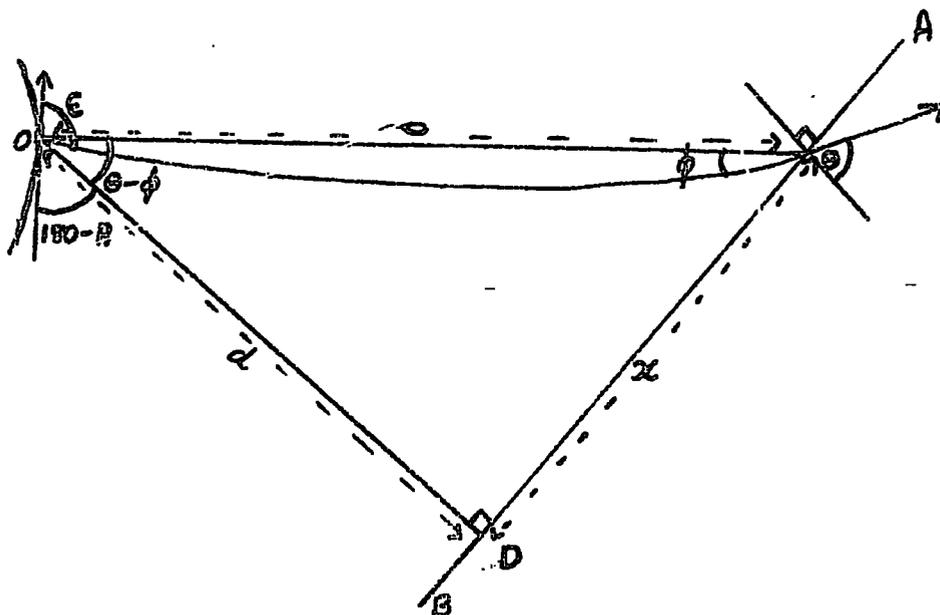
a) The Geometry of the Trajectory in a Horizontal Plane.

b) Co-ordinates of a point Z.

Figure 5.

if the point of emission is known (see chapter 4).

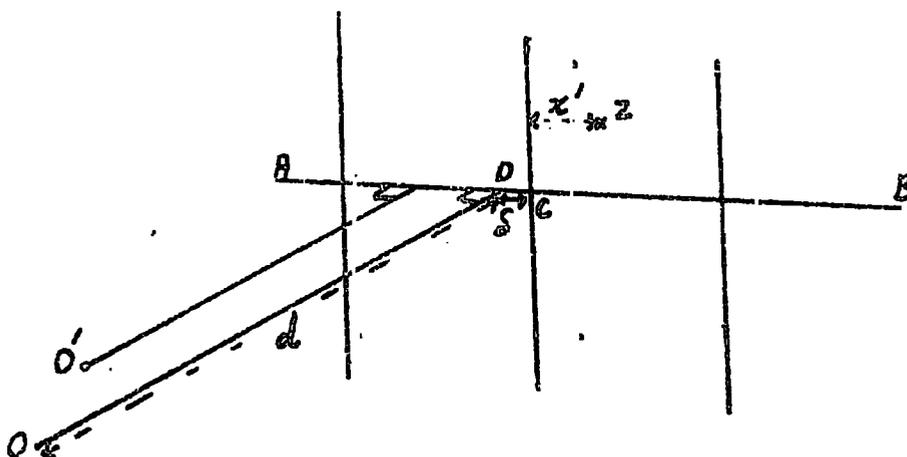$\mathcal{E}'$ can be obtained from measurements on the track in the emulsion since the vertical angle is unaffected by the magnetic field. Let d make an angle A with the emerging unscattered beam. Then

$$\mathcal{E} = A - (\Theta - \emptyset) - \emptyset \qquad\qquad 2.2.3.$$

Θ and $\emptyset$ may be positive or negative depending on the charge of the particle and the segment of the detecting circle in which the frame is located. In fact it is no longer possible by simple visual inspection to separate positively from negatively charged particles (see Fig. 6), for two reasons. Firstly, the fact that the frame lies along a tangent to the detection circle means that tracks reaching opposite edges of the frame appear to have different curvature even when they have the same momentum. Secondly, because the target has a finite size, if all tracks are assumed to have come from the target centre then some negative particles will appear positive and vice versa (see chapter 4).

Once d has been determined, $\mathcal{E}$ and p may be estimated
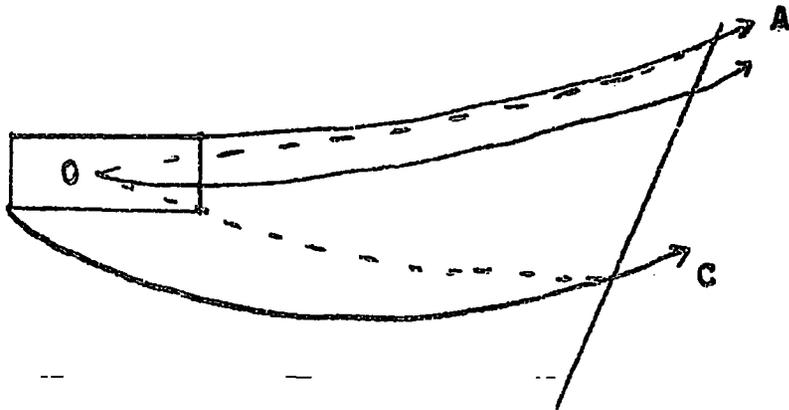
a) The effect of emission from a different centre. If
all are considered as coming from O, then A is estimated
to have a different curvature and C a higher momentum
than is the actual case.
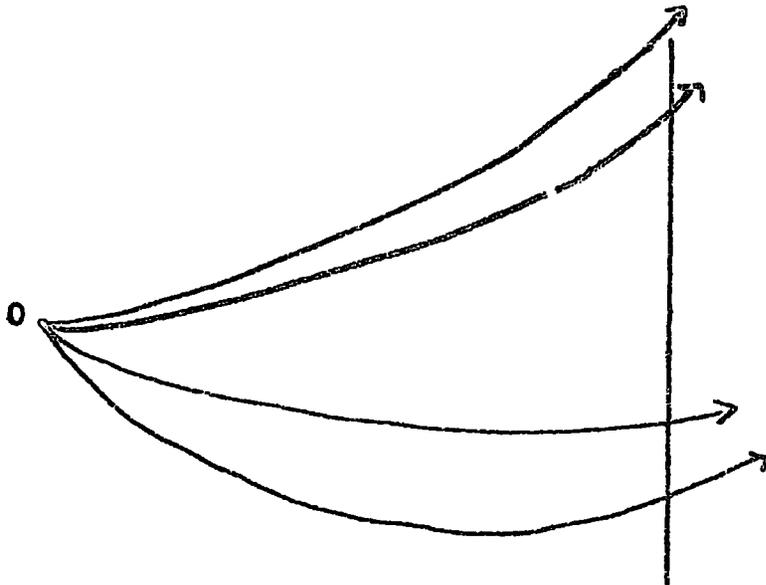
b). Pairs of particles emitted at the same spatial angle
with different momenta.

Figure 6.

from the co-ordinate measurements made for each track.

Accuracy

Misalignments of the frames. Small misalignments
of the frames would very quickly introduce large errors
into the evaluations. Examples of misalignments are
shown in Fig. 7, where A-B is the emulsion plane.

In a) Θ is the actual angle of the track with the
perpendicular to the emulsion, if the plate is correctly
aligned. When misaligned by $\delta\emptyset$ the error in momentum is
given by:-

$$P = p\left(1 - \frac{\sin\Theta}{\sin(\delta\emptyset + \Theta)}\right)$$

and if $\delta\emptyset = 1°$, then the error at 400 MeV/c is 102 MeV/c.
However, by accurately determining the plane of the plate
this error can be reduced to below 40 MeV/c.

In b) one end of the frame is higher than the other.
As long as $\delta\emptyset$ is less than 0.5° the error in p is
negligible, and the error in the angle of emission is
about $(0.3 \times \delta\emptyset°)$.

From c) it can be seen that if the plate is inclined
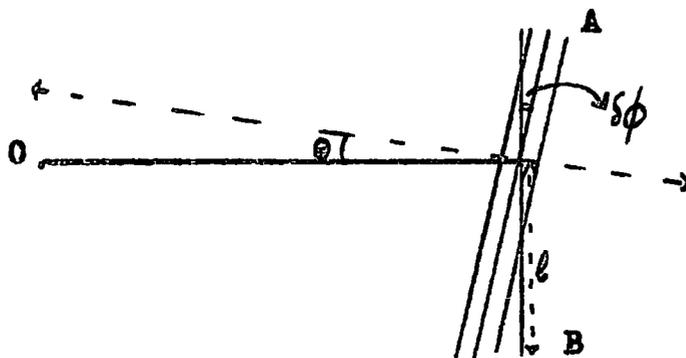
a). Plate inclined in plane of curvature of track.
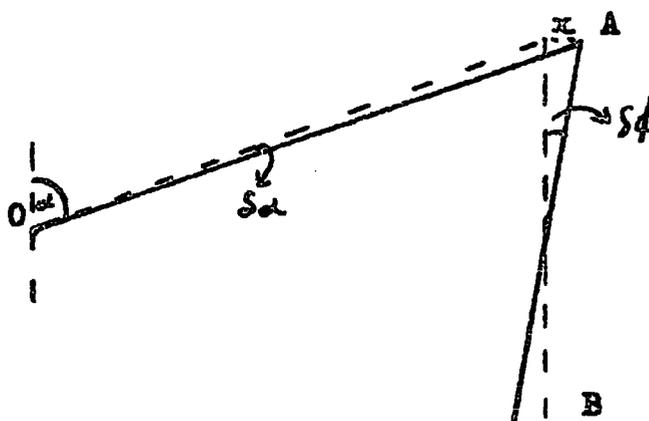
b). Plate not horizontal, one end higher than the other.
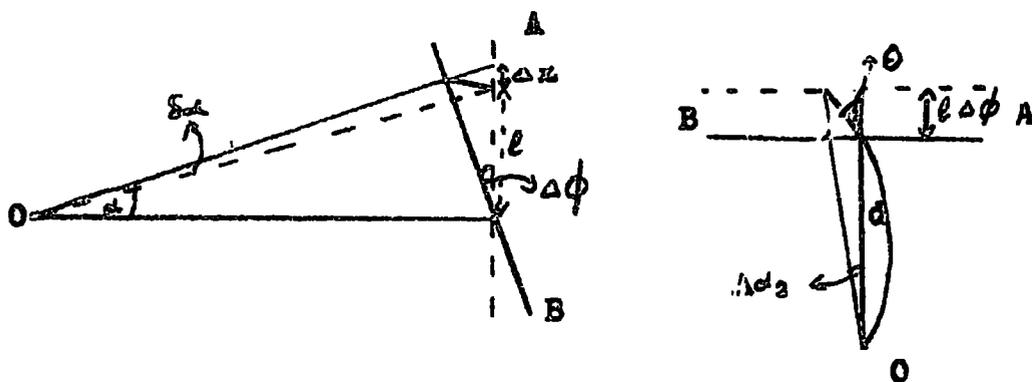
c). Plate inclined towards target in vertical plane.

Figure 7.

towards the target in the vertical plane, then the error in p is of the same order as that introduced by the increased target size. The error in the angle of emission is $(0.3 \times \delta\phi \times \tan\theta)$, and is 1°, if θ equals 45° and $\delta\phi$ is 5°.

Obviously when the alignment of the plates was known accurately, corrections could be made to all measurements.

Target Size. All the equations given above assume that the particles are emitted from a known point in the target. For a finite target this is obviously not the case. From Figure 5 it can be easily seen that moving the point of emission from O to some other point O', alters completely the reference system used to obtain the co-ordinates of any track in the emulsion. The length d is altered and also the point D where the perpendicular meets the plate, and hence the curvature of the track cannot be estimated without knowing the point of emission. Similarly the horizontal angle of emission relies on a knowledge of the point of emission. The vertical angle of emission is unchanged and can still be accurately estimated. To cope with this problem of the finite target size, a new method of analysis was introduced

(see chapter 4), and proved successful.

Accuracy of Measurements. The error introduced during measurement of the track angles in the plates was very small. The track could be located to within 3μ under the magnification used, which would introduce a maximum error of 6% for high energy particles, for low energy particles the error is about 1%. On travelling through the glass and the emulsion, the particles will lose energy due to multiple scattering. Because of its greater thickness more scattering takes place in the glass. The errors arising from uncertainty in location and scattering lead to a total maximum error in p of 15%. The maximum error in ξ is of the order of 2°.

2.3. The Construction of the Spectrograph.

The target for the exposure was to be set on an accurately machined brass base, which could then be used to locate and position the frames carrying the emulsion. The height of the target was determined by the spacing of the magnet faces, (see below) and the final dimensions were $2 \times 1 \times 5$ cm^3, the face presented to the incident beam being 2×5 cm^2.

The Frames.   In order to reconstruct accurately the particle trajectory, it is necessary to know the position of the track relative to a co-ordinate system in each plate, and also the relationship between the co-ordinate systems of the different plates and the centre of the target.   The determination of these relationships is termed 'calibration'.   This calibration must be permanent, and to achieve this, the construction must be such that individual plates can be removed from their positions, and replaced without destroying the exact relationship between them, in order to be able to measure accurately the track deflection, and to make it possible to coat, process and examine each plate separately. Since the deflection of the particles is perpendicular to the field, the plates must be supported vertically.

A kinematic method of locating the frames on the supports is employed using a hole, a groove and a plane (Fig. 8).   The grooves and holes are cut in appropriate positions on the upper surface of brass pillars, placed behind the edges of the frame to eliminate as much back scattering into the plates as possible.   The complementary
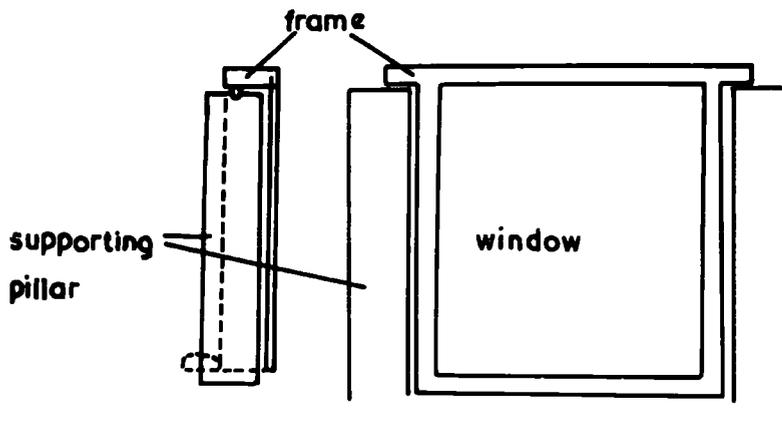
a) sectional drawing showing frame on supporting pillars
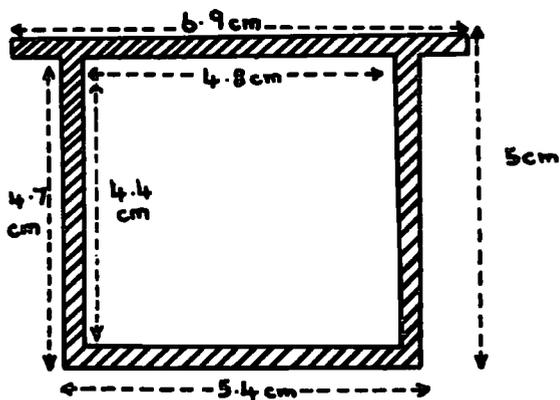
b) front of frame
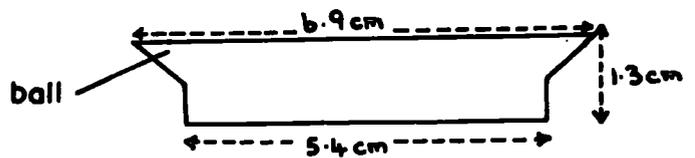
c) top of frame

Figure 8.

members of the location on the frames are steel balls 2 mm in diameter attached one at each end to the underside of the supporting extension. The balls are attached in a⁻position slightly removed from the axial plane of the frame, so that under its own weight the frame rests with its lower end against a projection; this constitutes the third member of the location. This method of accurate location has already been used successfully in this laboratory (Allen and Apostalakis, 1961). Great care is taken to ensure that the frames are perpendicular to the brass base when resting in position on the supports. Ideally, the kinematic location should be solely under a gravity constraint but, to avoid the possibility of movement of the plates while being inserted between the magnet poles, they are clamped by exerting pressure against a small ball on their upper surfaces. Just sufficient pressure is exerted to prevent movement; no deformation of the system is introduced thereby. Even with this additional constraint, the position of each frame is reproducible to better than 1μ.

In all three sets of six frames were accurately

machined for two exposures and a dummy run, plus an additional two spare frames. The detecting circle comprises two semi-circles of three frames each around the target.

The glasses were affixed to the front of the frames by gluing round the edges of the glass, and holding the glass permanently against the frame with a metal clamp screwed to the side of the frame.

The Plates. Each plate consisted of a specially coated glass about 800μ thick, with an emulsion 100μ thick, stuck onto both surfaces. The thickness of the glass being accurately determined for each plate. The basis of the co-ordinate system is a grid of fine lines ruled on one surface of the glass of each plate. For the greatest usefulness of the spectrograph the accuracy of the calibration should be of the order of 1μ.

By means of an engraving diamond a reference grid was inscribed on the glass surface nearest the target, and the calibration carried out with the frames in position. The grid is a single line across the plate horizontally, with three lines perpendicular to it at intervals of about 1.5 cm, the intervals being known

exactly for each frame, and the lines being perpendicular to within 5'. The distances of the crossing-points on the grid from the target centre were measured accurately using travelling microscopes, with each frame in its correct position. The frames and their positions are correspondingly numbered, to ensure correct replacement. From these measurements d, and the point D, where this perpendicular meets the plate relative to the grid can be ascertained.

Once the emulsion had been affixed to the glass, they were covered with black paper to shield them from all light.

<u>Calibration</u>. As has been shown each plate now has a fixed position relative to the target centre. d is known, and its distance from any recognisable point, C, on the grid in the same horizontal plane (see Fig. 5b). When scanning the plates the co-ordinates of C were recorded, and the co-ordinates of each track can be obtained using C as the origin. If the co-ordinates of a track at Z, are (x', y') with respect to C, then -

$$x = x' + d \qquad\qquad 2.3.1.$$

and hence ρ in 2.2.2 can be found.

2.4. The Magnetic Field.

A field strength of the order of 20 kilogauss was required over the target and frames, in order to facilitate observation of the required tracks. At this field strength, even a 300 MeV pion would undergo an easily detectable deflection ($> 1°$) over a distance of 6 cm. Also low energy particles would suffer large deflections. For example, the protons emitted from the target would have a much lower momentum than the pions, and many of them would thus move in tight spirals, never reaching the plates, and therefore not adding to the background.

To achieve this high field over the detectors a pair of metal cones was attached to the magnetic poles. The cone faces were held at a fixed distance of 5.5 cm apart by three metal spacers bolted on (see Fig. 9). The face area of the cones was the detecting circle of the spectrograph. With this arrangement a high uniform field was produced, and it was still possible to slide the

Figure 9.

The spectrograph in place between the cones.
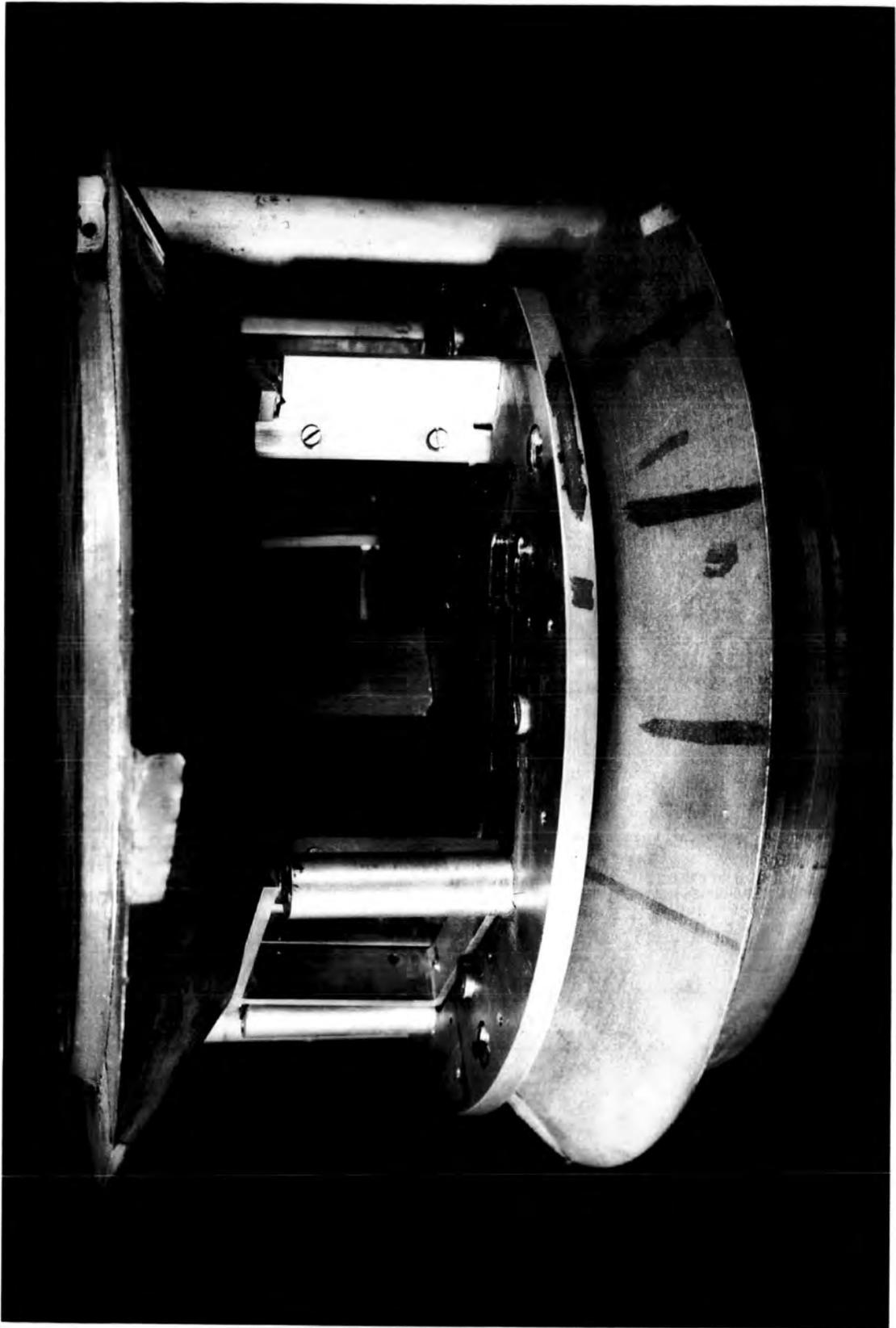
spectrograph in and out easily in order to replace target and frames.

The base of the spectrograph was so shaped that it could be slid easily into position between the spacers, and returned to its former position (see Fig. 10).

2.5. The Spectrograph as adapted to Experimental Conditions.

<u>Experimental Adaption</u>. It was decided to make two exposures with different targets. For one target carbon was chosen, as work with proton beams had previously stressed the need to examine closed shell nuclei (see 1.3), and many experiments had been carried out using a carbon target. The other target was to be silver, an important constituent of photographic emulsion and a heavier nucleus than carbon.

The original spectrograph (as described in 2.3) consisted of two semi-circles of three frames each; six frames in all. Each frame subtended an angle of 40° at the target, and allowing for track curvature, all angles of emission except those in the extreme forward and backward directions were covered. The exit and entrance were 2.4 cm. The magnetic field applied, caused the beam

Figure 10.

Insertion of the spectrograph between the cones.
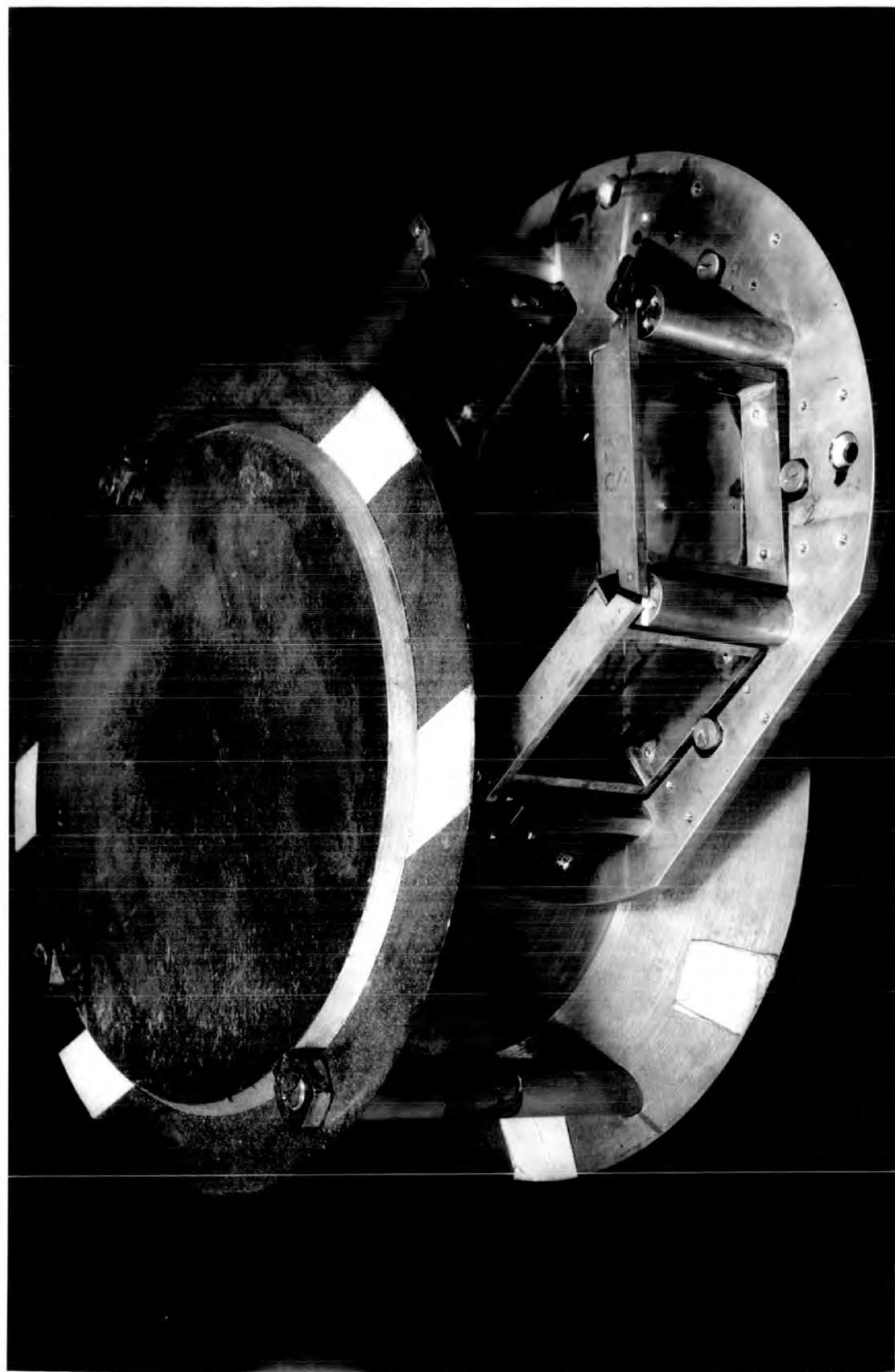
to deflect by 5 mm within the spectrograph before
reaching the target.   In order to focus the most intense
section of the beam on the target, the target was moved
5 mm from its central position.   This was necessary
since the calculated number of secondaries observable
depended on the centre of the beam passing into the
target and being scattered.   The repositioning did not
alter the essential measurements to be made for each
track, since the system could easily be recalibrated, and
after the exposures had been made, the recalibration was
performed for each of the frames, with the target in the
new position.

The second modification which was made, was more
important.   Due to difficulties in focussing the beam
(see chapter 3), its final profile laterally extended
beyond the spectrograph aperture, so that a portion of
low, but by no means negligible intensity passed through
the pillars and plates on either side of the entrance and
exit.   This meant that two plates at least would have
too high a background to be of any use, for not only would
there be tracks directly made by the beam, but also
scattering and interactions in the pillars would fill the

two nearest plates with tracks and increase the background
in the others.   Lead shielding and collimators did not
remove this tail on the profile.   It was decided
therefore, to remove two of the frames, so that the
spectrograph entrance and exit for the beam were increased,
and the chance of scattering in the supports was
considerably reduced.   The frames removed were those in
positions 6 and 3 in Figure 4.   The whole system was
then rotated until the beam was once more incident
perpendicularly on the target.

The removal of these frames meant that a much
smaller range of emission angles was covered, and also
that the detected particles were all scattered
approximately perpendicularly to the incident beam.
Unfortunately this is the least sensitive region in all
the nuclear models for which computations had been
performed.   The forward direction is the most sensitive
region, and the region in which the greatest discrepancy
had been observed so far in all experiments.   The
cross-section for scattering around 90° is almost constant,
but the shape of the energy spectrum in this region

differentiates between the various models. Probably the most sensitive variable in this region is the average energy of the particles scattered into each angular interval. However, it was necessary to alter the spectrograph to make the exposures in the time available.

These modifications did not in any way alter the essential accuracy of the spectrograph. In the angular region covered it was still possible to calculate both p and $\mathcal{E}$ from simple recordings of the tracks co-ordinates relative to the grid. A dummy run without any target would be made to record the background. This run would also reveal, if the beam at any time passed through any of the remaining plates.

The spectrograph as used with four frames in position and a carbon target can be seen in the photograph Figure 11. The glasses without emulsion are affixed to the frames, but the frames are unclamped. The shaping of the base which locates it between the magnet spacers is shown. The beam enters from the right, and was deflected by the field towards the top of the photograph and back again, on traversing the spectrograph.

Figure 11.

The spectrograph.
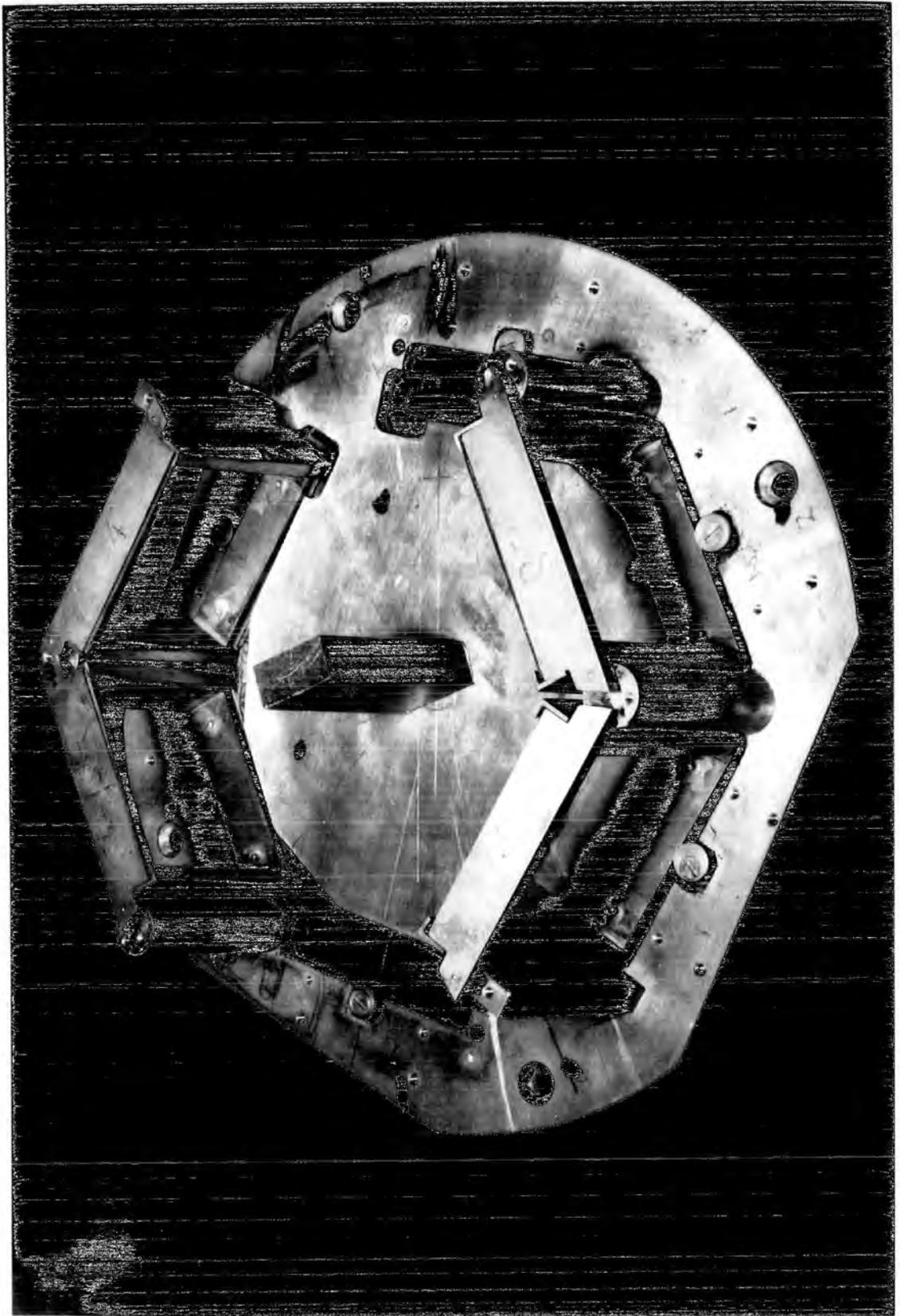
<u>Correction Factors</u>. It was necessary to adjust all computed values for two factors which affected the experimental data. The first was for the solid angle subtended by the plate at the centre of the target. Using diagram 3b the solid angle can be calculated. The horizontal path length for a particle is the arc of the circle cut-off by the chord ρ , $2\phi R$. In three dimensions the path length is -

$$\frac{2\phi R}{\cos\varepsilon'} = \frac{\rho\phi}{\sin\phi} . \frac{1}{\cos\varepsilon'} \qquad 2.6.1$$

The angle the beam makes with the perpendicular to the plate is α and -

$$\cos\alpha = \cos\theta . \cos\varepsilon' \qquad 2.6.2$$

also $\qquad\qquad \rho = d/\cos(\phi - \theta)$

let $\qquad\qquad \psi = \phi - \theta$

The solid angle per unit area is dw, where

$$dw = \frac{\cos\alpha}{(\text{path length})^2} \qquad 2.6.3$$

Thus from 2.6.1, 2.6.2 and 2.6.3

$$dw = \frac{\cos(\emptyset - \psi).\cos^2\psi.\sin^2\emptyset.\cos^3\mathcal{E}'.}{\emptyset^2.d^2} \qquad 2.6.4$$

so that for a particular $\mathcal{E}$ and p, ρ and $\emptyset$ are found for each $\mathcal{E}$, and dw can be calculated, using the relation -

$$\sin(2\emptyset -(A - \mathcal{E})) = \frac{300Hd}{p} - \sin(A - \mathcal{E}) \quad 2.6.5$$

and 2.6.4. This solid angle varied only slightly over the area scanned; the maximum variation being 6% for particles all travelling in the same plane, and 20% for all particles travelling from the target to any one plate.

The second factor was due to the selective detection at the edges of the plates. Particles emitted at the same spatial angle can have different projected horizontal angles of emission, and hence one may be detected while another misses the edge of the plate (see Fig. 6). Also it is the projection horizontally which determines the radius of curvature of the track. Hence at the plate end A for particles emitted with a vertical component of momentum more low energy particles will be lost than high energy ones. Similarly at the end B more high energy

particles will be lost. As considered here this effect is due to the finite size of the detecting area, the plates, and the curvature variation with momentum, and is independent of the target size. The effect of the target size was considered separately. The method of analysis described in chapter 4 took into account the loss due to the finite detector and shape.

Accuracy. The grid was calibrated to within 1 micron. The accuracy of location of the frames (see 2.2) was such, that with the frames in position the grid line was horizontal to within 10μ, the actual slope being known for each frame. This meant that the induced error in p and $\mathcal{E}$ was negligible.

The plates were vertical to within 3μ, and have only been scanned across the central region, thus no corrections have been introduced to compensate for this very slight inclination with respect to the vertical.

Effect of the target. The chance of an incident pion making two collisions in the target is $1/400$. Scattering in the target gives rise to an error in $\mathcal{E}$ of less than $5°$, and only below 160 MeV/c does it have an

appreciable effect on the momentum. For a particle of 120 MeV/c passing through 1 cm of target, the expected decrease in momentum is 10 MeV/c for carbon, and 19 MeV/c for silver. Therefore at a momentum as low as 120 MeV/c the error is 16%, and above 200 MeV/c it is negligible. The target size introduces errors in p and $\mathcal{E}$ which are considered further in chapter 4.

Effect of field. The high magnetic field causes low momentum particles to spiral, so that they never reach the frames. With 25 kg the lowest momentum which could be detected is about 50 MeV/c, which would give a very black track for a pion with θ equal to about 180°. In addition the target size would effectively prevent the detection of any particles below 80 MeV/c for carbon, and below 90 MeV/c for silver, due to absorption of secondaries within the target.

The effect of these errors is summed in Table 13 (see chapter 4) for plate 5, as an example of the variation in expected error in any one plate.

3. THE EXPERIMENTAL RUN.

3.1. Production of Pion Beam.

The beam used was produced from an internal target
in the 600MeV C.E.R.N. synchrocyclotron. A similar beam
had already been produced once, so the essential details
of the transport system were already known. The
requirement was a negative pion beam of about 300MeV with
as high an intensity as could be achieved. It was
necessary before the exposure to measure both the energy
and the contamination of this beam, and to focus it onto
the target. The actual floor space available for setting
up the transport system was limited by the need to avoid
the muon channel on one side, and the neutron beam on the
other (see Fig. 12). In fact the geography of the
neutron room where the exposures were made, determined
the location of the target relative to the channel
through the synchrocyclotron shielding wall.

It was hoped to finally produce a beam which in a
reasonable exposure time would provide one track per field
of view when scanning the plates. This meant in fact
about 5×10^3 secondaries per cm^2. For this was required
a beam of intensity 4×10^4 particles per second, which
could be focussed sharply on to an area of 2×5 cm^2.
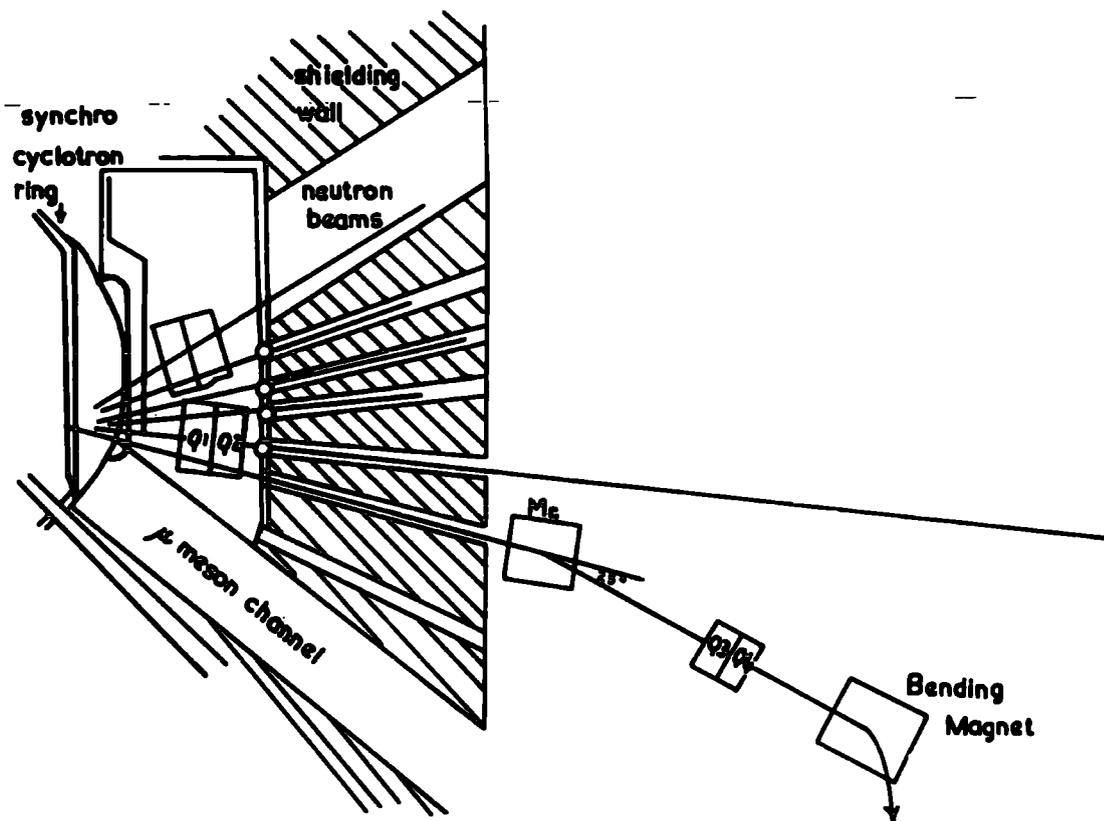
Diagram of Neutron Room

showing experimental layout

Figure 12

The exposure time would then be about eight hours.
(see 2.1).

3.2   Beam Transport System.

The beam transport system consisted of the fringing
field of the synchrocyclotron, and then a pair of
quadrupole magnets, placed as near to the target as
possible in order to obtain a high beam intensity.
These magnets are marked Q1, Q2, in Figure 12.   Outside
the shielding wall was an analysing magnet, MC, and a
further two quadrupoles, Q3, Q4, which independently
focus the beam horizontally and vertically.   The final
component of the system was the magnet into which the
spectrograph was to be inserted, hereafter referred to as
the 'bending magnet'.

The magnet used for the bending magnet was a
C.E.R.N. one metre bending magnet with tapered poles,
which would produce a maximum field of 17.5 kilogauss
(see CPS User's Handbook 02, page 2).   With the cones in
position near the front (with reference to the beam
source) of the magnet, the magnetic field strength was
measured using both a fluxmeter and a gaussmeter.   The

two instruments gave equal readings within the
experimental errors for the field strength, which was
25.5 kilogauss between the cones during the exposure.
In order to be able to define the trajectory of the beam
between the point of entry into the magnetic field and
the target, it was necessary to plot the field strength
over the area of the bending magnet.   A typical plot of
the field variation is shown in Figure 13.

In order to define the trajectory in the exposure
area, use was made of the floating wire technique (see
Braunersreuther, 1961).   A wire carrying an electric
current, had one end fixed on the axis of the beam between
the analysing magnet and the second pair of quadrupoles.
This wire passed through the quadrupoles and through the
bending magnet between the cones, and was held taut on
the far side.   The correct deflection for a given beam
momentum should be obtained by passing the appropriate
current through the wire.   The wire itself, must not
pass through two focal points, since all trajectories will
go through these two points and the wire therefore becomes
unstable.   The field strength changed so rapidly over
the cones that the wire merely averaged the effect, and

Magnetic Field Strength Variation across magnet
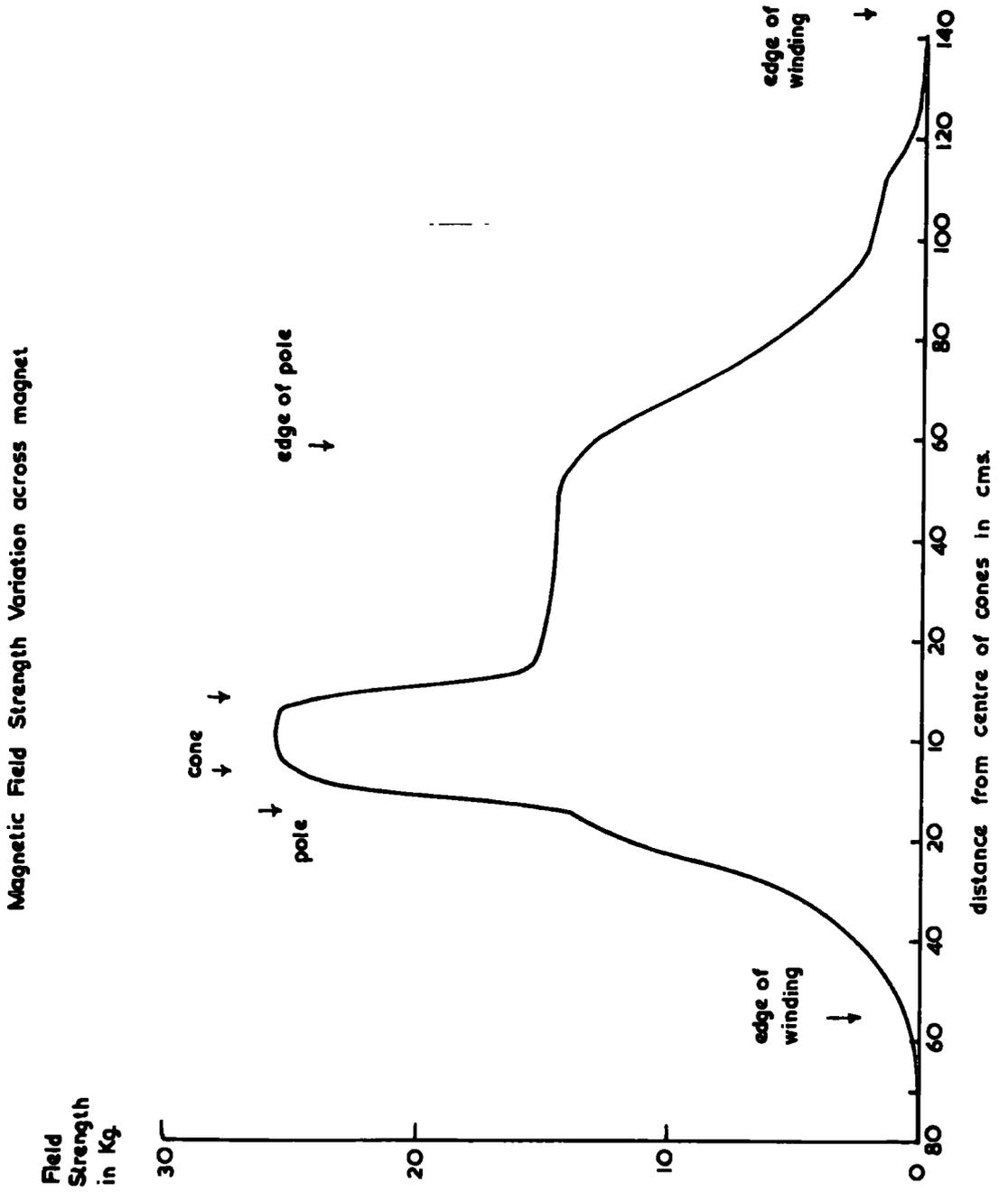
Figure 13

only a rough estimate of the deflection and hence the trajectory could be estimated. However, the wire indicated that the unscattered beam would pass out through the side of the magnet, no matter which position the cones were placed in relative to the geometry of the bending magnet.

The Profile. The profile of the beam was examined with the aid of a beam scanner consisting of scintillation counters. The intensity of the beam was first optimised by varying the currents in the quadrupoles and the analysing magnet. Three counters were used. Counter 2, the monitor, was between the channel through the shielding wall and the quadrupoles Q3, Q4. Counters 3 and 4 were placed on a scanning table, beyond these quadrupoles, one directly behind the other. The table provides the means for these two counters to be moved by remote control vertically and horizontally, accurately and together, through the beam.

For optimisation the currents in each component were varied individually keeping everything else constant. When altering the currents in a pair of quadrupoles, one current was increased, as the other was decreased, and then the polarity of each was reversed. As each

quadrupole tends to focus the beam in one plane and defocus it in the perpendicular plane, this selected the best combination for focussing the beam at one unique point in both planes. The beam profile was almost guassian, both horizontally and vertically. The peak of the intensity curve at the focal point, about one metre from Q4, was made as sharp as possible by altering the magnet currents, but there was still a long, low intensity tail.

A collimator was erected beyond the second pair of quadrupoles Q3, Q4. This reduced the peak of the intensity distribution rather than the tail. The intensity was measured at the image and at various distances from it. Finally a long collimator was built with an exit pupil $1 \times 4cm^2$, which gave a half width for the distribution of 1cm. This still left the beam too diffuse to reach the target without the tail passing through the side of the front frames. Two of the frames, those in positions 3 and 6, were removed in order to widen the entrance and exit, and the cones were rotated slightly. The final profile is shown in Figure 14.

a) Horizontal Beam Profile   collimator exit pupil $1 \times 4 \, cm^2$
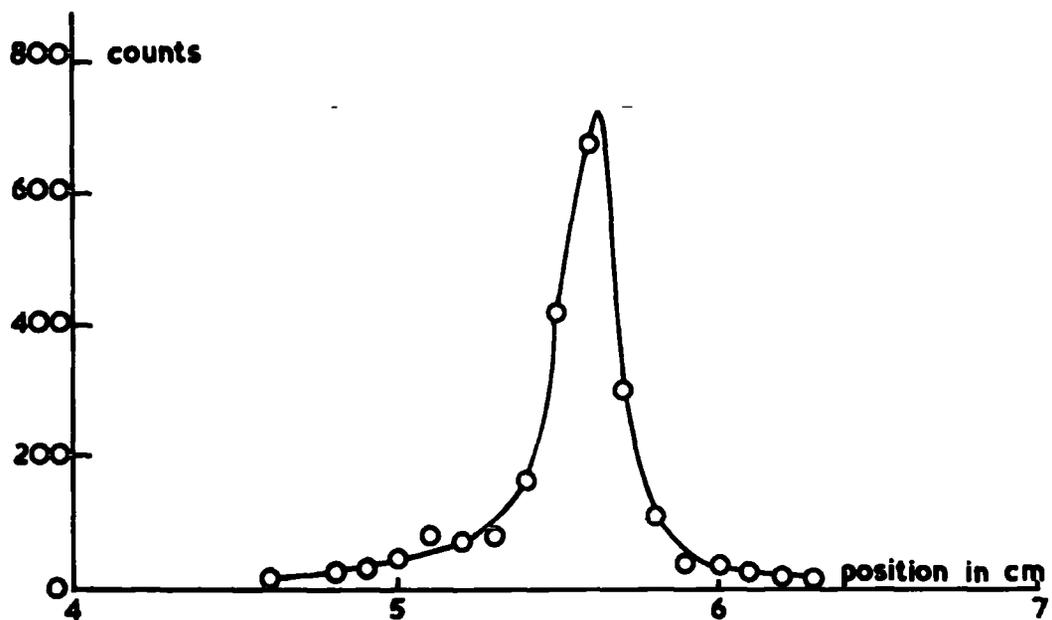
b) Vertical beam profile
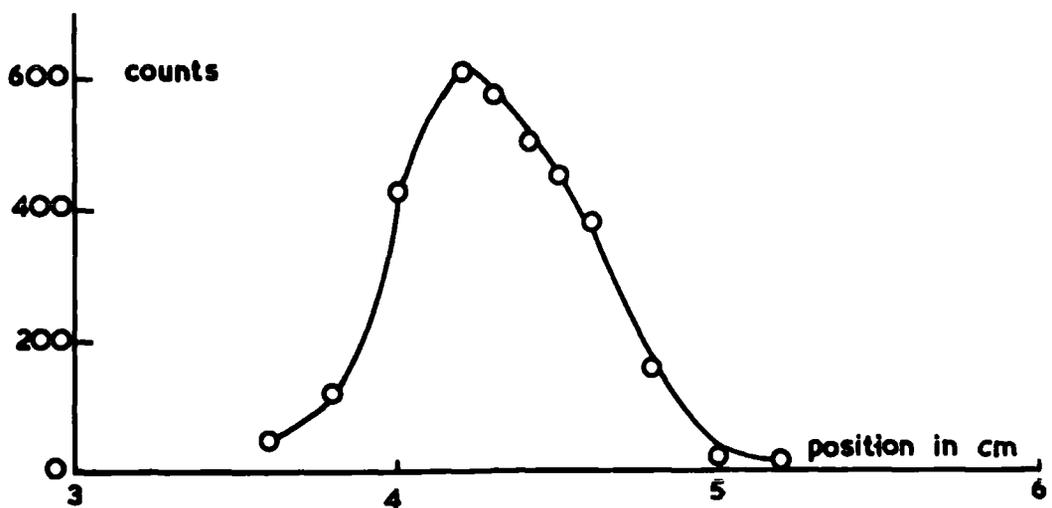
Figure   14

In order to find the correct position for the target inside the bending magnet, use was made of a scintillation counter with a long light guide. The counter could be placed between the cones, and the system adjusted so that the target was in the optimum position.

The beam intensity was also monitored using a scintillation intensifying polaroid camera made by one of the C.E.R.N. staff. (M. Roberts, private communication). This produced photographs of the beam intensity distribution, but the pion flux was so low that a long exposure was needed.

With the scintillation counter in the target position, the cones were moved across the magnet face until the counter was in the beam. The final adjustment was then made by varying the magnet current until the beam centre impinged perpendicularly on the counter. Once the cones were in their final position, this position was marked on the lower magnet face and the cones were not moved throughout the exposures. The spectrograph was inserted and removed without upsetting this arrangement. The magnetic field used for the exposures was 25.5 kilogauss.

3.3. Contamination and Radioactive Background.

Contamination.   An attempt was made to measure the
contamination of the beam using a time of flight technique.
(Dick, private communication).   Two scintillators are
used, both placed in the beam, but a distance, L, apart.
The final output of the equipment has a series of peaks,
one for each type of particle present in the beam.   The
separation between two of these final peaks is given by:-

$$\Delta T = L(1/\beta_1 - 1/\beta_2)/c$$

where ΔT is the time interval between the peaks, and β_1
and β_2 are the momentum-energy ratios for the two different
particles.

The distance L was 10.53 metres.   The resolution
of the peaks was not accurate enough with the counter
separation available, so that all that could be concluded
was, that there was a low muon but possibly high electron
contamination.   A typical curve obtained by this method
is shown in Figure 15.   By observing the shift of the
peak when a known delay was applied between the counters,
the distance between the channels could be calibrated in
terms of the time interval ΔT.
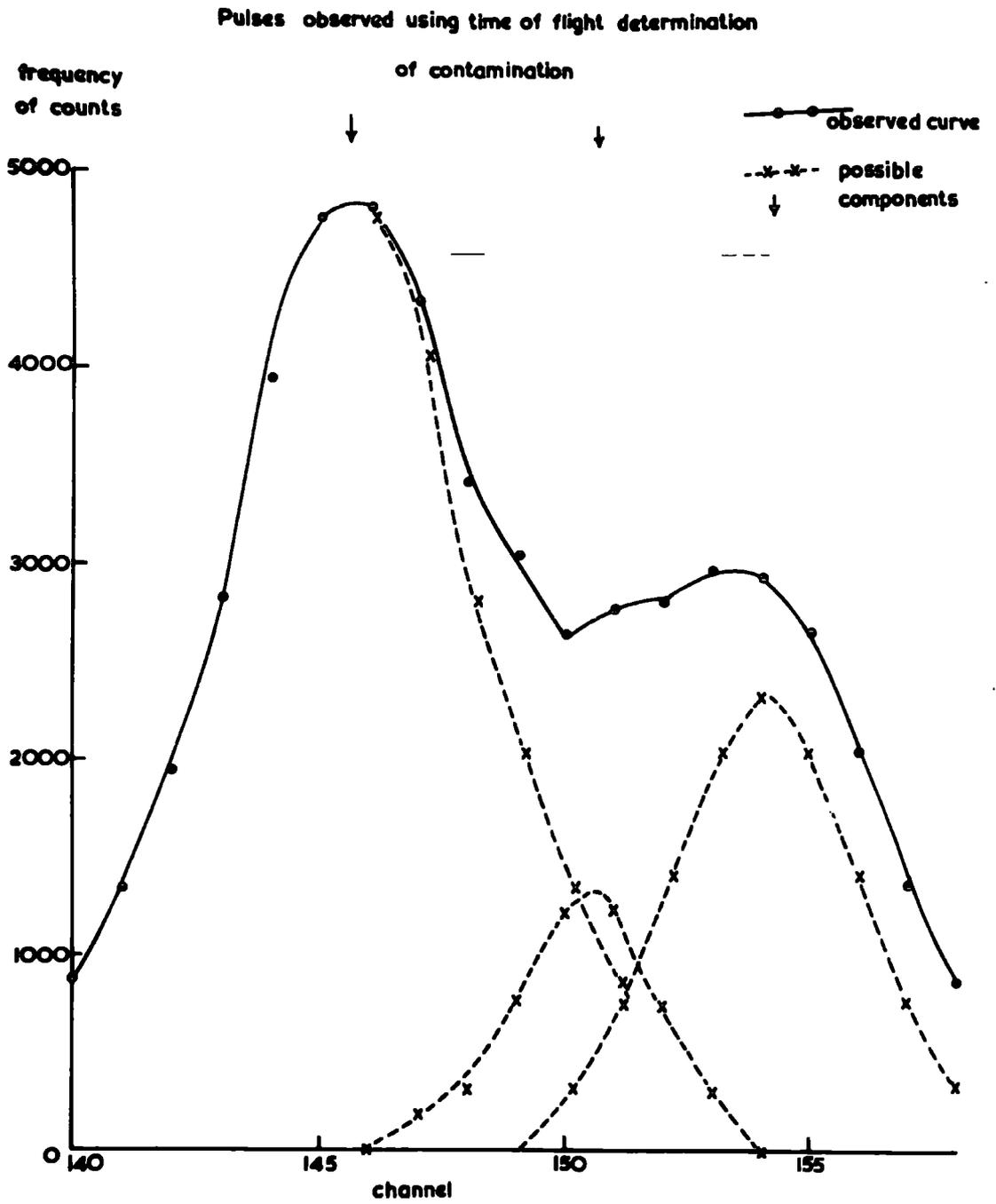
Figure 15

The muon contamination was examined by exposing some plates for ten seconds directly to the incident beam. The plates were then rotated through 90° and exposed for one minute to the beam, after the beam had passed through 15 cm of copper. The collimator used during the exposures was in position and the stack was exposed beyond it. The range of the particles in these plates was examined and the appropriate particle masses determined. This method showed the muon contamination to be 10%.

Background. In order to reduce the background a lead wall was erected in front of the cones, with a suitable beam aperture. This would shield the plates from background originating outside the magnet, but could not reduce any background arising after the beam had entered the spectrograph. Since as already mentioned in 3.2, the beam passed out through the side of the magnet some background was inevitable. The dummy run would provide the necessary data for the subtraction of the background from the signal.

Finally the best possible arrangement in the time available was achieved.

3.4. Exposures Made.

Three four hour exposures were completed with the spectrograph and with plates in positions 1, 2, 4 and 5; (see Fig. 4) for one a silver target was used, for one a carbon target, and one was without a target. For each exposure four fresh plates were used.

Because of the high background and the broad profile of the beam, it was decided to make an alternative exposure with no magnetic field. The simplest arrangement was used, employing large solid angles, and is shown in Figure 16. Rejecting the use of a magnetic field meant that multiple scattering measurements would have to be made in order to obtain the secondary pion energies, and therefore the layout was designed with this in mind. Since the technique used is not uncommon in nuclear physics and cosmic ray work, this will be referred to as the 'conventional' exposure.

The use of iron shielding successfully limited the extent of the beam in the vertical plane, so that it was incident on a 10cm long carbon target, but not on the stack of nuclear emulsion pellicles. In the horizontal
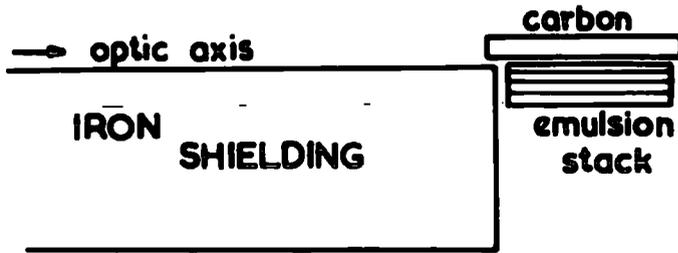
a) Arrangement for exposure
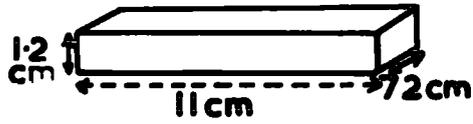
dimensions
of carbon block
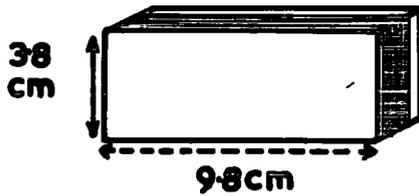
emulsion stack

Figure 16

plane the beam profile was satisfactory. The stack
consisted of 25, 400μ thick pellicles, lying between two
thick pieces of perspex, and the whole covered with black
paper to shield the emulsion from the light. This stack
was supported at a distance of 1cm from the carbon, so
that low energy particles would not reach it. The
exposure lasted three hours. Secondaries emitted between
6° and 174° could be recorded in the stack, but the
angular interval between 35° and 145° is the most
completely covered.

The disadvantages incurred by this design were
those which had led in the first place to the design of
the spectrograph. Aligning the plate for each angle of
emission, finding and measuring the tracks was a slow and
tedious process. Also, though for most tracks the pion
mass could be fairly confidently assumed there was no
way of determining the charge of the particle.

Momentum Determination. The exposure already
mentioned in 3.3. would enable the momentum of the beam
to be determined within the accuracy needed. The
particles which had passed through 15cm of copper would

have lost on average all but a few MeV of their initial
energy.   Therefore the particles will come to rest in
the emulsion and from the length of the track in the
emulsion the initial energy of the particle can be
estimated.   The tracks running perpendicular to these
stopping particles were of unscattered particles from the
main beam, and on these tracks pβ measurements could be
made.   Thus two methods were available for determining
the momentum of the beam, and the values obtained could
be compared.

3.5.   Processing.

Development of all the emulsions was by a
temperature cycle method.   The plates were presoaked and
cold developed at 6°C, and then placed in a dry hot stage
at 23°C.   The duration of each stage depended on the
emulsion thickness.   This system produced even
development throughout the emulsion with a clear image.

Before development the emulsions from both the
conventional exposure and the momentum-contamination
exposure were gridded on one surface, and numbered and

labelled on the other surface using a soft pencil.   The pencil mark would show after processing since all pressure marks cause local development.   The emulsion gridded side down and then affixed to a glass plate which had been specially coated by Messrs Ilford Ltd.

The spectrograph plates were removed from the frames before processing.   Since these plates were so small a special developing tank was constructed.   The plates, approximately 5.4 x 5cm^2, were held in a perspex rack.   As there was emulsion on both sides of the glass, the rack was necessary to prevent the sodden emulsion being damaged by handling during the processing.   This rack fitted comfortably into the developing tank which could then be supported in a tank of water at a suitable temperature.   Before removing from the frame, each plate was marked on the surface nearest the target so that both its position on the circle, and the type of target, if any, were recorded.   The spectrograph plates were processed immediately after exposure.

4. SCANNING AND MEASURING THE PLATES AND REDUCTION OF DATA

In chapter 3 three kinds of exposure have been described. Firstly exposures to determine the mean momentum of the beam were made. Secondly there were exposures using the emulsion spectrograph, and thirdly exposures to determine the scattering in carbon using emulsion in a conventional way. In this chapter the evaluation of the momentum of the beam based on scattering measurements and range-scattering measurements is described. This is followed by an account of the scanning and analysis of the plates and the results of the spectrographic exposures. The results from these exposures are compared with those from the conventional emulsion stack exposure.

4.1. Determination of the Energy of the Beam.

The experimental arrangement and exposures for determining the incident beam energy have already been described in 3.3. It was arranged that the kinetic energy would be in the region of 300 MeV (see 1.7), and the apparatus was designed with this energy in mind. In order to be able to estimate the energy loss of the

scattered pions, it was necessary to know as accurately as possible the average energy of the incident particles, and their energy distribution. Without these values the determination of the number of low energy transfers which take place would not be possible. Two methods were used to measure the beam energy.

a) <u>Absorption of the beam</u>. The stack which had been exposed behind the copper absorber was scanned as follows. Tracks, which from their inclination and position must have passed through the copper were picked up 1 centimetre from the edge of the plate. Each track was aligned parallel to the motion of the microscope stage, and its length and angle of inclination recorded. Using a cell length of 200μ, the scattering of the track was measured, moving away from the plate edge, and hence $p\beta$ for each track was determined. About 50 readings were made for each track.

Nineteen tracks were measured thus, and three of these were rejected after measurement since their $p\beta$ were too high for them to belong to a 300 MeV π^- beam, but were consistent with them being muons. For the remaining sixteen tracks, the average $p\beta$ was (122 ± 3) MeV/c with

a standard deviation of 15 MeV, corresponding to a
kinetic energy of 62 MeV after 15 cm of copper.   The
range-energy determinations of Barkas (1958) were used in
conjunction with the data of Sternheimer (1959) to
evaluate the initial energy incident on the copper.   From
the measurement of pβ the energy and therefore the
residual range of the particle leaving the copper can be
deduced.   This residual range added to the equivalent
path in emulsion for 15 cm of copper gives the total range
and hence the energy.

The incident kinetic energy was calculated by the
above method to be (285 $\pm$ 2) MeV.

b) <u>Measurements on the incident beam</u>.   Scattering
measurements for determining pβ were made as follows.
Beam tracks were picked up 1 cm from the plate edge,
aligned parallel to the traverse of the stage, and the
scattering recorded on cell lengths of 200 or 300μ.
Over 40 readings were made on each track, so that pβ was
determined to 10% accuracy.

31 tracks had an average pβ of (376 $\pm$ 12) MeV/c,
which is equivalent to a kinetic energy of (285 $\pm$ 15) MeV.

c)   <u>Final estimate of energy</u>.   Good agreement for the energy of the incident meson beam was obtained using the two methods described above.   The value used in all subsequent calculations for the incident kinetic energy was (285 ± 15) MeV, equivalent to a total energy of 421 MeV and a momentum of 400 MeV/c.

4.2.   Scanning of the Plates from the Spectrograph Exposure.

a)   <u>Details of the method</u>.   The plates were examined on Cooke microscopes under a magnification of 45 x 1.5 x 15.

The upper emulsion surface, that which had been nearer the target during the exposure, was area scanned. Suitable tracks were picked up and followed to the emulsion-glass interface, and were paired in the other emulsion, matching similar lengths and the same apparent directions at the emulsion-air interface;   the direction at this surface is not affected by distortion because the emulsion can move freely here (Fig. 17a).   The co-ordinates (X, Y) of the track at the two emulsion-glass interfaces were recorded, and at the beginning of each days scanning
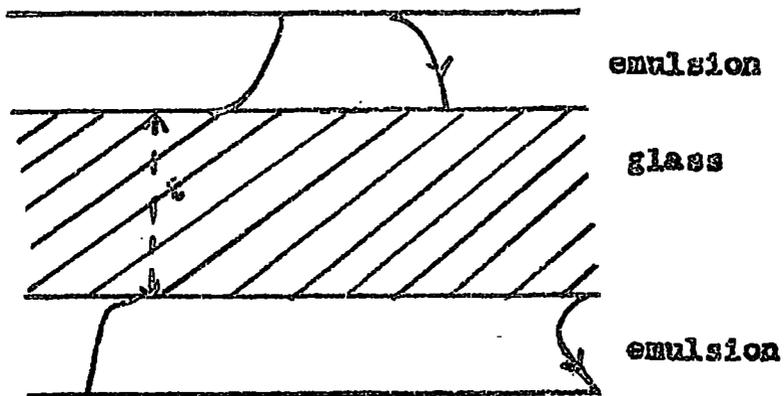
a). Track directions in emulsions and glass.
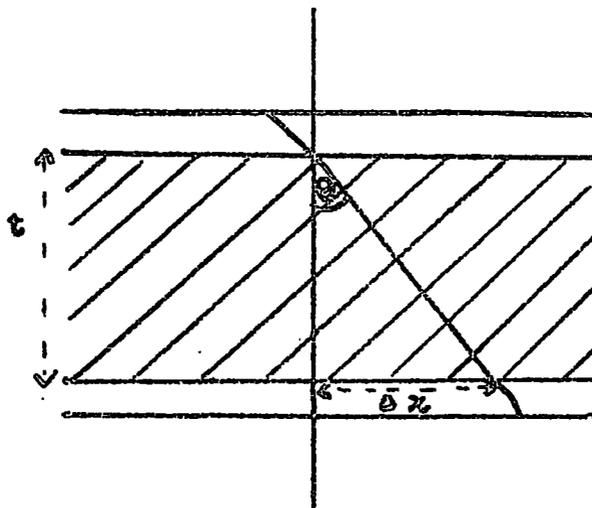
b). Determination of Θ.

Figure 17.

the co-ordinates of the central crossing-point of the
grid-lines on the glass were also recorded all to an
accuracy of $\pm 2\mu$.

Equal areas either side of the central grid line
were scanned, each scan starting and finishing at least
$\frac{1}{2}$ cm from the edge of the emulsion thus eliminating edge
distortion.   The scanning was started above the horizontal
cross grid line, and that section of the plate which had
been the upper area vertically during the exposure was
scanned.

To eliminate obvious low energy and background
particles, tracks whose length was greater than 250μ in
the upper emulsion were rejected.   Even if a particle
were emitted from the extremes of the target, its track
length should be less than 250μ in the upper emulsion,
and most low energy secondaries will have been absorbed
by the target (i.e. those with momentum $\lesssim$ 80 MeV/c, see
2.5).   Thus any long tracks should be background or
secondary scatters.

b)   <u>Collection of data</u>.

<u>Horizontal component</u>.   From the co-ordinates of

the track at the emulsion-glass interfaces, the horizontal
component of the track length, Δx, in the glass was
obtained by subtraction (see 17b).   Now

$$\tan\Theta = \Delta x/t. \qquad\qquad 4.2.1$$

where t is the glass thickness (see 2.2).   At low Θ
therefore there is an almost linear relationship between
Θ and Δx.   From this stage, in all subsequent work,
only tracks for which a partner had been found in the
lower emulsion are considered.   On a piece of graph
paper, with X in the upper emulsion and Δx as
co-ordinates, the positions of all such tracks were
recorded. Δx runs from -250μ to $+250\mu$, the corresponding
value of Θ depending on t.   X depends on the area
scanned but was in the range 0 to 25 mm in all cases.
On the X scale was recorded the average position of the
fixed point, the central crossing point (C in Fig. 5b)
of the grid lines.

   Vertical components.   The vertical distribution of
the tracks was examined, where

$$\tan \mathcal{E}' = \Delta y/t. \qquad\qquad 4.2.2.$$

In figure 18 the vertical distribution of emission points in the target as recorded in C5 is compared with the vertical beam profile (Figure 14). Allowing for the distortion of the distribution due to emission angle, and emission points off centre in the target, it can be seen that particles detected in the central region of the plate were detected predominately in the same horizontal plane.

The maximum vertical angle of emission to reach the centre of the plate is 27°. For this angle the horizontal component of the momentum will be at its minimum value of 90% of the total momentum. This will tend to shift the highest momenta down by 40 MeV/c, but at 200 MeV/c the error is only 20 MeV/c. From figure 18 it can be seen that 82% of the particles have a horizontal component of more than 99% of their total momentum. Therefore, as assumed in chapter 2, the curvature of the track will give an accurate estimate of the momentum.

4.3.   Method of Analysis

a) **Reason for this method.** Already in chapter 2 (see 2.2. and figure 6) the effect of the target has been

Number
of tracks
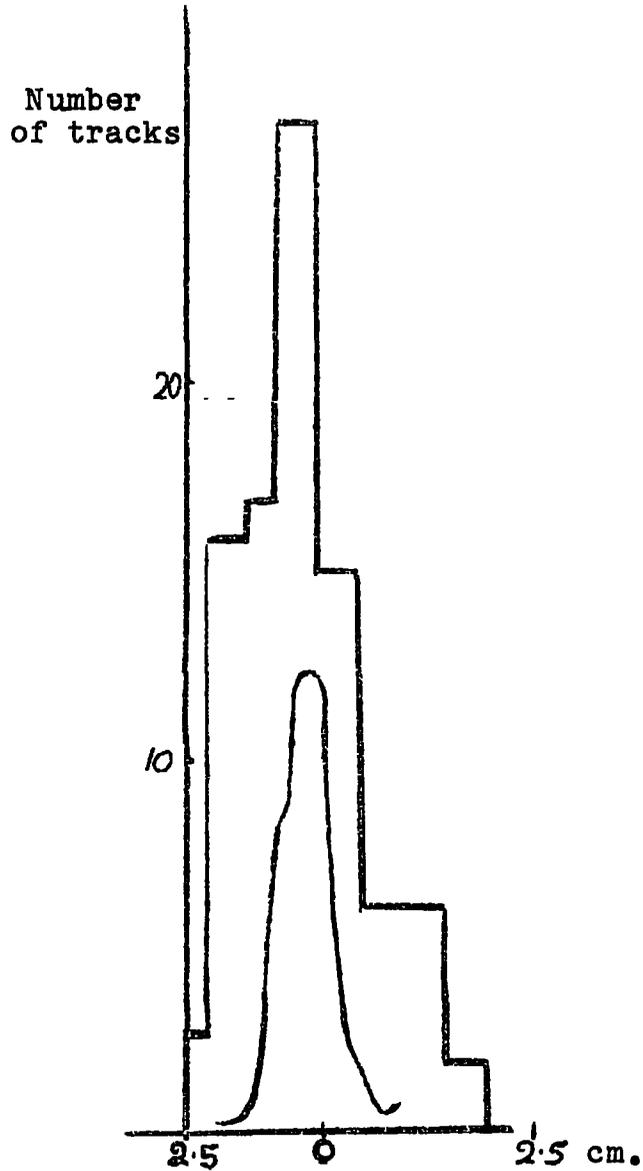
Vertical distribution of emission points in target
for particles dectected in C5.The distribution in C4
was very similar.
The vertical intensity variation of the beam(see
figure I4) is shown with the same horizontal scale.

Figure I8.

mentioned.   If all the particles come from a point
target, the charge on the particle would be easily
determined from the curvature of the track, but the extent
of the target in the horizontal plane alters both the
apparent charge (see Fig. 19a) and the apparent momentum
(see Figs. 6a and 19).   Consider the tracks in figure 19b,
OF is a straight line from O to the plate, and in fact
represents infinite momentum of either charge at a given
emission angle.   P is the track of a negative particle
emitted from O with 400 MeV/c.   Many particles from the
target of high momentum which strike the plate between P
and F will leave a track of little or no apparent
curvature with respect to O.   The particle therefore
will appear negative and of even higher energy, the nearer
to F the higher the energy.   This is so only for tracks
which appear to have very little curvature with respect
to O.   Track A, the same curvature as P and therefore
actually with the same momentum, when traced back to O,
appears as a very high energy positive particle.
Similarly track B, also the same curvature as P, appears
as a negative particle of much lower energy, if O is the
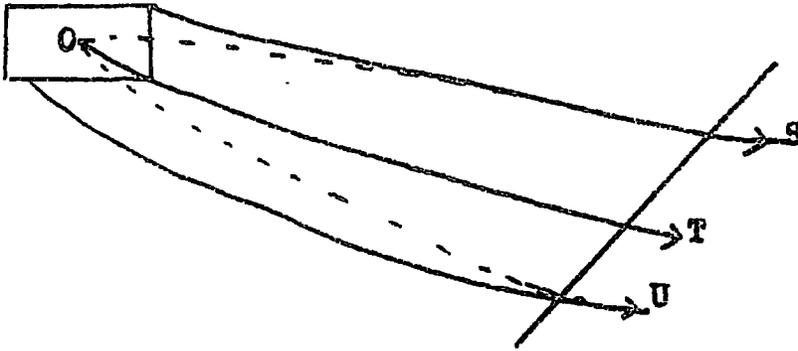
a) If O is taken as the point of origin then S and U which
   are negative and of the same momentum, appear to have
   different track curvatures, and S in fact appears to
   carry a positive charge.
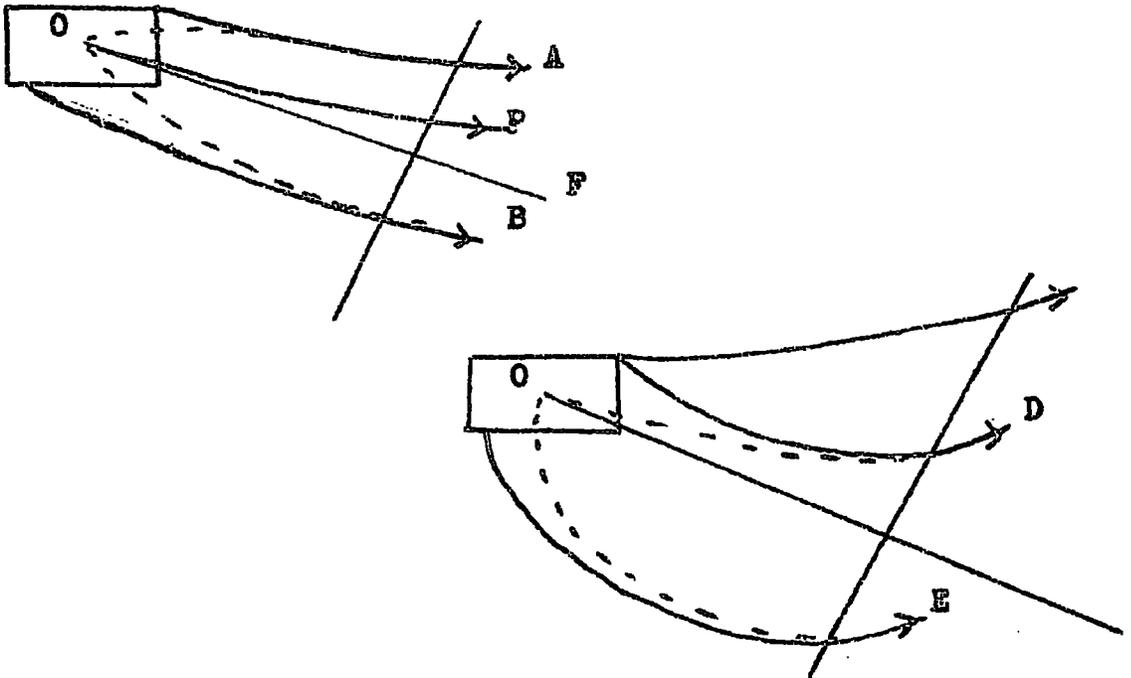
b) Alteration of track charge and momentum.
   P is a negative particle emitted from O with about
   400 MeV/c.

Figure 19.

assumed emission point.   Thus tracks of 400 MeV/c negative

pions emitted uniformly from all points in a horizontal

cross-section of the target will appear with respect to

O as very low energy negative pions through the whole

range to infinitely high energy pions of either charge

and as high energy positive pions.

Similarly tracks D and E are of low energy negative

particles.   If traced back to O, D appears to be of much

high energy, and can even appear as of positive charge,

while E appears to be of much lower energy.

When a simple computer program was run using O as

the sole point of emission, as many positive as negative

particles were obtained with apparent momenta running all

the way up to infinite.   Therefore a new method of

analysis was used.

b) <u>The analysis</u>.   For a particular plate of thickness

t, the values of $\sin\theta$ and Δx were plotted (see equ.

4.2.1).   For this same plate the values of d (see 2.2)

and A (equ. 2.2.3) are calculated from the original

calibrations for each of the points B_0, O, and F_0 (see

Fig. 20a).   Selecting a particular point of emission,

values of x (Fig. 5a) (equivalent to different angles of
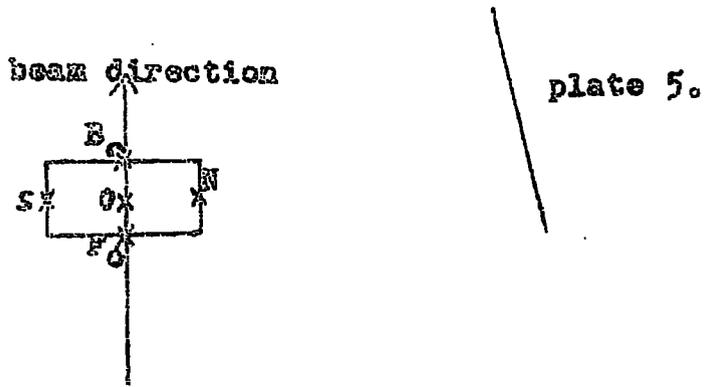
a) Path length and direction of beam in target.
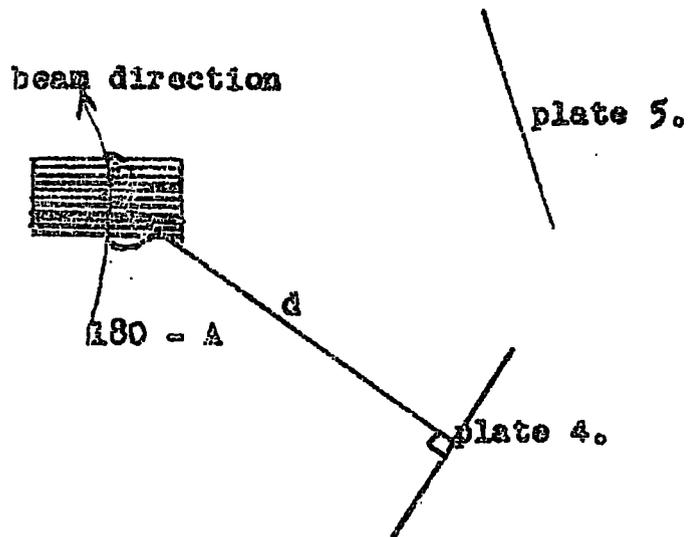
b) Division of target into equal segments.

Figure 20.

emission) from 0 to 2 cm are chosen, and values of $(\theta - \phi)$
(equ. 2.2.1) can then be obtained, also values for ρ for
each x (equ. 2.2.2). The steps are as follows. Once
x is chosen, then from equation 2.2.2, ρ is uniquely
determined. A value of p is now selected. From
equation 2.1.4, it can be seen that these values of ρ
and p fix ϕ. ϕ is then substituted in $\theta - \phi$ in equation
2.2.1 and θ is obtained. Using this value of θ, Δ x
can now be calculated (see 4.2.1). For each p therefore
we have x and Δ x. Five values of p, 100, 200, 300, 400
and 500 MeV/c, were used. So it is now possible for
each emission point, for example F_o, to choose a
particular momentum, and from the above calculation
determine the values of Δx and x which will be observed
for a particle emitted from F_o with this momentum.

On the X- Δx plot (see 4.2b) curves are drawn for
each momentum, showing where the tracks will occur for
target positions corresponding to B_o, 0 and F_o. For
any one target position, the momentum curves turn out to
be almost parallel and sensibly straight lines. The
diagram is then divided into equally spaced channels,

which are arbitrarily numbered. The channels run parallel to the lines of constant momentum. Figure 21 shows a typical plot without the points for the observed tracks. All plates which occupied the same position in the spectrograph, have the channels marked off in the same x- Δx positions. The relative values of x and X depend on the co-ordinates of C, and its distance from d (see 2.3). It can be seen in figure 21, that particles of different momentum can reach the same parts of a plate with identical inclinations provided they originate in different regions of the target. Moreover, any high momentum positive particles will fall into the channels expected for the high momentum negative particles.

If the initial momentum spectrum of the scattered particles is known, from the distribution of scattering points in the target the number of particles falling into each of these channels could in theory be calculated. In fact the number of target scattering points is uniform in depth $(F_0 \rightarrow 0 \rightarrow B_0)$ and proportional to the beam intensity $(S \rightarrow 0 \rightarrow N$, Fig. 19a). The number of tracks falling into some arbitrary channel A is N_A, where
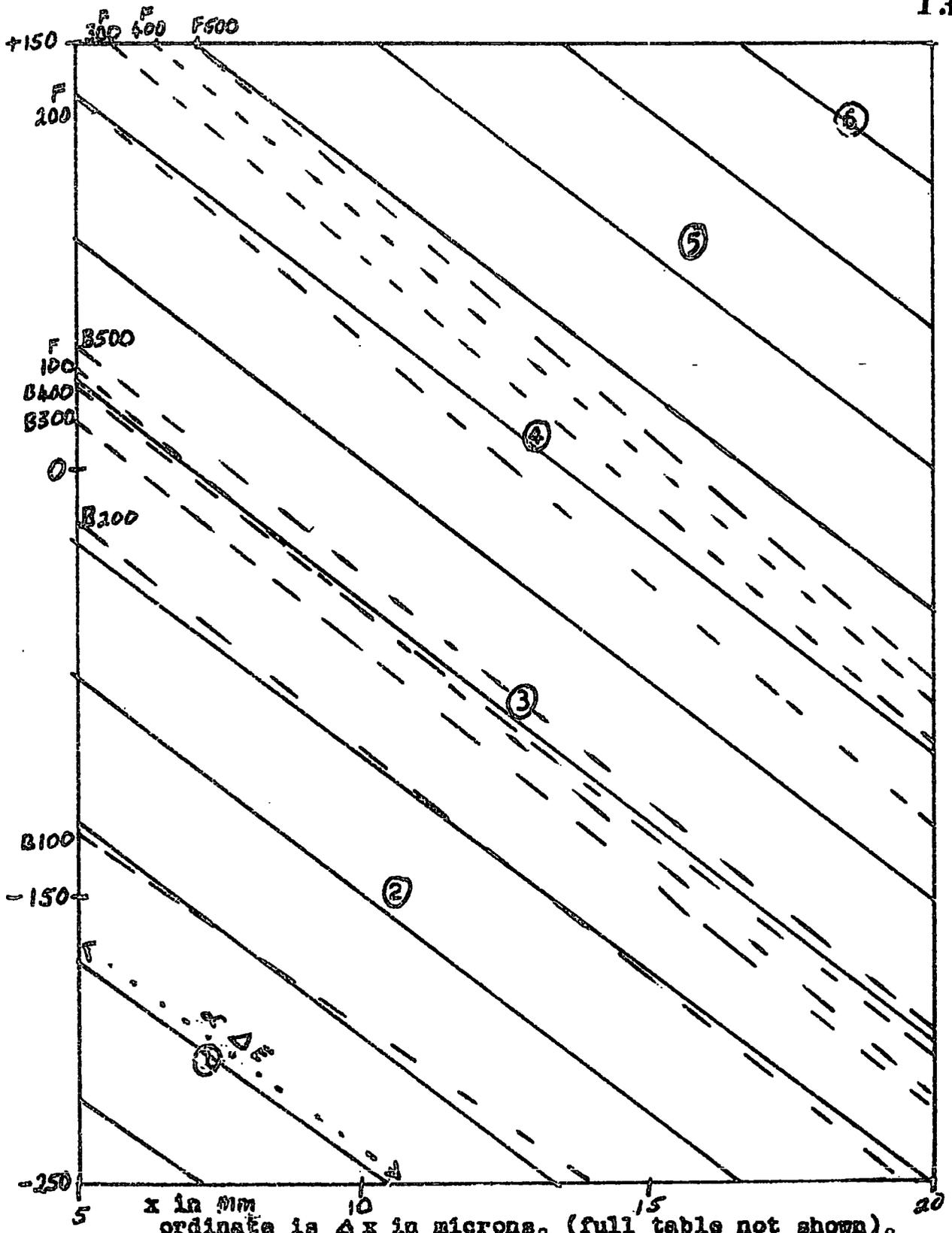
ordinate is Δx in microns. (full table not shown).
F and B refer to target positions, number is momentum
in MeV/c.

Figure 21.

$$N_A \propto \frac{d\sigma}{d\Omega} \cdot \Delta\varepsilon \cdot \left(n(p_o)\Delta p_o + n(p_{F_o})\Delta p_{F_o} + n(p_{B_o})\Delta p_{B_o} \right.$$

$$\left. + \text{ all intermediate positions} \right)$$

for $B_o \to 0 \to F_o$.

where $n(p_1)$ is the number emitted in momentum interval p at position 1.

Now $\Delta\varepsilon$, the angular width subtended by channel A at the target, is proportional to the length of the straight line on the graph (see Fig. 21), and is constant over a large area of the plot and $\frac{d\sigma}{d\Omega}$, the differential cross-section is approximately constant. Therefore the 'density' of tracks is

$$\frac{N_A}{\text{Length of A}} \propto \frac{N_A}{\Delta\varepsilon} \propto \sum_{i=F_o}^{B_o} n(p_1)\Delta p_1 \qquad 4.3.1.$$

i.e. the track density automatically eliminates the angular dependence and depends only on the momentum spectrum of the scattered particles.

The problem is to find $n(p)$ from the track density, for this a fixed Δp of 50 MeV/c is assumed. A matrix

is formed which gives the proportion of this Δp at a particular value of p which falls into channel A, channel B, etc. for particles scattered at a particular level in the target.

The target is divided into 10 0.1 cm strips parallel to the beam, as shown in figure 20b. For a target position in the centre of each strip, X and Δx for each p are determined. In practice it is possible to interpolate between positions, and calculations need not be made for every strip.

The channels into which the various momenta from each target position fall, are plotted as shown in figure 22. The matrix is assembled from this graph by tabulating as follows:-

Channel A contains - 110 - 140 MeV/c from B_o 60% of Δp = 50

Channel B contains - 140 - 160 MeV/c from B_o 40% of Δp = 50

and   100 - 120 MeV/c from C   40% of Δp = 50

etc.

The matrix is then modified to allow for emission points across the width of each strip $(S \rightarrow 0 \rightarrow N)$. The beam intensity however falls off rapidly, dropping to half-
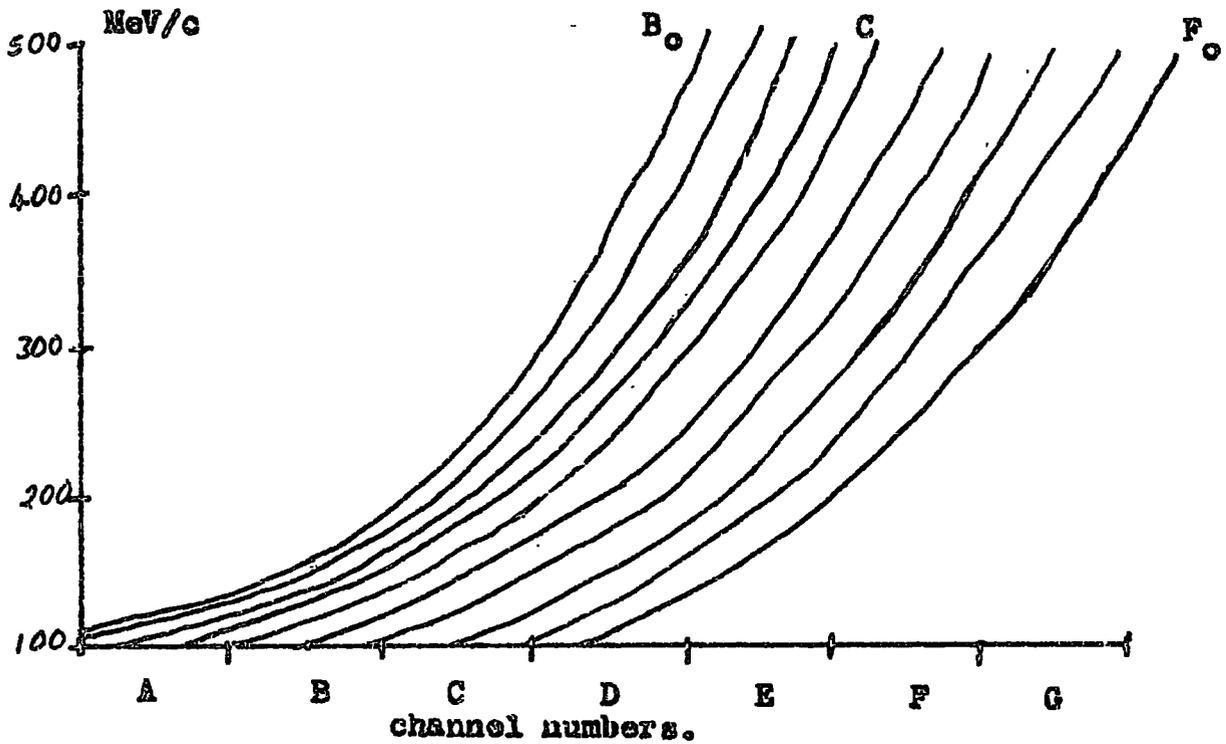
The channels into which the various momenta from
each target position fall.

Figure 22.

height at 0.1 cm from the central peak and having a total
width of less than 0.4 cm altogether (see figure 14).
Therefore the modification for beam width is quite small.
Then the matrix is normalised to 100% for each momentum
interval.   This gives the matrix $N(s, p)$ where s is the
channel number and p the momentum.

A computer program was written, which, given an
initial momentum spectrum $I(p)$ of particles emitted from
the target, would calculate the expected distribution of
tracks per channel.   For each particular plate the
matrix $N(s, p)$ was calculated as given above for channel
number s and for momentum p from 100 to 500 MeV/c.   An
assumed emission spectrum $I(p)$ for the target was then
chosen, and the matrix $M(s)$ formed, where

$$M(s) = N(s, p) \times I(p).$$

$M(s)$ is the expected track density in channels and can
be compared after correction for spurious contribution
from the dummy run.

As has already been mentioned, high energy positive

particles will fall into the same channels as the high

energy negative particles. Those channels in which

positive particles will be found can be determined, but

the exact positive contribution cannot be determined with

accuracy. The effect is more important in C4 where the

negative particles occupy a smaller number of channels.

The momentum spectrum $I(p)$ was therefore fitted over

those channels which could not be occupied by any

contribution from positive particles, channels $1 \rightarrow 3$ in

C4, and channels $1 \rightarrow 6$ in C5. The positive particles

cannot be identified since only momenta and charge, but

not mass, occur in the trajectory equations (see section

2.1).

4.4. Results of the Spectrographic Exposures

a) Results of the dummy run. The conditions under

which the dummy run was made have already been described

in 3.3 and 3.4. Despite the changes made in the

spectrograph, a preliminary scanning of the plates

revealed a very high background in plates from positions

1 and 2. After comparing the dummy plates with those

exposed around a carbon target, it was concluded that the

ratio of background to secondary tracks was too high in these two positions. For the dummy run therefore plates from positions 4 and 5 were concentrated on, and hereafter are referred to as plates D4 and D5 respectively.

Table VII shows the results as the density of tracks per channel for D5. As expected for general background, the density is evenly distributed over all channels, and therefore over the whole area of the scan. This background will include external radiation, and particles scattered within the detecting system.

The results for D4, Table VIII, show the same even background distribution per channel. The fluctuations are within the experimental error.

b) <u>The exposure to a carbon target</u>. The plates exposed with the carbon target in position were labelled C4 and C5 in positions 4 and 5 respectively. The angle A the perpendicular to the plate makes with the beam (alreadt defined in chapter 2) is 68° for positions 5 and 121° for position 4. Sampling is therefore predominantly centred on these two angles.

Observed Track 'Densities' in D5.

channel no:	0	1	2	3	4	5	6
'density'	0.50	0.95	0.84	0.83	0.88	1.04	0.69
error ±	0.20	0.20	0.17	0.14	0.13	0.13	0.10

channel no:	7	8	9	10	11	12
'density'	1.04	1.08	1.01	1.27	0.93	0.78
error ±	0.13	0.13	0.13	0.15	0.13	0.13

channel no:	13	14	15	16
'density'	0.86	0.96	0.51	1.06
error ±	0.14	0.20	0.16	0.30

TABLE VII

Observed Track 'Densities' in D4.

channel no:	0	1	2	3	4	5	6
'density'	0.97	1.24	1.25	1.15	1.08	0.78	0.99
error $\pm$	0.25	0.21	0.18	0.15	0.14	0.16	0.20

TABLE VIII

Table IX gives the value for t, d and δ (see figures 5b and 17) for the plates on which extensive measurements were made. The most important variation is in δ, which was therefore measured with a very high degree of accuracy.

In C5 and D5, equal areas of 51.7 mm^2 were scanned. The results are shown in Table X, and figure 23. The central channels can clearly be seen to contain the scattered pions.

The channels in C4 are spaced and numbered as in D4, the foot of the perpendicular to the plate being used as the reference in both cases. The area scanned in C4 was 13.2 mm^2 compared with 24.7 mm^2 in D4. A greater area was scanned in the dummy plate in order to achieve better statistics for the background. Unlike D4, the track density in C4 varies with channel number with a maximum in channel 3 (see Table XI).

c) <u>The plates exposed with a silver target.</u> Preliminary examination of the plates exposed with a silver target in position revealed that because of the extremely high background, the signal/background ratio was very small. Much larger areas would have to be

Plate constants

Plate	t in μ error ± 20 μ	d in mm error ± 0.1 mm	δ in mm error ± 0.005 mm
D5	865	53.84	-2.19
C5	845	54.16	-1.68
D4	850	54.50	+2.79
C4	885	54.50	+2.79

t is shown in figure 17.

d and δ are shown in figure 5b.
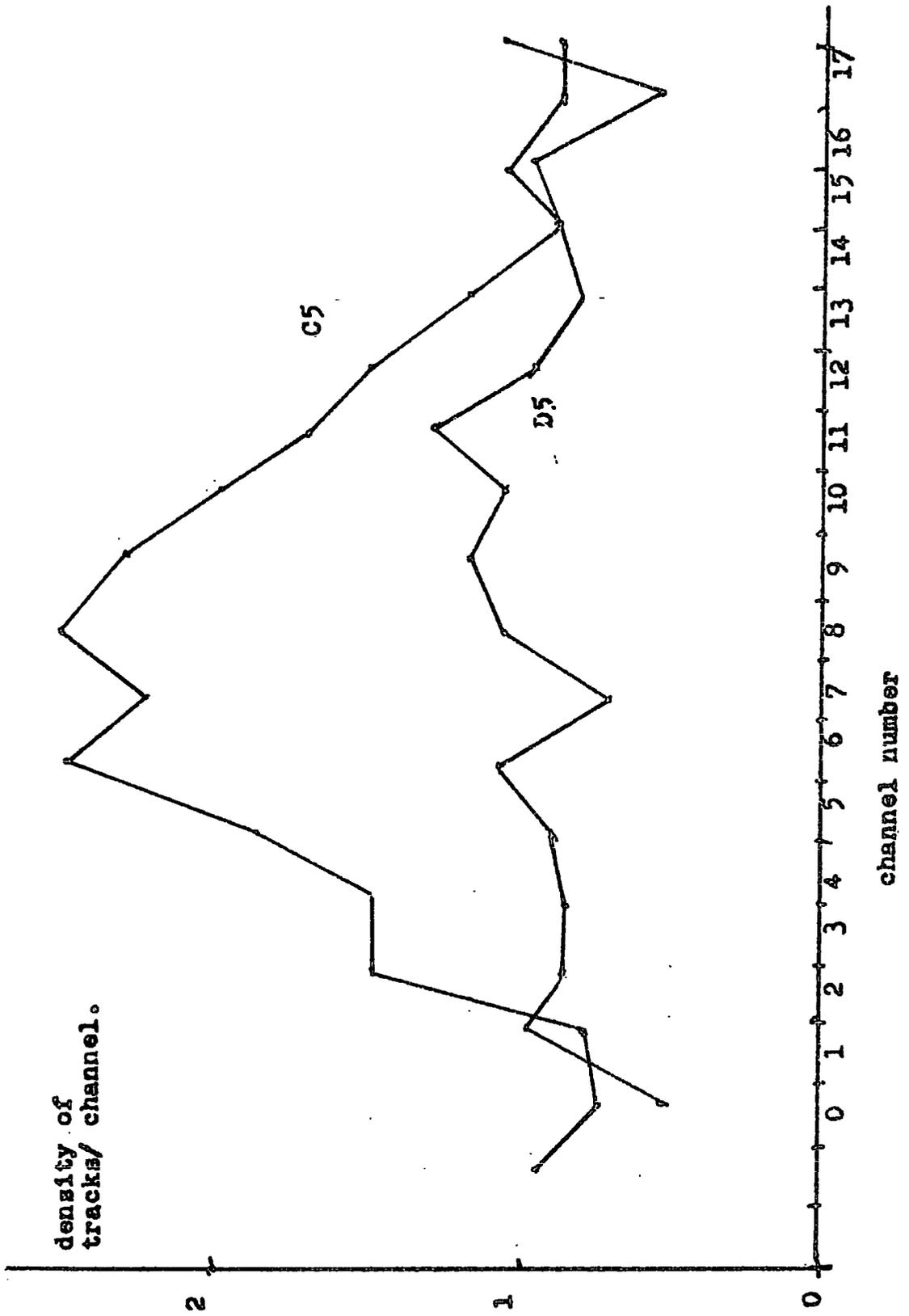
TABLE IX

Figure 23.

scanned, than in the plates exposed with a carbon target, in order to achieve good statistics.

d) <u>The signal</u>. In order to estimate the signal accurately it is necessary to normalise the results from the dummy plates so that the total exposure and area scanned are equivalent to that in the plates exposed with a target.

Equal areas have been scanned in C5 and D5, therefore D5 was normalised, so that the densities were corrected only for the different exposure times by the factor

$$\frac{\text{length of C exposure}}{\text{length of D exposure}} = 1.07 \qquad 4.4.1.$$

The normalised densities in D5 and the resulting signal are shown in Table X

The densities in D4 naturally require the same correction for exposure time as those in D5, see equ. 4.4.1. In C4 the area scanned was 0.53 (13.2/24.7) of that scanned in D4. An additional correction was needed since the channel lengths were not equal in the two plates. This additional correction was the ratio of the

channel	D5 unscaled	D5 scaled	C5 density	signal
1	0.95 ± 0.20	1.02 ± 0.20	0.76 ± 0.16	-0.26 ± 0.3
2	0.84 ± 0.17	0.90 ± 0.17	1.48 ± 0.20	0.58 ± 0.3
3	0.83 ± 0.14	0.89 ± 0.14	1.46 ± 0.18	0.57 ± 0.2
4	0.88 ± 0.13	0.94 ± 0.13	1.83 ± 0.18	0.89 ± 0.2
5	1.04 ± 0.13	1.11 ± 0.13	2.47 ± 0.20	1.36 ± 0.2
6	0.69 ± 0.10	0.74 ± 0.10	2.20 ± 0.18	1.46 ± 0.2
7	1.04 ± 0.13	1.11 ± 0.13	2.29 ± 0.17	1.18 ± 0.2
8	1.08 ± 0.13	1.16 ± 0.13	2.28 ± 0.19	1.12 ± 0.2
9	1.01 ± 0.13	1.08 ± 0.13	1.98 ± 0.17	0.90 ± 0.2
10	1.27 ± 0.15	1.36 ± 0.15	1.68 ± 0.16	0.32 ± 0.2

In channels 0 and 11 to 16, the signal is very low and
oscillates around zero.

The signal in C5.

TABLE X

lengths of the channel in D4 and C4.   The final
correction was therefore

$$1.07 \times 0.53 \times \frac{\text{length in D}}{\text{length in C}}$$

The scaled densities and resulting signal are shown in
Table XI.

e) <u>Plate efficiencies</u>.   The plate detection
efficiency has already been discussed in chapter 2
(see 2.5), where the solid angle subtended at the centre
of the target was calculated, and the selective detection
of momentum was mentioned.

The size of the target has a negligible effect on
the solid angle, the variation for different emission
points naturally being of the same order as that for the
different emission angles - an average of 12%.   For
particles in the same plane, it is 6%.

The selective detection of momenta at the plate
edges can be seen from the channel-momenta matrices.
Channel 1 which lies to one side of the plate contains
predominantly low momenta.   However as long as
ψ ($\tan^{-1}$ X/d) remains small ($\lesssim$ 20°) the channel length

channel	D4 unscaled	D4 scaled	C4 density	signal
1	1.24 ± 0.21	0.98 ± 0.17	1.13 ± 0.25	0.15 ± 0.3
2	1.25 ± 0.18	0.99 ± 0.14	1.97 ± 0.25	0.98 ± 0.3
3	1.15 ± 0.15	0.91 ± 0.12	3.16 ± 0.29	2.25 ± 0.2
4	1.08 ± 0.14	0.85 ± 0.11	2.54 ± 0.25	1.69 ± 0.2
5	0.78 ± 0.16	0.62 ± 0.13	1.77 ± 0.22	1.15 ± 0.2
6	0.99 ± 0.20	0.78 ± 0.16	1.23 ± 0.18	0.45 ± 0.3

The Signal in C4

TABLE XI

is proportional to the emission angle over which particles
are detected.   Table XII shows this range for C4 and C5.
The total angular range detected by the plate for any one
target emission point is about 20°.   The emission angle
detected falls off very slowly with the vertical co-ordinate
of the emission point on the target, the greatest variation
being 5° between the centre and the extremity of the
target.   If the mean emission angle is calculated for the
target centre, and taken as the mean for the whole target,
the error is only $\pm$ 1°.   The 'density' of tracks per
channel was the variable used, and this should be
proportional to the density of tracks per angle of emission.
In those cases where approximate calculations were made
to check this assumption, the error was $\pm$ 5%.   The
matrix method therefore automatically corrects for plate
efficiencies during the calculation.

   f)   <u>Scanning efficiency</u>.   The efficiency of
detecting a track depends on its total projected length
in the top emulsion.   Steep tracks perpendicular to the
surface are more efficiently detected than those tracks
with a much greater projected length, since it was the

Plate	$\bar{p}$ MeV/c	centre of target angular range	mean angle
C4	100	126 - 140	132
	200	120 - 135	127
	400	117 - 132	124
C5	100	69 - 91	80
	200	63 - 87	75
	400	61 - 82	72

angular range - average range from total height of target
along central certical line.

mean angle   - mean angle for central point of target,
the error on this is only $\pm$ 1° if it is
taken as the mean for the whole target
(see text).

TABLE XII

steep tracks for which the scanner was looking, and longer
tracks were to some extent lost in the background of long
tracks running across the emulsion.   Usually therefore
high momenta were detected more efficiently than low
momenta.   The corrections are shown in Table XIII.

　　　g) The determination of the initial momentum spectrum.
The best fit to the observed data, tables X and XI, was
obtained using the computer program mentioned above
(section 4.3.b) by which the momentum spectrum of the
scattered mesons is determined.   It is shown in figure 24
for plate C5 and figure 25 for plate C4.   The corresponding
momentum distributions are shown in table XIV.   The
program was originally run ignoring the possibility of
positive particles reaching the plates.   Under these
circumstances the results for C5 were acceptable because
6 channels receive negatively but not positively charged
particles.   Plate C4 requires a double peaked momentum
curve, the peaks occurring at 125 MeV/c and 325 MeV/c,
if all track densities are assumed to be due to negative
particles.   Fits were therefore made to those channels
which could not contain positive particles.

Scanning Efficiency

Momentum MeV/c	C4	C5
100	90 ± 10%	64 ± 20%
400	92 ± 6%	84 ± 12%

Estimated Errors

Error as % due to –	Plate	Momentum MeV/c.		
		100	200	400
	C5			
solid angle		0	11	6
energy loss in target		10	2	0
Total		10	13	6
	C4			
solid angle		0	0	0
energy loss in target		10	2	0
Total		10	2	0

TABLE XIII

The best fitting of computed model, program to the best density/channel results for plate 65.
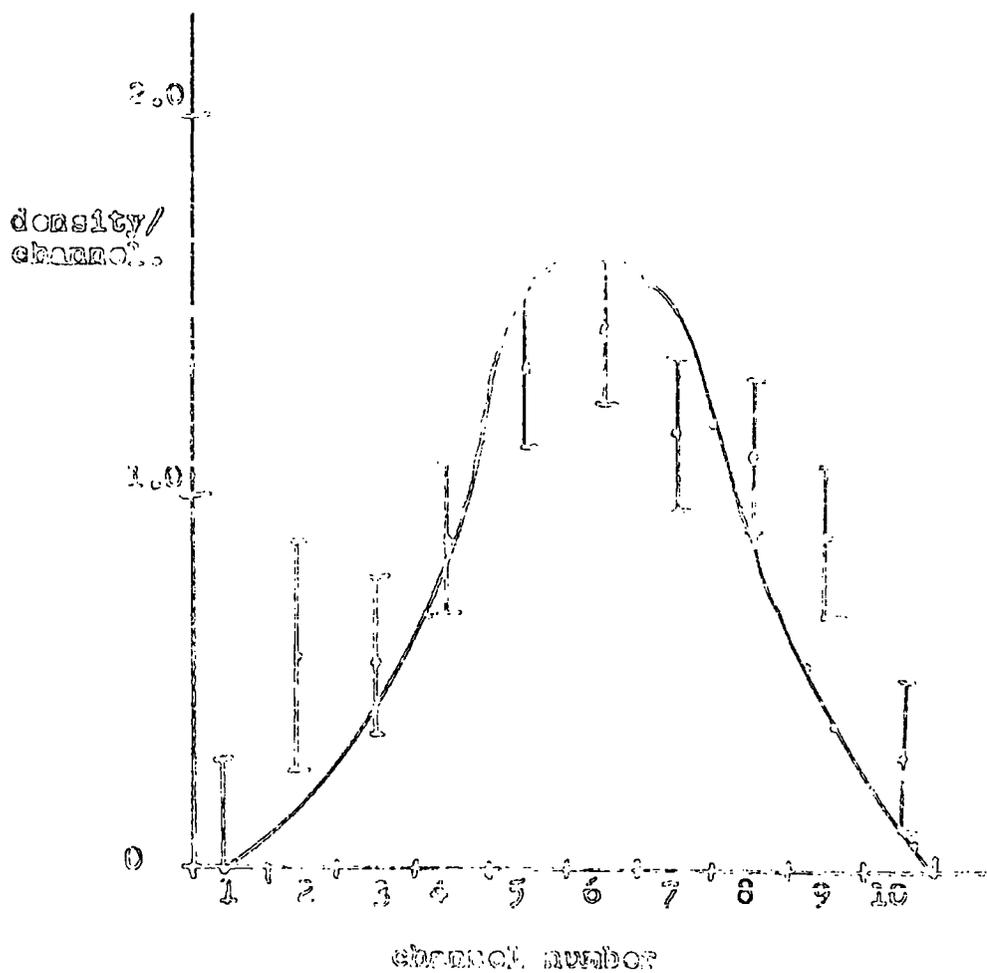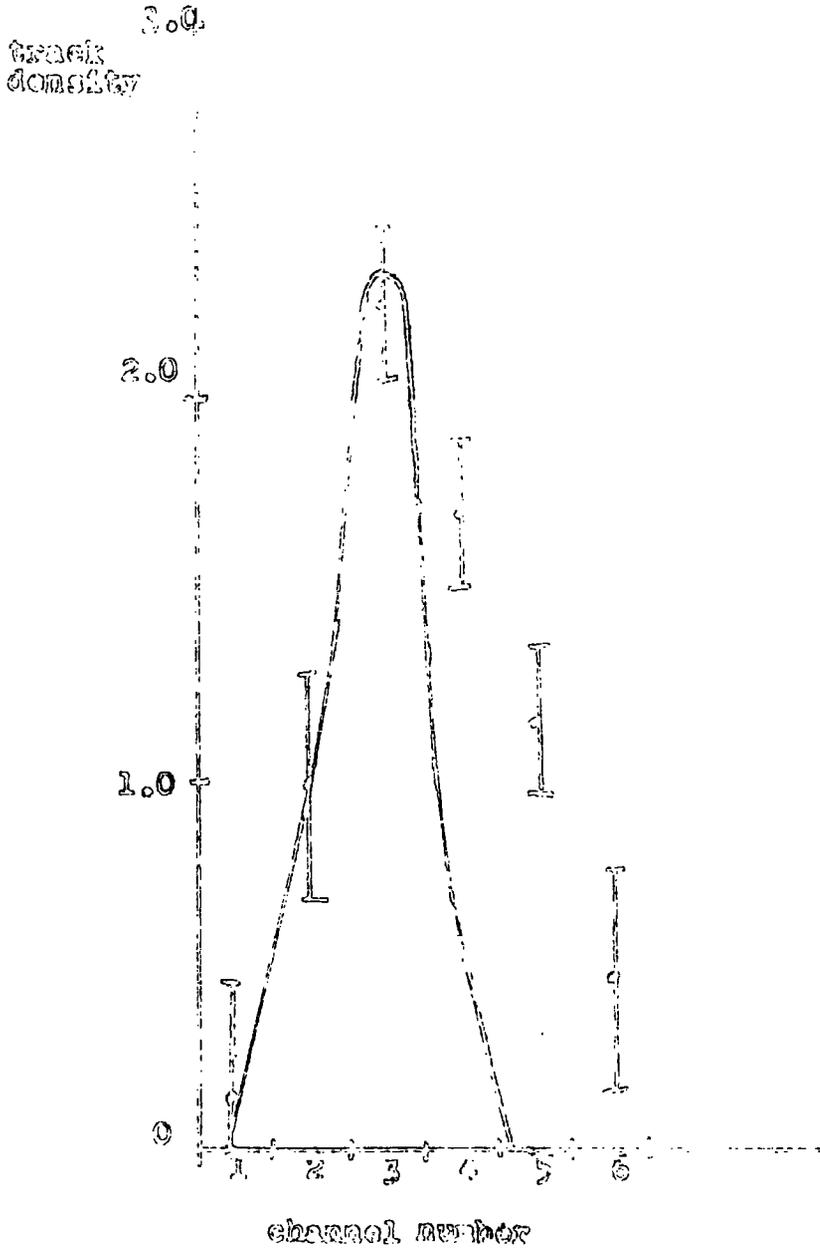

Figure 26.

Figure 25c

In plate C5 the fit was made to channels 1 - 6, since any positive particles would be expected to fall in channels 7 - 14. It is this fit which is shown in figure 24.

Plate 24 samples angles in the backward direction, where the momentum is expected to be low. It is precisely this area where the greatest uncertainty will occur. Firstly, for example, pions with momenta of 100 MeV/c after scattering may leave the target with only 80 MeV/c because of energy loss (see section 2.5). This will tend to bias the measured momenta towards low values, that is the lower momentum channels will contain particles whose original scattered momenta belonged to higher channels. This effect is only important for momenta below 150 MeV/c. Secondly, pions emitted with very low momenta are so strongly deflected in the magnetic field, that they never reach the recording plate. For this spectrograph, pions emitted with momenta less than 80 MeV/c will firstly lose energy in the target, and secondly be trapped in the magnetic field. The bias to low momenta and the trapping in the field are important in momentum channels 1 and 2. Channel 1 will

The momentum spectra which provide the best fit to the channel density curves.

Spectra were fitted over channels 1 - 6 in C5 and channels 2 and 3 in C4.

momentum MeV/c.	C4	C5
100 - 150	15 (20)	2 (5)
150 - 200	10 (15)	20 (22)
200 - 250	7	33
250 - 300	4	20
300 - 350	2	5
350 - 400	1	3
400 - 450	0	2
450 - 500	0	0
mean p	188 $\pm$ 20 MeV/c	239 $\pm$ 10 MeV/c

TABLE XIV

contain particles originally scattered with momenta of less than 100 MeV/c, and also particles which have lost energy in the target. This means that a momentum spectrum fit can only be made to channels 2 and 3, and that only the very roughest estimate of the spectrum can be made. The channel contents for plate C4 are summarised in table XV.

Since low momenta particles are lost, and high momenta particles are obscured by positive tracks, the ends of the momentum spectrum are uncertain. The errors quoted on the mean p in table XIV are due to the uncertainty of the momentum spectrum at high and low momenta. The figures in brackets, in table XIV show the corrected figures if maximum absorption took place.

4.5. Pβ Measurements in Conventional Exposure.

The plates from the emulsion stack were examined on a Cooke microscope under a magnification of 80 x 1.5 x 15, and on a Koristka R4 under a magnification of 62 x 2 x 15. Tracks within five degrees of a chosen angle to the beam direction, were picked up 1 cm from the

Occupation of channels in plate C4.

| channel	contribution
1	a) negative particles below 100 MeV/c from back of target.
	b) negative particles between 100 - 150 MeV/c, which have undergone further energy loss.
2	negative particles between 100 - 150 MeV/c, from the back half of the target.
3	negative particles between 100 - 500 MeV/c.
4	a) negative particles of 200 - 500 MeV/c, from front half of target.
	b) positive particles of 500 - 250 MeV/c, from back half of target.
5	positive particles between 500 - 80 MeV/c.
6	positive particles of below 200 MeV/c, from the front half of the target.

The momenta quoted are those of the secondary meson after the initial scatter in the carbon target.

TABLE XV

edge of the plate, and scattering measurements made on them. The cell lengths used were 200μ and 300μ, and the angles selected were 20°, 45°, 75°, 90°, 135° and 157° (see Fig. 26). The accuracy on each measurement was about 10%. Ten or more individual measurements were made at each angle.

The evaluated pβ was assumed to refer to the centre of the track. The distance of this point from the emulsion edge at the point of entry was measured, and the momentum calculated at entry from the tables of Barkas (1958). Further correction was made for the range of the secondary in the carbon target. It was assumed that the scattering occurred along the central axis of the target. In the case of 20° scatterings the interactions take place near the entrance of the target; for 135°, near the exit. The primary energies differ by about 25 MeV. To allow for this the secondary pion energies were scaled so that the primary energy is 285 MeV.

a) 75°. Detailed measurements were made at 75 ± 5° to the original beam direction. 79 pion tracks were measured in all. The results after correction for energy loss in emulsion and carbon are shown in figure 27.
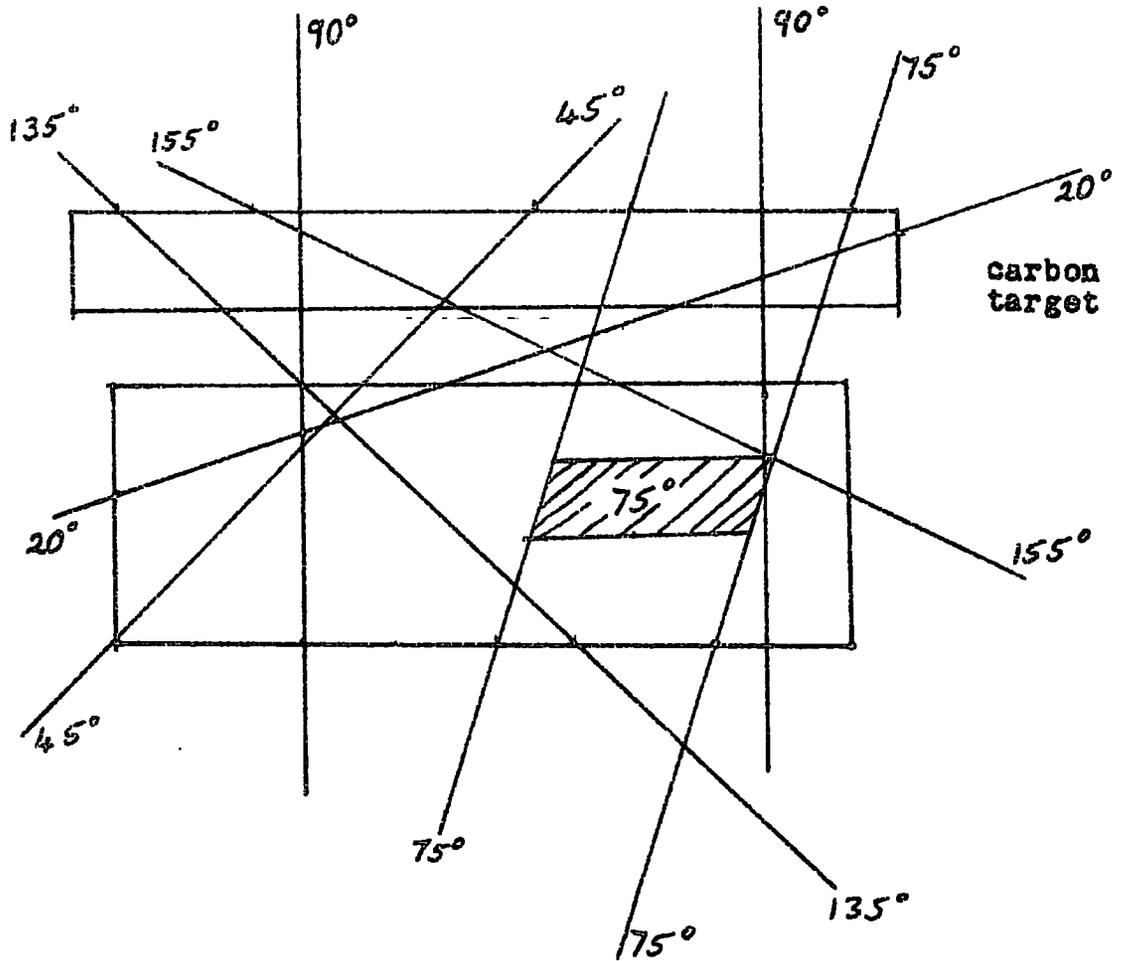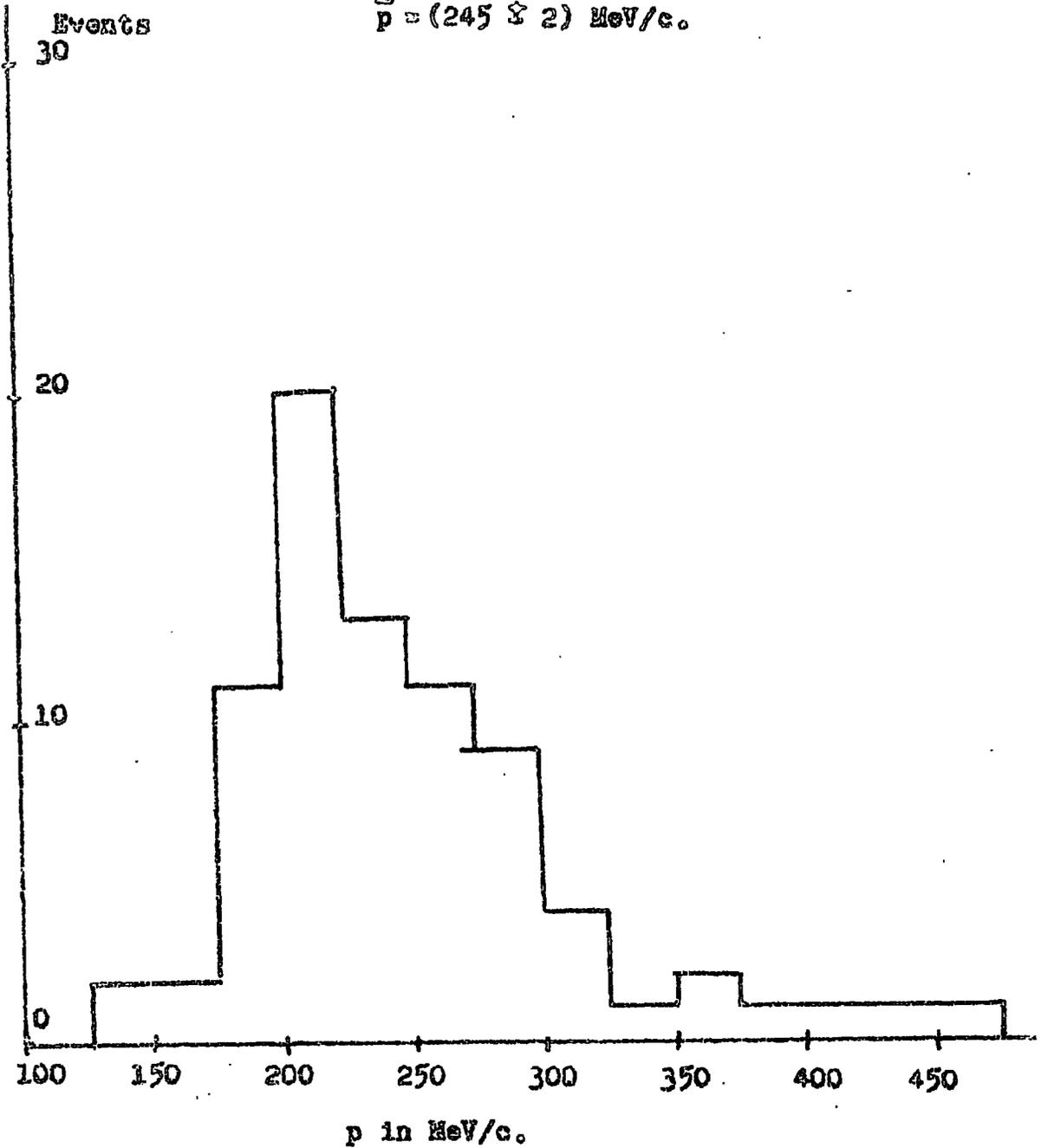
Regions of the solid block over which $p\beta$ measurements
were made. (Drawn to size.)

Figure 26.

Scattering at 75°

$\bar{p} = (245 \mp 2)$ MeV/c.

p in MeV/c.

79 tracks. Average measuring error 22 MeV/c.

pβ measurements corrected for energy loss in target and in emulsion.

Figure 27.

The distribution is uniquely peaked between 200 and 225 MeV/c, the peak being broader on the high momentum side. The average momentum is 245 ± 2 MeV/c.

b) <u>90°</u>. 180 tracks whose angle with the beam direction was 90 ± 5° were measured. The values for pβ were corrected for energy loss in the target and emulsion as before. The results are shown in figure 28. There is one broad peak at around 200 MeV/c, and the average momentum is 228 ± 2 MeV/c.

c) <u>Other angles</u>. Only a brief inspection of the secondary momentum at other emission angles was made.

10 tracks were measured up whose average emission angle was (20 ± 1)°. Of these 10 tracks, one appeared to be an elastic scatter with momentum approaching that of the incident beam. The average momentum of the remaining 9 was 343 ± 13 MeV/c.

At 45 ± 2° to the incident beam, 17 tracks gave an average momentum of 283 ± 15 MeV/c.

9 tracks at (135 ± 5)° to the main beam had an average of 171 ± 12 MeV/c, and ten tracks at (157 ± 3)° gave an average of 181 ± 12 MeV/c. All momenta have
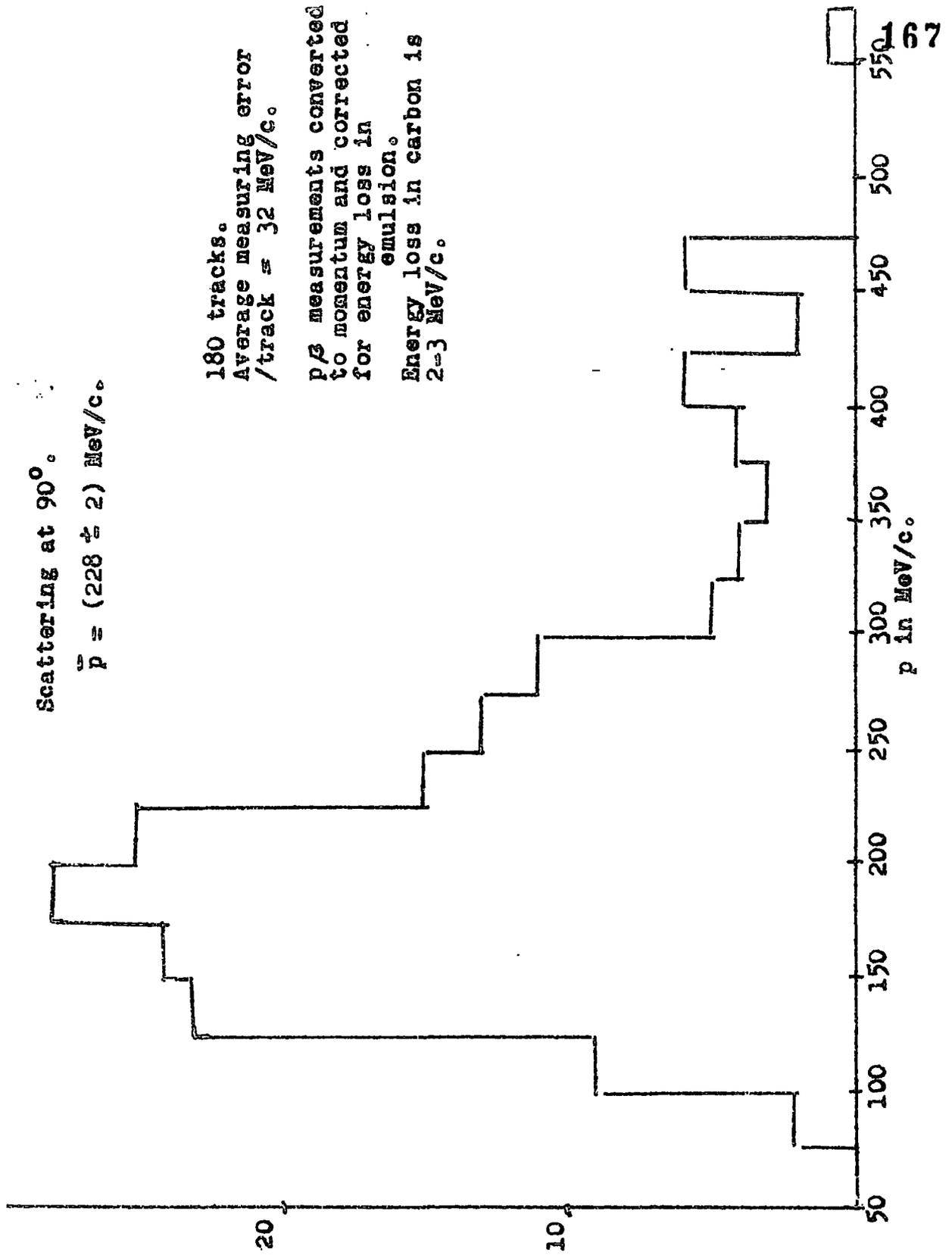
Figure 28.

been corrected for energy loss in the emulsion and target.

d) <u>Momentum spectrum</u>. In figure 29 is shown the secondary momentum versus emission angle spectrum obtained from the $p\beta$ measurements. This shows the expected decrease in momentum at high angles of emission, the average momentum in the backward direction being around 180 MeV/c. At each emission angle the actual momentum spread is quite considerable however, as can be seen from figures 27 and 28.

4.6. <u>Results and Conclusions on Technique</u>.

a) <u>Comparison of conventional and spectrographic exposures</u>. If the mean momentum in table XVI for C5 is compared with that obtained at 75°, very good agreement is observed. Comparison of the actual momentum distributions using a χ^2 test, has a probability p = 0.5. In the conventional $p\beta$ measurements, particles with low momenta would lose energy and be scattered as in the spectrographic exposure, and therefore this end of the distribution has the largest errors. The distributions
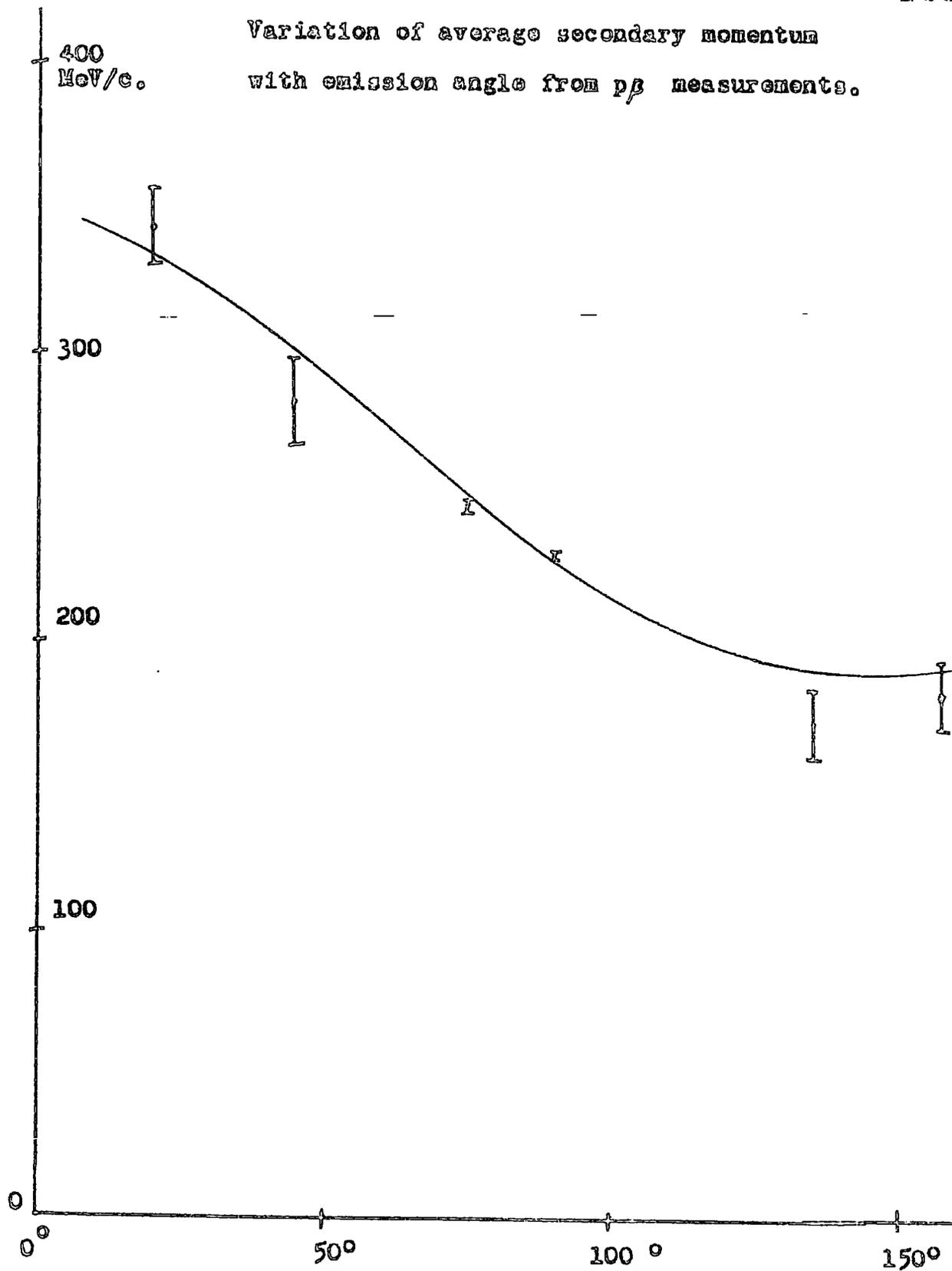
Variation of average secondary momentum
with emission angle from pβ measurements.

Figure 29.

The momentum spectra which provide the best fit
to the channel density curves. A correction
is then applied for scanning errors etc.

| Momentum | C4 | | C5 | |
MeV/c.	best fit	corrected	best fit	corrected
100 - 150	15	18	2	3
150 - 200	10	12	20	19
200 - 250	7	7.9	33	33
250 - 300	4	4.4	20	17
300 - 350	2	2.2	5	5
350 - 400	1	1	3	3
400 - 450	0	0	2	1
450 - 500	0	0	0	0
mean p.	188 ± 20	185 ± 20	239 ± 10	234 ± 10

TABLE XVI

are compared in figure 30, normalised to equal areas.

For C4 the mean angle is 127°. If the results
are compared with those at 135°, the mean momenta are
seen to be compatible. As the pβ of only a small number
of tracks was measured at 135° meaningful comparison of
momentum distributions is impossible.

b) <u>Conclusions on the technique</u>. Scanning is
much quicker of the spectrographic plates than by the
conventional pβ method. The analysis of the present
spectrographic exposure was made difficult by the high
background, which could in future be avoided. Much of
the background arose from scattering of the beam
particles in the side of the magnet. The availability
of a differently constructed magnet, a smaller face area
for instance, would have reduced the background
considerably, and made scanning easier, quicker and more
efficient. The high background not only slowed up the
task of achieving good statistics but also made it
extremely difficult, almost impossible in plates 1 and 2,
to pick out tracks of the right type.

A good beam is essential for both methods. In the
spectrographic exposures, a higher flux of particles per

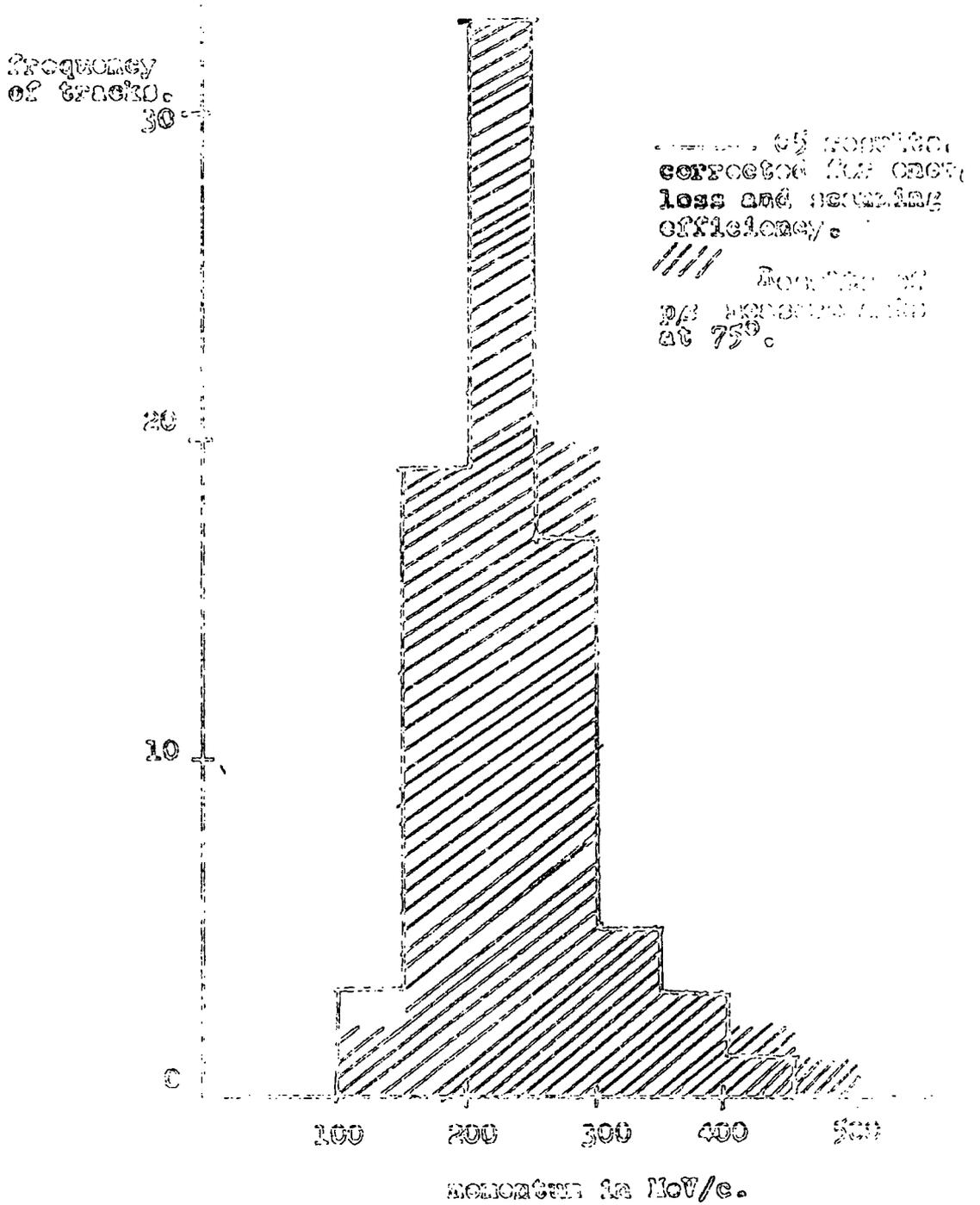Comparison of the results of $p p$ scattering measurements at 75° and the results of plate 69.

Figure 39.

unit area would be preferable.   With such a higher flux
and a sharper beam it would be possible to use a much
smaller, thinner, target, and still obtain a reasonable
flux of detectable secondaries.   The shorter the path   - --
length of the particles in the target, the less absorption
will take place (see chapter 2), thus reducing the
uncertainty on the momentum.   A smaller target area
would also simplify the matrix in the Δx - X system of
analysis, and simplify the range of the emission angles
selected by each plate.

The method of analysis of the spectrographic plates,
while needing good statistics, proved in fact simple to
use.   The matrix for each plate can be worked out
beforehand and the particle positions entered on the
Δx - X plot as the plate is scanned.   Comparison with
the conventional pβ exposure shows that the method is
accurate.

Further use of this method would therefore require
first of all the production of a high flux (of the order
of 2 x 10^4 particles/sec cm^2) well-defined beam, and
the use of a magnet whose structure allows the primary

beam to pass through unimpeded. All six plates of the
spectrograph can then be used with a much smaller target
volume (about 0.25 cm square horizontal cross-section).
The great reduction in background should then render
scanning much more efficient with a much higher signal
to background ratio.

5.   DISCUSSION OF THE RESULTS.

In chapter 4 the momenta of scattered pions were determined at angles of scattering around 75° and 127° using the emulsion spectrograph.   The "conventional" exposure was made to check the results at 75°, and to confirm the use of the spectrograph.   Further measurements were made at 90° with the conventional exposure, and at other angles, i.e. 20°, 45°, 135° and 155°;   small numbers of tracks were measured to establish the variation of mean energy with angles of scattering.

In this chapter the distribution of pion momenta at fixed angles of scattering, and the distribution of mean momenta (or energies) as a function of the scattering angle are compared with the calculations that were described and summarised in chapter I, and with the Monte Carlo calculations of Bertini (1963).   Evidence is sought for the effects of a) nucleonic momenta and to determine if possible their distribution, b) pion potentials, and c) the exclusion effect and its magnitude.

5.1. Distribution of Pion Momenta at Scattering Angles of 75° and 90°.

From figures 27 and 28 it can be seen that a distribution of nucleonic momenta is indicated, rather than a line spectrum from a stationary nucleon. Figure 2d shows the expected spread of secondary momenta at 90° using a nucleonic momentum distribution. The momentum spread is over some 300 MeV/c. The observed momentum spread at 90° is greater than this.

The type of exclusion principle applied was discussed in chapter I, section 10, where it was decided that the depth of the potential well, V, was the determining factor. Carbon has 4 nucleons in the $1s_{\frac{1}{2}}$ and 8 nucleons in the $2p_{3/2}$ (see 1.2, the shell model). Using Strnad's estimations of V_s and V_p (see 1.3), two-thirds of the nucleons require momentum transfers of greater than $(40 - KE)$ MeV, and the remaining nucleons of greater than $(79 - KE)$ MeV. If the average kinetic energy is 20 MeV, the average energy loss to the nucleons is therefore 43 MeV.

a) <u>Bertini's Monte Carlo calculations.</u> Bertini

(1963) performed a series of nuclear cascade calculations, assuming a varying nuclear density. A pion potential was incorporated, which was equal to the potential of the nucleon with which it was interacting. The nuclear potential being in fact 7 MeV greater than the corresponding zero temperature Fermi energy (see section 1.5).

Bertini ran his Monte Carlo calculations for 300 MeV π^-- C interactions (private communication). Our incident energy was 285 MeV, so assuming that over such a short range the variations are proportional, the results have been scaled. The energy - angle distribution is shown on figure 38 and there is good agreement with our results.

The angular distribution from the Bertini calculations is shown in figure 31. In figure 32, a comparison is made of the predicted energy distribution and the observed one at 90°. The comparison is only fair. As with other π-nucleon calculations (see Bertini 1963), the observed peak is at a much lower energy than the predicted peak. The observed peak includes some

Angular distribution expected
for 300 MeV π⁻ - carbon scatter-
ings (Monte Carlo calculation).

H. W. Bertini.

F/B = 1.88
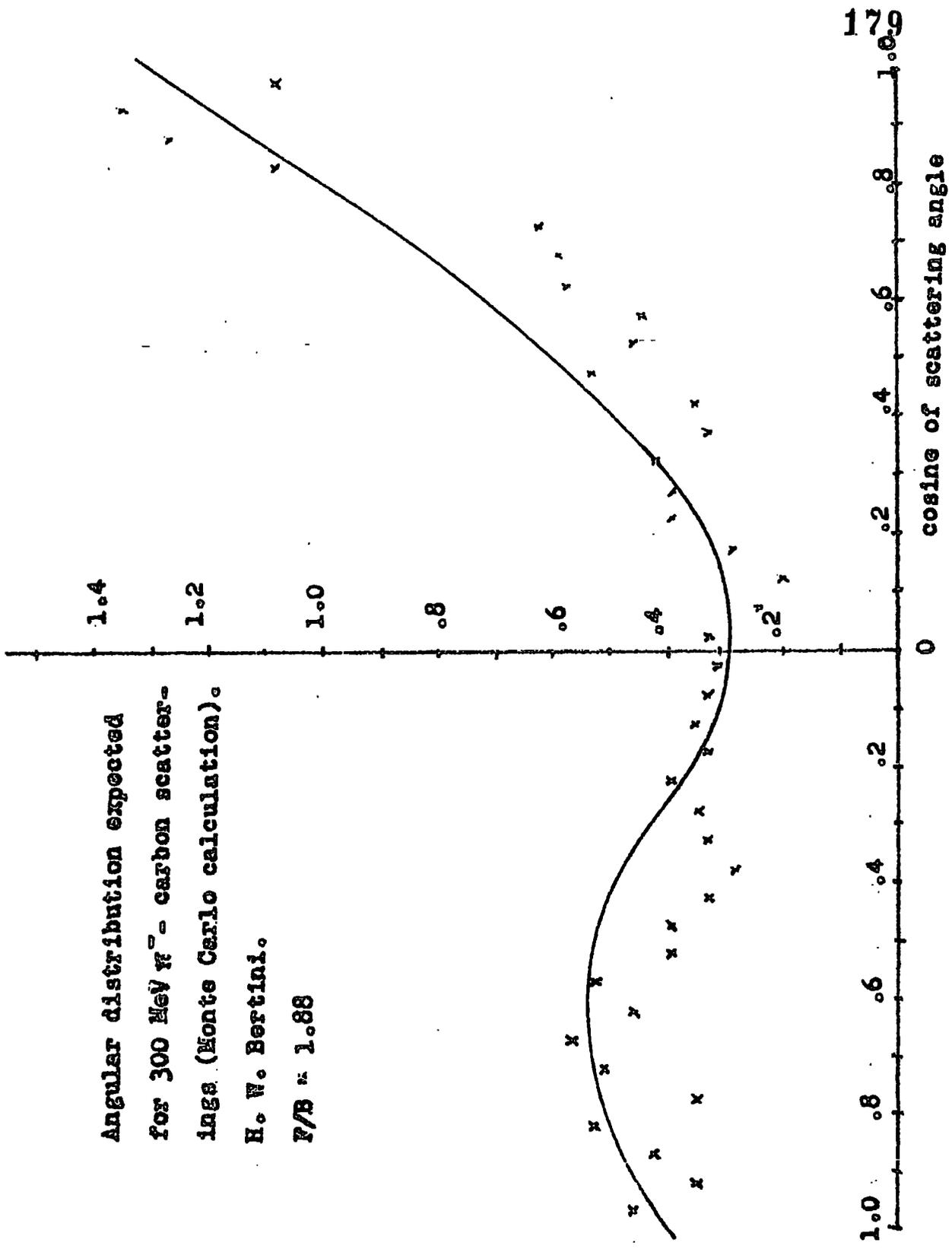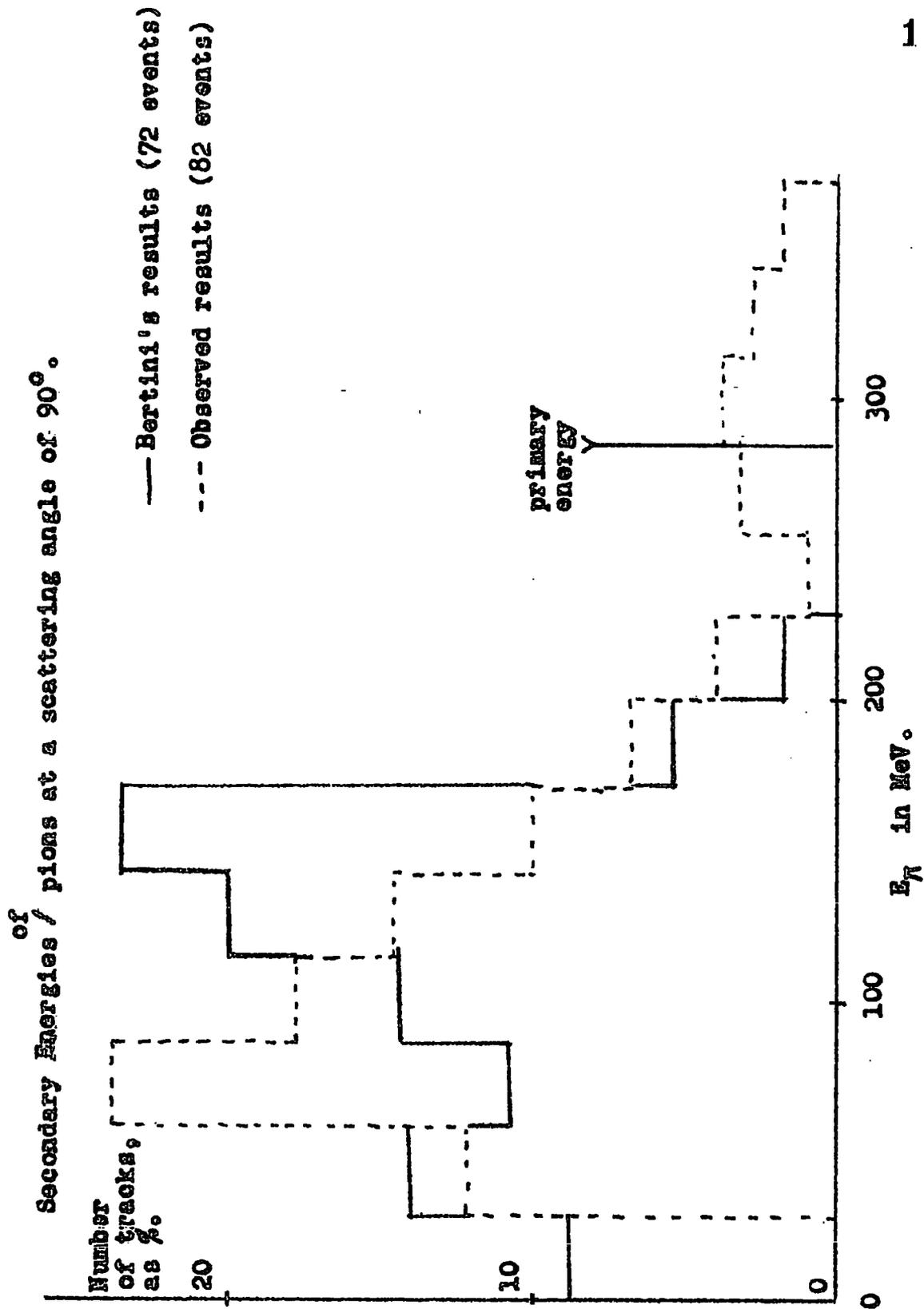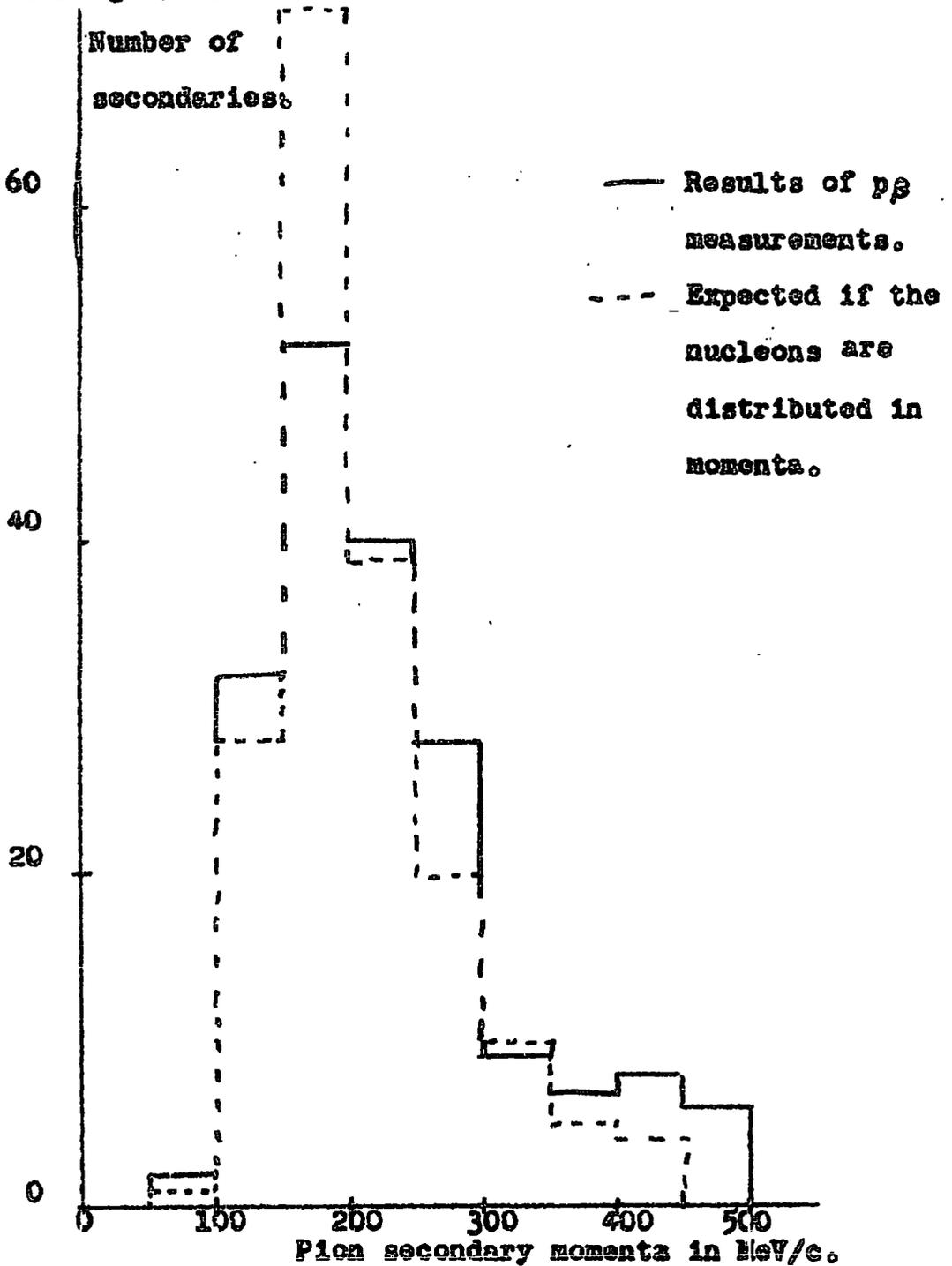
cosine of scattering angle

Figure 31.

Figure 32.

pions of high estimated energy, which the restrictions on the calculations do not allow to occur. The difference between the peaks is about 90 MeV and therefore outside the range of the postulated exclusion principle effect for one nucleon.

   b) <u>Momentum distribution of nucleons and pion potential.</u>   As stated in chapter I, three possible nucleonic momentum distributions have been considered; the Fermi, the Gaussian and a composite Gaussian. In many instances the Gaussian results were identical with those from the Fermi, and never differed very much from the calculations using one of the other two distributions.
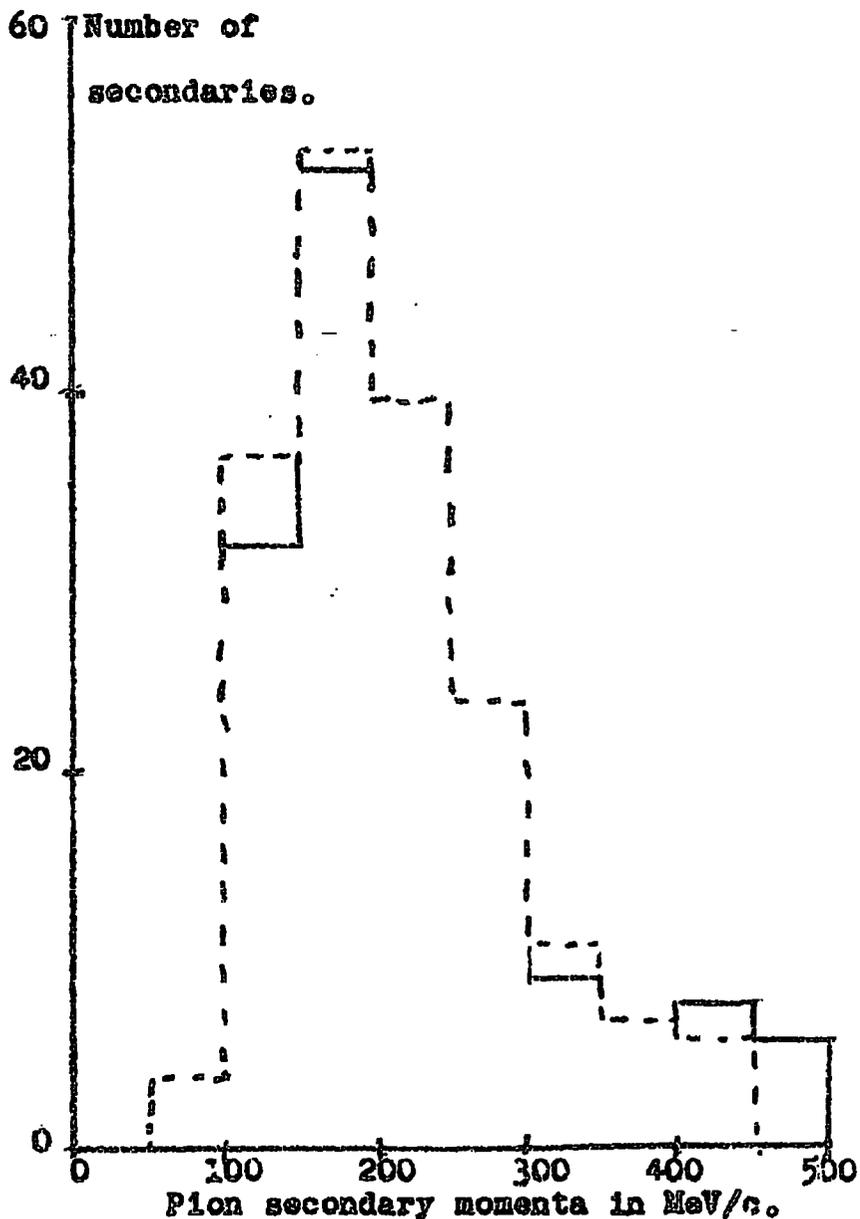
   In figures 33 and 34 are shown the results of $p\beta$ measurements at 90° compared with the expected results for two nucleonic momenta distributions. One distribution is the Fermi with a p_{max} of 225 MeV/c (KE = 12.8 MeV) as an average for all nucleons. The other is the composite Gaussian with a p_{max} of 275 MeV/c (average nucleonic KE = 18.6 MeV). For the composite distribution raising p_{max} to 425 MeV/c, alters only slightly the expected distribution of secondary pion

through 90°.

Number of secondaries.

60

——— Results of pβ measurements.

- - - Expected if the nucleons are distributed in momenta.

40

20

0

0   100   200   300   400   500

Pion secondary momenta in MeV/c.

Nucleons momentum distribution is assumed to be a composite Gaussian. Same total number of events for each.

Figure 33.

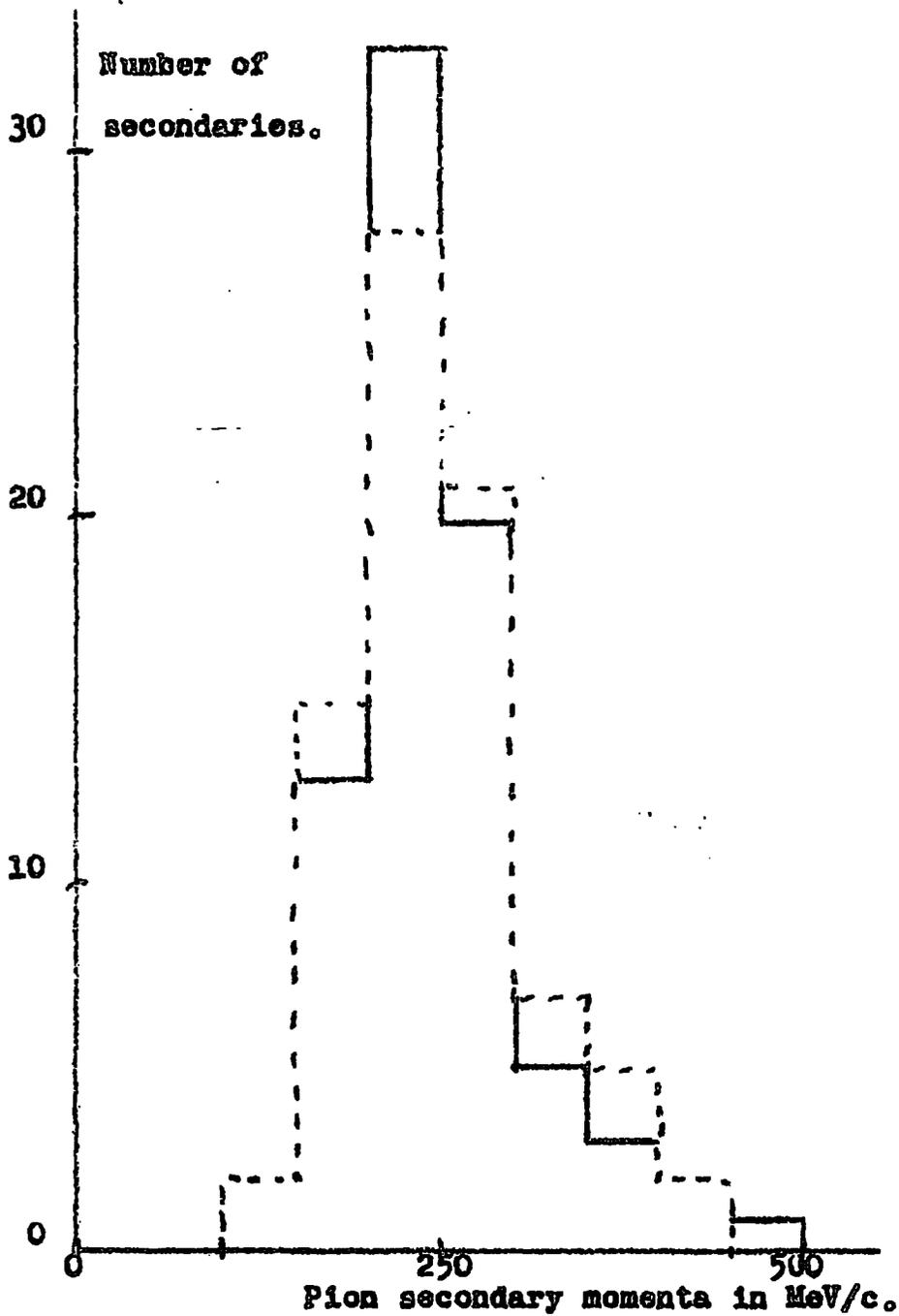— Results of p_{β} measurements. - - - - Expected if the
nucleons have a Fermi distribution of momenta. Same total
number of events for each.

Figure 34.

momenta, but raises the average nucleonic kinetic energy to 24 MeV, which is rather higher than expected (see section 1.3). Both the distributions shown in figures 33 and 34 were obtained by assuming that under the influence of the potential, the pion energy at the moment of impact is 260 MeV (see section 1.10) and after the collision there is a further potential effect as the pion leaves the nucleus. The laboratory energy is estimated from the curve in figure 2c. Both distributions fit better than Bertini's, but the Fermi gives the better fit.

At 75° (see figures 35 and 36) the fits for the two distributions to the observed histogram are again good.

A momentum distribution of the nucleons will therefore explain the spread in secondary momenta, if in addition the pion potential is considered. This potential both tends to shift the peak of the momentum distribution at any given scattering angle, and effectively increases the momentum spread.

Results of p/β measurements. --- Expected if the nucleons have a composite Gaussian distribution of momenta. Same total number of events for each.

Figure 35.
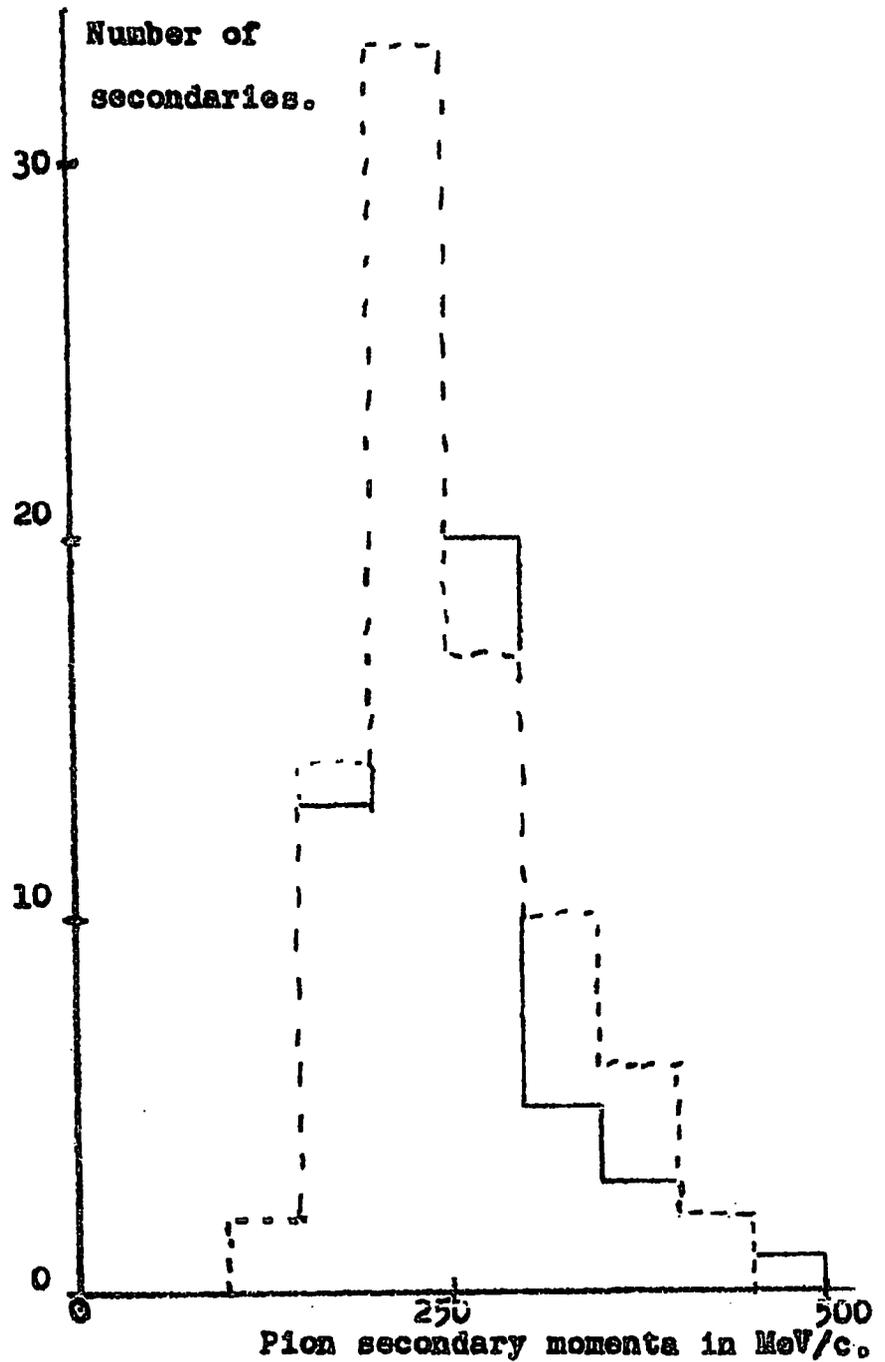
— Results of pp̄ measurements. ---Expected if the nucleons have a Fermi distribution of momenta. Same total number of events for each.
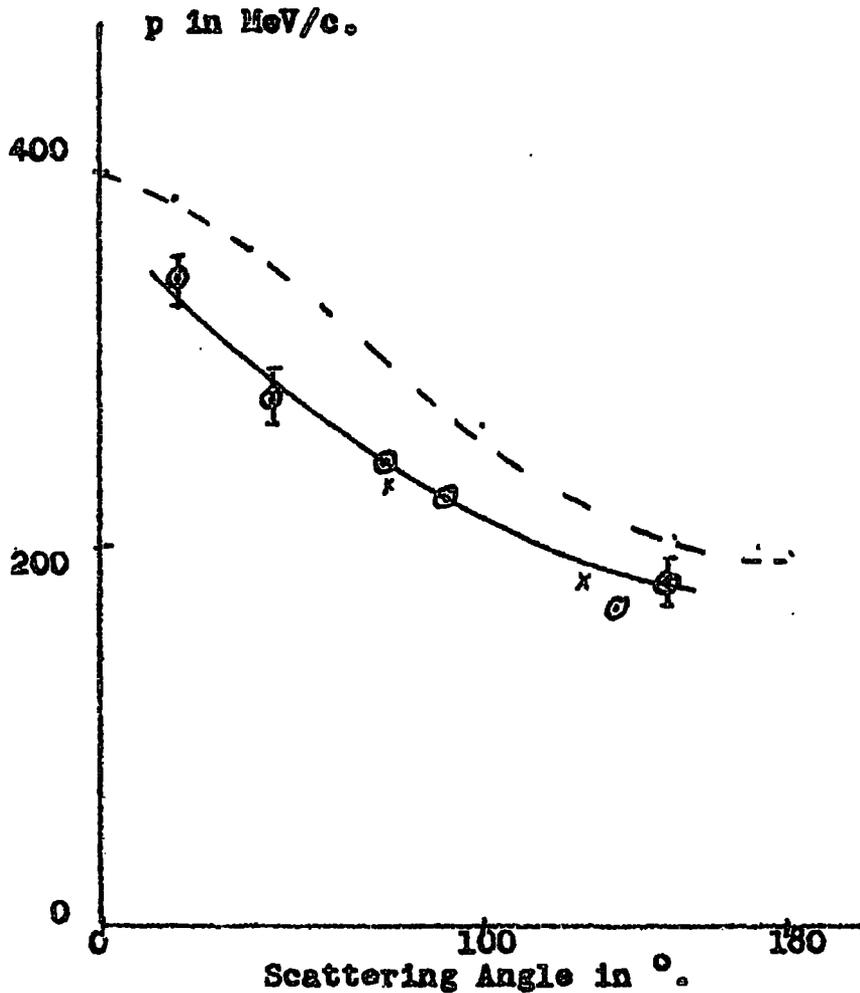
Figure 36

5.2. Variation of Momentum and Energy with Scattering Angle.

In figure 37 the results for the variation of momentum with emission angle are shown. The dotted curve shows the results expected for scattering off a stationary proton. The general shape of the curve is followed by the experimental results, but the observed energy of the scattered pion is consistently less than that expected from free proton scattering.

In figure 38 the results are compared with the expected curve if a distribution of nucleonic momenta is assumed and the pion potential effect is taken into account (see figure 2a). The general agreement is good in the backward, but bad in the forward direction. The potential effect for the average energy is not dependent on the particular momentum distribution chosen.

In figure 39 the results expected for the calculations are shown with an exclusion effect (see section 5.3) in addition to the pion potential. This exclusion effect depends upon the depth of the nuclear well and the nucleonic momenta within the nucleus.
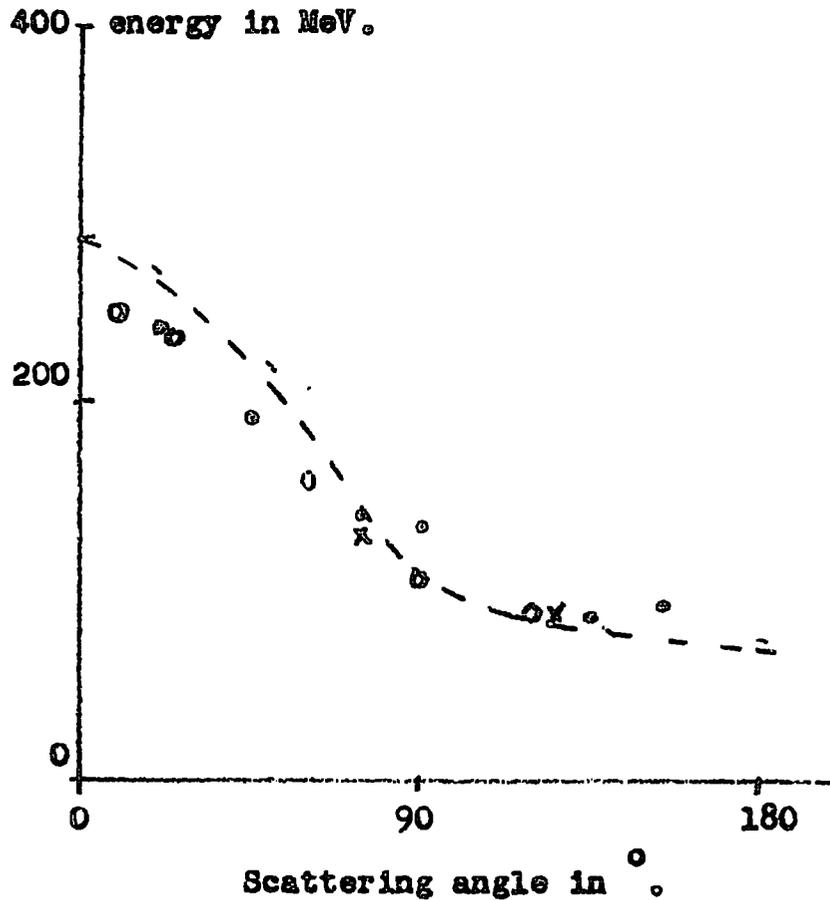
Variation of Secondary Momentum with Scattering Angle.

θ - Results of pβ measurements. x - results of spectrographic exposure. - - -expected results if target is a stationary nucleon.

Figure 37.
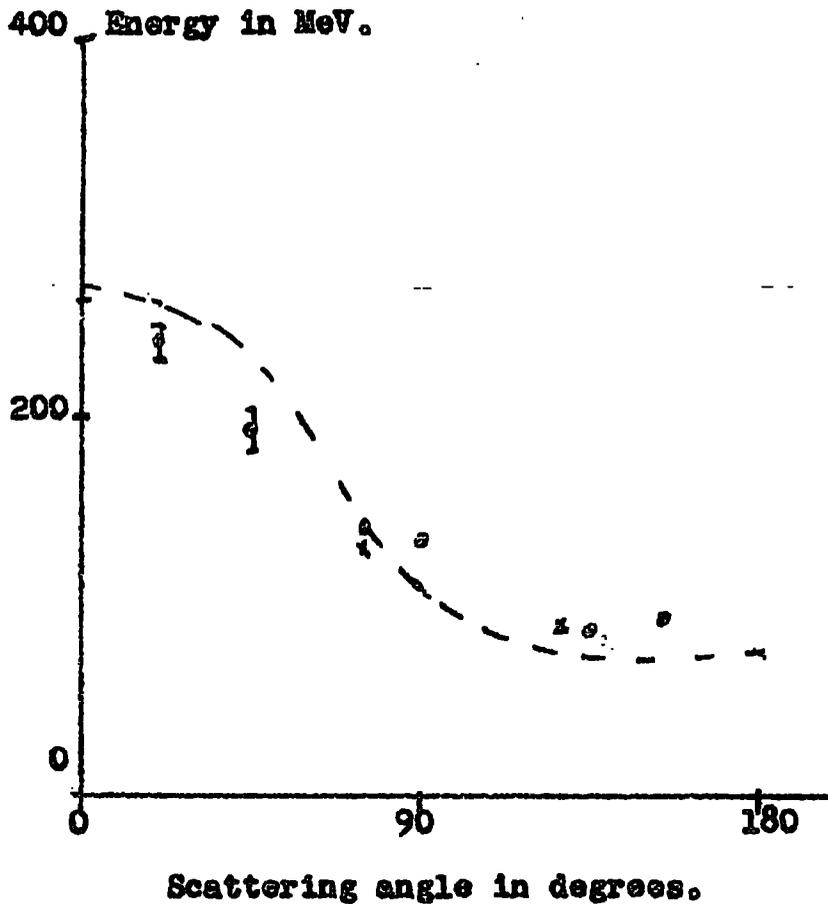
Variation of secondary pion energy with scattering angle.

o - Results of pβ measurements. ✗ - results of spectrographic exposure. O - Bertini's results.
- - - - Expected curve if 290 Me^V pion is acted upon by a pion potential in the nucleus, nucleonic momentum has negligible effect.

Figure 38.

400 Energy in MeV.

200

0

0   90   180

Scattering angle in degrees.

θ - Results of pβ measurements. ✗ - results of
spectrographic exposure. - - - Expected curve if the
nucleons have a composite Gaussian momentum distribution,
and the pion is acted upon by a pion potential and the
exclusion principle applies with a well depth of 53 MeV.
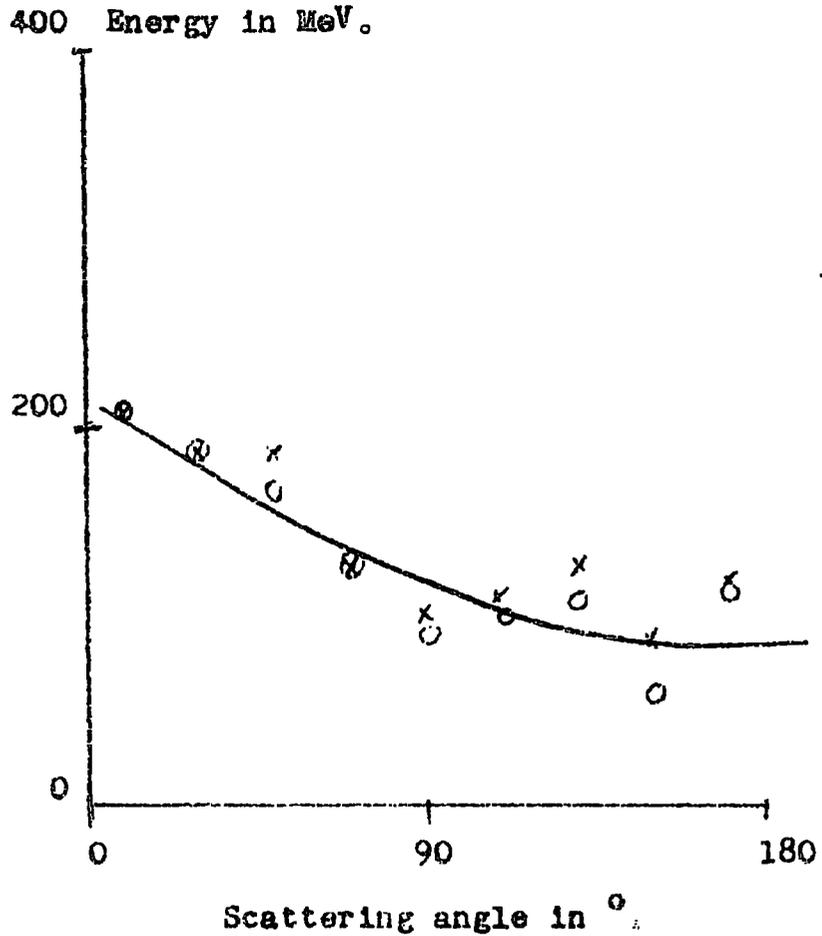
Figure 39.

The results of Bertini's Monte Carlo calculations are shown on the same graph. All give good agreement with one another.

Comparison with other results. Belovitskii (1959) measured the scattering angles and energies of 300 MeV π^- and π^+ in G5 emulsion. In figure 40, the average energy of the scattered meson is shown from Belovitskii's results. These are to be compared with our results at 285 MeV in figure 38. Generally the Belovitskii data give a lower average energy and thus a greater energy transfer. The statistics are not good enough to permit comparison of the energy distributions over a given angular range.

Belovitskii's average energy was 133 MeV. Since only tracks 1500μ long had measurements made on them, there is a lower cut-off in the region of 60 MeV. The forward-backward ratio was, $F/B = 1.15 \pm 0.1$ (all $E\pi > 60$ MeV). Only a third of the particles which should be forward scattered were found (see comparison with the results of Finney et al. below).

Conclusion. The results of scattering experiments

Variation of secondary pion energy with scattering angle, from the data of G.E. Belovitskii (1959)

Scattering angle in °.

x-π^- - with energy greater than 125 MeV. (30 in all).

o -all π^- particles.

Figure 40

require the struck nucleons to be distributed in momenta
within a potential well, and an exclusion principle
depending on the depth of the nuclear potential well
applies.

5.3.   The Pauli Exclusion Principle.

Since both the Fermi distribution and the composite
Gaussian distribution account for the reduction in mean
energy and scattering of pions, it is of interest to
calculate the reduction in cross-section.

As already stated an exclusion principle which
requires the nucleon to escape with greater than a given
minimum momentum, did not give the observed decrease in
mean energy at low scattering angles.   If however V is
assumed to be 53 MeV (average for carbon s and p nucleons),
then the decrease shown in figure 39 is obtained.   If
energy transfers of less than the required amount to
escape from the well are forbidden then at both 75° and
90° only a very small effect is expected.   Calculations
made using both the Fermi and composite Gaussian
distributions, revealed that the forbidden transfers

occurred only at emergent pion mementa at 275 MeV/c and above, and at the most reduce the expected frequency by one-sixth.

The effect of the exclusion principle via the composite Gaussian distributions with a maximum momentum of 275 MeV/c, is to reduce the pion nucleon cross-section by 64%, and to give a forward/backward ratio of 0.89 $\pm$ 0.1. The Fermi distribution when the exclusion principle was applied gave a cross-section reduction of 62%, and a forward/backward ratio of 1.00 $\pm$ 0.1. This can be compared with the results of Finney et al. (1962) who concluded that the deviation of pion-complex nuclei interactions from the prediction of the optical model of the nucleus required a reduction of the pion nucleon cross-section by 63%, and forward/backward ratio of 1.1 $\pm$ 0.35 (all $E\pi$ > 85 MeV). The average energy of the secondaries was 164 $\pm$ 26 MeV. The statistics were too low (80 tracks over complete 180° range) to compare in detail. Altogether the results of Finney et al. and of Belovitskii (see 5.2) are in good agreement with our results using either momentum distribution and the exclusion principle.

By contrast the forward/backward ratio from
Bertini's calculations is 1.88 without any cut-off, and
the ratio would be increased if any low energy cut-off
were applied.   If it is assumed that forward scatters
of less than 20° are rarely detected then the Bertini
ratio does drop to 1.16, but this is a very unlikely
assumption as 20° is an easily detected scatter.

5.4.   Conclusion and Summary

The results quoted here are consistent with the
pion being acted upon by a potential of the order of
30 MeV.   The potential is energy dependent.   The
angular distribution agrees well with Bertini's predictions.
Bertini has in fact used a nuclear momentum distribution
which approximates to a Gaussian with a kT value of
15 MeV.   This value agrees well and lies within the
range of α values quoted in 1.3.4 (Azhgirey, 1959).

The momentum results at 90° are not however
compatible.   Our results have a much greater high energy
tail, whereas the Bertini results have a sharp cut-off

on the high energy side. It is obvious that in some
interactions much more energy is transferred to the
nucleus than is allowed for on Bertini's model. It
would seem that the pion⁻ potential and well depth used
by Bertini are not large enough. However, if the
spread above 285 MeV (figure 32) is taken as an indication
of the general error at high $p\beta$ measurements, then the
average energy is lowered slightly in figure 38, but the
distribution peak in figure 32 remains at 80 MeV.

Assuming a range of nucleonic momenta from 0 to
275 MeV/c and using experimentally determined pion
potentials we can obtain a better fit to the results at
90° than Bertini's model, and this fit is also good at
75°. The exclusion principle has however, a negligible
effect at these two angles.

Summary.

a) Momentum distribution.

The nucleons have a range of momenta from 0 to at least
275 MeV/c. Extending the composite Gaussian to 425 MeV/c

makes only a small difference to the parameters discussed here. The biggest difference is in the average nucleon energy, raising it from 20 to 24 MeV. Measurements at small scattering angles may lead to a determination of the momentum distribution. The two alternatives found suitable so far are:

$N(p) \propto p^2$ the Fermi distribution.

$N(p) \propto p^2 e^{-p^2}/(191)^2$ the composite Gaussian distribution.

b) Pion potentials.

A potential in the region of 30 MeV, which is very sensitive to the pionic energy is needed to explain the experimental results. The function used is shown in figure 2c.

c) Pauli Exclusion Principle.

An exclusion principle is applied such that the struck nucleon must receive (53 - KE) MeV is the reaction is allowed. The exact value of the nucleonic potential has not been determined, 53 MeV having been averaged from the calculations of Strnad, but it gives reasonable agreement

with the experimental results (see figure 39).

Acknowledgements

The author wishes to thank Professor G.D. Rochester for his interest and encouragement and provision of facilities. The author is indebted to Dr. J.V. Major and Dr. A.J. Apostalakis for constant help and fruitful discussion, for doing most of the $p\beta$ measurements and for checking many calculations.

Dr. H.W. Bertini very kindly ran his π-nucleus Monte Carlo program at 300 MeV so that it could be compared with the results reported here.

The author would also like to thank: the staff of the Computing Laboratory of the University of Newcastle-on-Tyne, especially Miss E. Barrington, for much help during the initial stages of programming; Mrs. E. Templeton of the Computing Laboratory, the University of Durham; Mr. D. Jobling of the physics department workshop for constructing the spectrograph; the members of the various groups at CERN whose advice we sought especially Dr. Michaelis, Mr. M. Roberts and Dr. L. Hoffmann; and past and present members of the emulsion group, namely, Dr. G.A. Briggs, Mrs. E. Errington, Dr. P.J. Finney, Professor N.A. Kahn and C. Kitchen.

REFERENCES

Ajzenberg-Selove, F. and Lauritsen, T., 1959, Nuclear
    Phys. 11, 1.

Allen, J.E., Apostalakis, A.J., Lee, Y.J., Major, J.V.
    and Perez Ferreira, E., 1959, Phil. Mag., 4,
    858.

Allen, J.E., Apostalakis, A.J., Lee, Y.J., Major, J.V.
    and Perez Ferreira, E., 1961, Phil. Mag., 6,
    833.

Allen, J.E. and Apostalakis, A.J., 1961, Proc. Roy. Soc.
    A., 265, 117.

Ashkin, J., Blaser, J.P., Feiner, F. and Stern, M.O.,
    1956, Phys. Rev., 101, 1149. CERN Symposium II
    1956, p. 225.

Ashkin, J., Blaser, J.P., Feiner, F. and Stern, M.O.,
    1957, Phys. Rev., 105, 724.

Azhgirey, L.S., Vzorov, I.K., Zrelov, V.P., Mescheryakov,
    M.G., Neganov, B.S., Ryndin, R.M. and Shabudin,
    A.F., 1959, Nuclear Phys., 13, 258.

Baqui Beg, M.A., 1960, Phys. Rev., 120, 1867.

Barkas, W.H., 1958, Nuovo Cim., 8, 201.

Belovitskii, G.E., 1959, Soviet Phys. JETP., 8, 581.

Bertini, H.W., 1963, Phys. Rev., 131, 1801.

Braunersreuther, E., Chabaud, V., Delorme, C. and
Morpurgo, M., 1961, C.E.R.N. reprint, 61 - 12,
p. 12.

Brueckner, K.A., 1958, Rev. Mod. Phys., 30, 561.

Chew, G.F. and Goldberger, M.L., 1950, Phys. Rev., 77,
470.

Clarke, J.O. and Major, J.V., 1957, Phil. Mag., 2, 37.

Deahl, J., Derrick, M., Fetkovich, J., Fields, T. and
Yodh, G.B., 1960, Proceedings of the 1960
Annual International Conference on High Energy
Physics at Rochester, p. 185.

Deahl, J., Derrick, M., Fetkovich, J., Fields, T. and
Yodh, G.B., 1961, Phys. Rev., 124, 1987.

Elton, L.R.B. and Gomes, L.C., 1957, Phys. Rev., 105,
1027.

Fernbach, S., Serber, R. and Taylor, T.B., 1949, Phys.
Rev., 75, 1352.

Feshbach, H., Porter, C.E. and Weisskopf, V.F., 1954,
Phys. Rev., 96, 448.

Feshbach, H. and Weisskopf, V.F., 1949, Phys. Rev., 76, 1550.

Finney, P.J., Major, J.V. and Parkhouse, P.G.J.T., 1962, Phil. Mag., 7, 237.

Garron, J.P., Jacmart, J.C., Riou, M. and Ruhla, Ch., 1961, Journ. de Phys., 22, 622.

Garron, J.P., Jacmart, J.C., Riou, M., Ruhla, C., Teillac, J. and Strauch, K., 1962, Nuclear Phys., 37, 126.

Glauber, R.J., 1956, Physica, 22, 1185.

Gooding, T.J. and Pugh, M.G., 1960, Nuclear Phys., 18, 46.

Gottschalk, B. and Strauch, K., 1960, Phys. Rev., 120, 1005.

Haxel, O., Jensen, J.H.D. and Suess, H.E., 1949, Phys. Rev., 75, 1766L.

Helland, J.A., Devlin, T.J., Hagge, D.E., Longo, M.J., Moyer, B.J. and Wood, C.D., 1962, 1962 International Conference on High Energy Physics at C.E.R.N. p. 3.

Henley, E.M., 1952, Phys. Rev., 85, 204.

Hofstadter, R., 1956, Rev. Mod. Phys., 28, 214.

James, A.N. and Pugh, H.G., 1962, Nuclear Phys., 42, 441.

Karplus, R. and Yamaguchi, Y., 1961, Nuovo Cim., 22, 588.

Kellman, S., Kovacik, W.P. and Romanowski, T.A., 1963,
        Phys. Rev., 129, 365.

Kim, Y.S., 1963, Phys. Rev., 129, 1293.

Maris, T.A.J., Hillman, P. and Tyren, H., 1958, Nuclear
        Phys., 7, 1.

Mayer, M.G., 1949, Phys. Rev., 75, 1969L.

Metropolis, N., Bivins, R., Storm, M., Turkevich, A.,
        Miller, J.M. and Friedlander, G., 1958, Phys.
        Rev., 110, 185.

Metropolis, N., Bivins, R., Storm, M., Miller, J.M.,
        Friedlander, G. and Turkevich, A., 1958, Phys.
        Rev., 110, 204.

Nikol'skii, B.A., Kudrin, L.P. and Ali-Sade, S.A., 1957,
        Soviet Phys., JETP., 5, 93.

Oda, N. and Harada, K., 1958, Nuclear Phys., 7, 251.

Sarjant Singh and Alexander, J.M., 1962, Phys. Rev.,
        128, 711.

Sternheimer, R.M., 1959, Phys. Rev., 115, 137.

Strnad, J., 1962, Nuclear Phys., 35, 451.

Tyren, H., Hillman, P. and Maris, T.A.J., 1958, Nuclear
Phys., 7, 9.

Watson, K.M. and Zemach, C., 1958, Nuovo Cim., 10, 452.

Winsberg, L. and Clements, T.P., 1960, Phys. Rev., 122,
1623.

Yuan, L.C.L., 1956, CERN Symposium, 1956, 2, 195.

Zhdanov, A.P. and Fedotov, P.I., 1961, Soviet Phys.,
JETP., 14, 1330.

Zinov, V.G. and Korenchenko, S.M., 1959, Soviet Phys.,
JETP., 36, 429.